Development of a Particle in Cell Code for the Simulation of Dual Stage Ion Thrusters

Elinor C Bramer

Department of Engineering and Design

University of Sussex

A thesis submitted in fulfilment of the requirements

for the degree of Doctor of Philosophy

September 2013

Declaration

I hereby declare that this thesis has not been and will not be, submitted in whole or in part to another University for the award of any other degree.

Signature:.....

UNIVERSITY OF SUSSEX

ELINOR C BRAMER DOCTOR OF PHILOSOPHY

DEVELOPMENT OF A PARTICLE IN CELL CODE FOR THE SIMULATION OF DUAL STAGE ION THRUSTERS

SUMMARY

This thesis focuses on the design, development and testing of a two dimensional particle in cell (PIC) code (PICSIE) written in Matlab. The code is applied to the specific problem of modelling the performance of dual stage ion thrusters. The code simulates one full aperture within dual stage ion thruster systems, focusing on the flow of ions through the aperture. Only the ions have been included in the simulation in order to minimize running time.

The results produced by the simulation code are compared with results obtained from the vacuum chamber testing of the DS4G prototype, along with results from other simulation codes and research papers in order to verify the performance of the simulation code.

The Dual-Stage 4-Grid (DS4G) and Dual-Stage 3-Grid (DS3G) thrusters are both simulated in order to compare the performance of the two thrusters and assess the benefits and disadvantages of including the fourth grid in a dual stage thruster system. Different grid configurations are simulated in order to find the most efficient configuration of the ion optics and accelerating voltages for each thruster, with the aim being to find the configurations that produce the maximum particle momentum, thrust and specific impulse while minimizing the rate of erosion of the ion optics and maximising the efficiency of the thruster. These simulations are applied to the problem of deciding if the advantages provided in using a 4th grid outweigh the disadvantages compared to the 3 grid design.

The results show that if erosion due to backstreaming ions is disregarded, including the fourth grid in the thruster design results in no apparent advantages in terms of the performance parameters studied in this work. The only noticeable difference between the three and four grid cases is a significant increase in the change in ion momentum observed when the fourth grid is not included in the design. The conclusion of the work is that the fourth grid should not be included in the dual stage design unless a very long lifetime is required and it is thought that erosion due to backstreaming will prevent the three grid thruster from fulfilling this criteria.

The concept of propagating waves through the plasma within the ion thruster discharge chamber is investigated, with the aim of discovering any benefits and improvements in performance that may arise and forming a conclusion on whether further study on the topic of waves within the discharge chamber may be beneficial. No improvements in performance parameters were observed in this work, although further study in the area may show benefits to introducing waves into the plasma.

Acknowledgements

Completion of this thesis was only possible thanks to the help of several people. Firstly I would like to express my sincere gratitude to my supervisor, Dr. Andy Buckley, for his valuable guidance, advice and constant encouragement throughout my research work. It is thanks to Andy that I began working towards a DPhil in the first place, it would never have happened without him.

I would also like to thank my friend and fellow student Sri Reddy for the hours we spent discussing this work, and the University of Sussex for providing the funding which allowed me to undertake this research.

Finally I would like to thank my parents for their constant support, in particular my mother for the hours spent proofreading and critiquing this thesis and the many valuable suggestions provided.

Contents

List of Figures

List of Tables

1 Introduction

1.1 Motivation

In this section the motivation for undertaking this work is discussed. Firstly, due to the lack of flight testing opportunities the computer based simulation studies of ion engines play an important role in research and development. Testing in a vacuum chamber is expensive due to the size of the chamber and the length of time required in high vacuum conditions, and whilst use of a simulation can only ever be used as a complementary tool in the design and testing of a thruster and cannot replace vacuum chamber testing, it provides an efficient and cost effective way of analysing performance factors such as projected lifetime and thrust produced. The basic physics within an ion thruster are better revealed within a simulation and more comprehensive diagnostic techniques can be employed compared with those available in a vacuum chamber, providing a more detailed view of the performance of an engine and the motion of particles within it.

During the design process the most efficient engine configuration needs to be found in order for the engine to perform at the required standard, based on the mission requirements; it would be extremely time consuming to manufacture many variations of the same engine, and the cost would be prohibitive. An optimized configuration of many parameters needs to be found before an engine can be manufactured and tested; a simulation allows the configuration of an engine to be manipulated and the effects of the changes observed in a time and cost effective way.

A wide range of research has already been carried out on the issue of simulating ion thruster performance, as will be discussed in the Literature Review in Section 3. Producing an alternative simulation tool allows comparison between simulation results and provides a different perspective when investigating a research question, allowing a problem to be approached from several different angles and either providing confirmation that a conclusion is accurate or indicating that further work should be done in a particular area.

1.2 Research Aims

The primary aim of this research is to produce a particle in cell code to facilitate the study of dual stage ion thrusters; the simulation will study the flow of plasma through a single grid aperture, producing a range of diagnostic parameters including the change in ion momentum and the number of ions impacting on the grids. The simulation code will be verified by comparing its results to those obtained during testing of a DS4G prototype in a vacuum chamber and those obtained by other researchers from simulations of the DS3G.

Once the simulation code is deemed to be producing accurate results, the aim of this work is firstly to come to a conclusion on whether including a fourth grid in a dual stage system is worthwhile in terms of performance benefits while taking into account the added complexity that would come from the inclusion of the grid. This research will then aim

to find an optimized grid configuration based on target parameters.

2 Introduction to Ion Thrusters

The desire to explore space and gain knowledge of what lies beyond our planet has long been a motivator for technological development. The use of ion thrusters in space travel will allow humans to explore further into space than was previously possible, and the use and development of this technology is vital for the continued exploration of our area of the galaxy.

This section will provide an introduction to the concept of ion thrusters, including the techniques used to produce the ions from the chosen propellant and a discussion on different types of ion thrusters, both those currently in operation and those being studied as possibilities for use in space travel in the future. A history of ion propulsion in space will be provided, along with details of space missions that will use ion thrusters for propulsion in the near future.

2.1 Introduction to Ion Propulsion

Ion propulsion is a technique in which a gas (usually xenon, a colourless, odourless, heavy noble gas) is given an electric charge, producing an ionized gas. The ions are then accelerated to around 30 km/s and emitted from the spacecraft, producing thrust (NASA, 2008). Ion engines are highly efficient compared with chemical engines, although the thrust produced is considerably lower (0.09N of thrust can be produced by an ion engine, compared to between 450N and 2250N for a chemical rocket (NASA, 2008)). This means that ion engines cannot be used for take-off through the Earth's atmosphere, or any other situations where high acceleration and thrust are required, but could be a much better choice for travel in space than chemical engines. Although a chemical engine is more powerful, the duration of thrust is much less than that possible with an ion engine, due to the amount of propellant needed by the chemical engine. The cargo-to-propellant ratio for a typical chemical rocket is 1:2 while the ratio for an ion engine is around 4:1 (Prado, 2002). NASA's Deep Space 1 carried 81kg of xenon propellant, enough to fuel the engine for 20 months (NASA, 2008), whereas ESA's Galileo carried 925kg of propellant which was used in 30 manoeuvres during the gravity-assisted trip to Jupiter (Hamilton, 2009). With current technology an ion engine can operate continuously for several years. NASA's Deep Space 1 achieved a speed of up to 4.5km/s, around ten times the maximum speed of a spacecraft using a chemical engine (Deep Space 1, 2001); the maximum velocity (or the available change in velocity ΔV) depends on the amount of propellant carried. The rocket equation states that

$$\Delta V = I_{sp} g_0 \ln \frac{Mi}{Mf} \tag{2.1}$$

Where Mi and Mf are the initial and final spacecraft masses, ΔV is the required change in spacecraft velocity, g_0 is the gravitational constant and I_{sp} is the specific impulse. It can be seen that to maximise the useful payload, the I_{sp} should be maximised. The I_{sp} is

given by

$$I_{sp} = \frac{F}{\dot{m} g_0} \tag{2.2}$$

Where F is the thrust and $\dot{m}$ is the propellant mass flow rate, which is given by

$$\dot{m} = QM \tag{2.3}$$

Where Q is the propellant particle flow rate in particles per second and M is the mass of the particle (Goebel and Katz,2008). Specific impulse is expressed in units of seconds and is a measure of the propellant fuel consumption rate (Charles, 2009). A high specific impulse shows high propellant efficiency. Ion thrusters achieve much higher specific impulse than chemical rockets, making ion propulsion well suited for travel in space. Chemical rockets can usually produce an I_{sp} of around 200-400s while ion thrusters can generate I_{sp} of several thousand (Boyd, 2011). As much less propellant is needed to be stored aboard an ion thruster this means that the vehicle can be smaller and lighter than a chemical rocket, reducing the launch cost.

The ions are accelerated either by electrostatic or electromagnetic forces. Conventional ion thrusters use electrically charged grids to accelerate the ions and are known as gridded ion engines or GIEs, but several other methods are also available, all of which will be discussed in Section 2.3. The thrust produced by an ion thruster is given by the time rate of change of the momentum, and can be written as

$$F = \dot{m} v_{ex} \tag{2.4}$$

Where v_{ex} is the average exhaust velocity. The mass utilization efficiency and thruster efficiency are often used for comparison between thrusters. The mass utilization efficiency η_m defines the amount of ionized propellant versus un-ionized propellant. It is also known as the propellant utilization efficiency. It is given by

$$\eta_m = \frac{\dot{m}_i}{\dot{m}_p} \frac{I_b}{q} \frac{M}{\dot{m}} \tag{2.5}$$

Where I_b is the ion beam current and q is the charge of an ion. The thruster efficiency η_T is defined as

$$\eta_T = \frac{F^2}{2\dot{m} P_{in}} \tag{2.6}$$

Where P_{in} is the total electric power used by the thruster (Goebel and Katz, 2008).

2.2 Ionization Techniques

2.2.1 Electron Bombardment

The most common technique used to ionize propellant in an ion thruster is electron bombardment. Electrons are injected by a discharge cathode into the discharge chamber

where the propellant is confined; these electrons collide with the neutral propellant atoms, knocking electrons off the atoms and resulting in two negatively charged electrons and one positively charged ion (NASA,2012). NASA's NSTAR and NEXT thrusters and QinetiQ's T5 and T6 thrusters (all discussed in Section 2.4) use electron bombardment for ionization.

2.2.2 Electron Cyclotron Resonance

Another technique used to ionize propellant is electron cyclotron resonance. The propellant is confined within a magnetic field in the discharge chamber and microwaves are injected into this region at the electron cyclotron resonance frequency, as defined by the magnetic field **B** .

$$w_c = \frac{q\mathbf{B}}{M} \tag{2.7}$$

This energises electrons which collide with the neutral propellant atoms, resulting in ionization. The Japanese Space Agency's Hayabusa used electron cyclotron resonance to ionize the propellant, using magnetic rings ($\sim$ 0.3T) and a 2.4GHz wave emission (Ahedo, 2011).

2.2.3 Confining Propellant for Ionization

Efficient propellant utilization requires confinement of the propellant in order to allow maximum ionization; a magnetic field is often used to confine the propellant in order to maximise utilization (Ahedo, 2011). High strength magnets are placed around the edges of the discharge chamber; as electrons approach the discharge chamber walls they are redirected back into the centre of the discharge chamber by the magnetic field. This maximises the length of time the propellant atoms are within the discharge chamber and therefore maximising the chances of ionization and the propellant utilization (NASA, 2012).

2.3 Ion Thrusters Overview

2.3.1 Gridded Ion Thrusters - Principles of Operation

In a conventional gridded ion engine (GIE), ions are accelerated by means of an electric field generated by electrodes within the thruster known as the ion optics or grids. Each grid has thousands of apertures, which act as lenses to focus the ions through the grid, forming ion jets. Collectively these jets are known as the ion beam.

The grids on NASA's NSTAR ion engine have around 15000 apertures (Brophy, 2002); the apertures allow some of the neutral xenon gas to leak out, however the grid is designed to minimize the loss of un-ionized propellant (Brophy, 2002). The ratio of the mass flow rate in the form of ions in the exhaust to the total mass flow rate into the engine is called the propellant utilization efficiency, given in Eq. 2.5 (Brophy, 2002). The exhaust velocity of the ion beam depends on the voltage applied to the grids; this voltage is theoretically unlimited. As a large amount of positive ions are expelled in the ion beam, an equal

amount of negatively charged particles must also be expelled in order to keep the overall charge of the exhaust beam neutral. A cathode called the neutraliser is located in the downstream area of the thruster and expels the necessary electrons, preventing spacecraft charging. ESA's SMART-1 thruster uses xenon gas with a flow rate of 0.3mg/s through the neutralizer (Brophy, 2002).

GIEs normally use two or three grids; the screen grid, the accelerator grid and sometimes a deceleration grid. The screen grid is charged highly positive, the accelerator grid slightly lower but still positive and systems which use the deceleration grid have it charged slightly negative. Some systems include the deceleration grid in order to protect the accelerator grid from erosion due to backstreaming ions, which will be discussed in Section 3, but this greatly increases the complexity of the thruster. The grids are charged in this way to produce an electric field gradient in order to accelerate the particles. The ions are generated in the region of high positive charge and follow the electric field lines towards the area with the lower charge. The charges of the grids and the distances between them must be carefully chosen to maximise efficiency; at high voltage differences (approaching 5kV) between the screen and accelerator grids some ions collide with the second grid, (see discussion of erosion in Section 3), causing damage by increasing the aperture size via erosion of the grid material and thereby reducing the lifetime of the thruster (ESA, 2006). The Dual-Stage 4-Grid (DS4G) ion engine was developed to mitigate this problem and is discussed in Section 4. Grid transparency and alignment must satisfy conflicting requirements of maximising the extracted current, minimizing ion impaction on the grids, maintaining structural integrity and producing a low divergence ion beam (Ahedo, 2011), and research is still being undertaken in this area.

2.3.2 Other Electrostatic Thrusters - Non Gridded

GIEs are classed as electrostatic thrusters as they use electric fields to accelerate ions; other electrostatic thrusters include Hall Effect thrusters and FEEP thrusters, which have the advantage of using methods other than grids to produce the electric field to accelerate the particles, thereby removing the problem of reduced thruster lifetime due to grid erosion.

Field Emission Electric Propulsion Thruster

The Field Emission Electric Propulsion engine is a low thrust, high accuracy, non gridded electric propulsion system used for maintaining satellite positions. It produces between 0.01 and 0.1mN of thrust compared to 92mN produced by NASA's NSTAR thruster (ESA, 2009) and an I_{sp} of around 10,000s (Martinez-Sanchez and Pollard, 1998). The liquid metal caesium is used as propellant; it flows between a set of metal surfaces ending in a slit measuring one micron across (see Figure 2.1). The propellant is held in place by surface tension until an electric field is generated, causing cone shapes to be formed in the propellant which produce ions from the tips, generating thrust (ESA, 2009). Several tests have verified the operation of the FEEP thrusters and they will be used on ESA and NASA's joint mission LISA Pathfinder (Scharlemann *et.al.*, 2011). However the use of

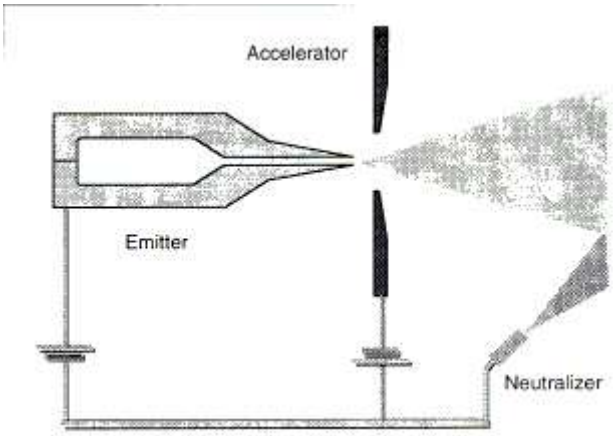

Figure 2.1: FEEP engine diagram (Marcuccio *et.al.*, 1997)

FEEP is limited by the very low thrust/power ratio, which limits the use of FEEP to low thrust precision control such as satellite stationkeeping (Martinez-Sanchez and Pollard, 1998).

Hall Effect Thrusters

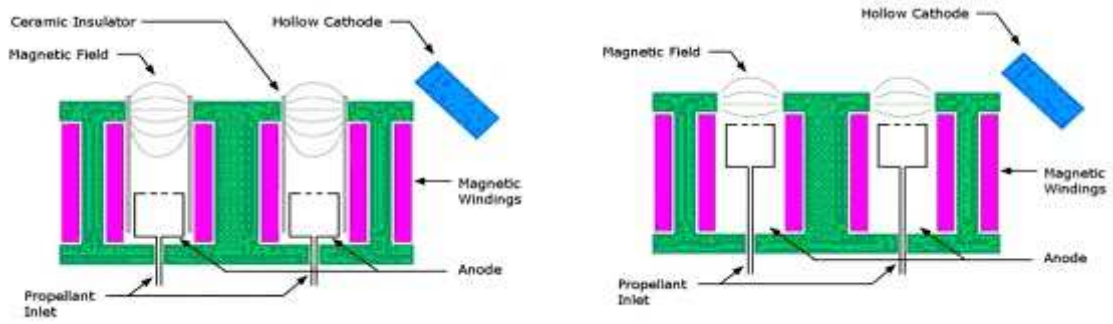

Figure 2.2: SPT Hall Thruster and TAL Hall Thruster diagrams (ESA,2004)

Hall Effect thrusters (HETs) (see Figure 2.2), or closed drift thrusters, can be classified as both electrostatic and electromagnetic. The propellant, usually xenon, is ionized by an electron current generated by a cathode; in order to produce an adequate plasma density for propulsion ($n_e =\sim 10^{17} - 10^{18} m^{-3}$) and near total propellant ionization, the axial electron current is inhibited by applying a near-radial magnetic field of a few hundred Gauss (Ahedo, 2011). The ions are highly magnetized and move with an azimuthal (**E**x**B**) drift (otherwise known as a Hall current) and are accelerated under the electrostatic field impressed by the negative cathode (Martinez-Sanchez and Pollard, 1998). The lower voltages, smaller amount of electric points to control and the larger ion current density compared to conventional GIEs make the HET electrically simpler and more compact than a conventional GIE. A commercial HET typically provides a specific impulse of 3000s - 8000s using xenon as a propellant, but has a low thrust efficiency of 50-55% (compared with 65-70% in a conventional GIE), a shorter lifetime and a larger plume divergence, which could potentially cause damage due to energetic particles impacting on the spacecraft (Ahedo,

2011). Hall Effect thrusters are divided into two types, stationary plasma thrusters (SPT) and thrusters with anode layer (TAL) based on geometric and material differences and the different physical processes that take place within the discharge plasma (ESA, 2004). The first use of a Hall effect thruster as the primary propulsion for space travel was on ESA's SMART-1 spacecraft, which was launched in 2003 and produced an average thrust of 67mN (Estublier *et.al.*, 2007). Modern HETs tend to be dual mode, enabling operation at high thrusts (such as for orbit insertion) or high specific impulses (such as for satellite stationkeeping) (Ahedo, 2011).

2.3.3 Electromagnetic Thrusters

Electromagnetic thrusters use magnetic fields to accelerate ions, thereby producing thrust.

Helicon Double Layer Thruster

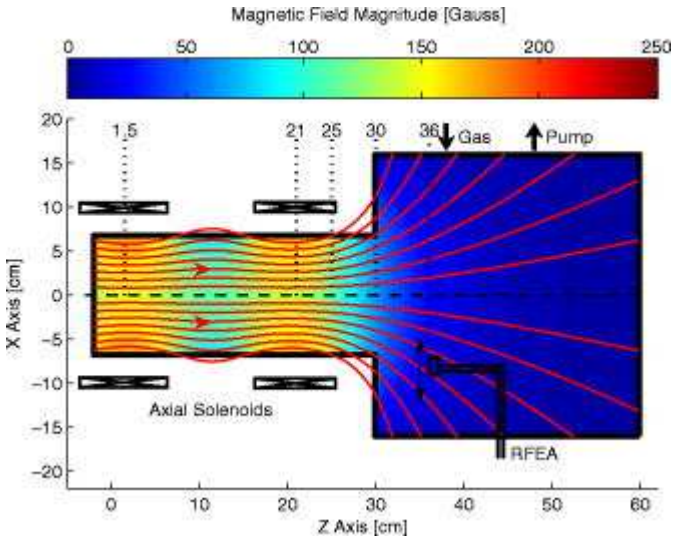

Figure 2.3: Top down schematic of HDLT attached to CHI KUNG diffusion chamber (Charles *et.al.*, 2008)

The Helicon Double Layer Thruster was developed by Australia National University. It generates thrust by accelerating a radio frequency (RF) generated plasma across a double layer that forms in the presence of a diverging magnetic field (Charles, 2009). The double layer is a strong drop in potential over a narrow distance within the plasma, which is formed during plasma breakdown and remains stable afterwards, and this electric field accelerates the ions (Charles, 2009). The Australia National University (ANU) is currently researching the HDLT; Figure 2.3 shows a top down schematic of the HDLT attached to the CHI KUNG diffusion chamber. The schematic shows the solenoids along with the corresponding magnetic field lines (shown in red) and magnetic field magnitude, and the retarding field energy analyser (REFA), which is used to measure the current versus discriminator voltage characteristic (Charles *et.al.*, 2008).

Magnetoplasmadynamic Thruster

The magnetoplasmadynamic thruster (MPDT) accelerates particles by way of the combined effects of a thermal pressure gradient and the Lorentz force defined in Eq. 2.8 (Ahedo, 2011). The Lorentz force is the force on a point charge (an idealized model of a particle with an electric charge) due to electromagnetic fields and is given by

$$\mathbf{F} = q(\mathbf{E} + \mathbf{v}x\mathbf{B}) \tag{2.8}$$

where q is the charge of the particle, **E** is the electric field and **B** is the magnetic field As the electric current returns to the power supply through the cathode a magnetic field of around 0.1T is created. This field reacts with the electric current flowing from the anode to the cathode, creating the Lorentz force (see Figure 2.4)(NASA, 2010).

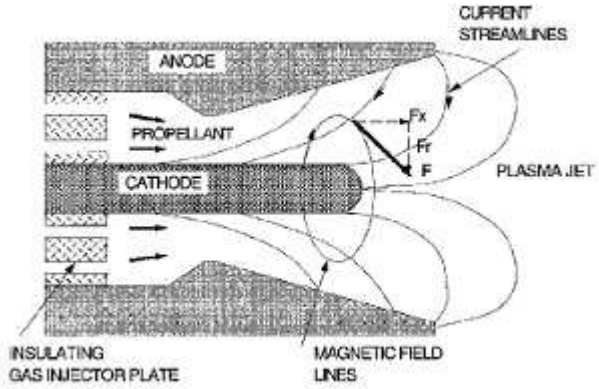

Figure 2.4: MPD Thruster diagram (Martinez-Sanchez and Pollard, 1998)

A low discharge current I_d between electrodes results in low magnetic pressure, $\mathbf{B} \propto I_d$, which results in poor mass utilization and high electrode losses. As a result of this the MPDT has the requirement of high discharge current, making it a high power device only (Ahedo, 2011). The MPDT has several shortcomings; thrust efficiency is low ($\sim 40\%$) due to high power losses at the electrode sheaths and the high ionization cost, secondly the electrode erosion rate is high, limiting the lifetime to below 1000h, and thirdly the high power requirement has hindered research and testing. It has been suggested that the use of lithium as a propellant and using multichannel hollow cathodes may reduce the cathode erosion while increasing thrust efficiency (Ahedo, 2011). The thrust is proportional to the magnetic pressure created by the thruster. Thruster efficiency of around 50% has been achieved in testing with hydrogen used as propellant and around 10N of thrust can be produced (Kubota, 2009).

VASIMR

The Variable Specific Impulse Magneto Rocket (known as VASIMR) uses a helicon plasma source, ion cyclotron resonance (ICR) to heat the plasma and a magnetic nozzle to accelerate the heated plasma. The VASIMR concept has been under development since the

early 80s; however it must still prove reliable operation and propulsive merits (Ahedo, 2011). Its advantages include the ability to vary the thrust and specific impulse generated by the rocket and it is suggested that if hydrogen is used as a fuel then due to hydrogen's properties as a radiation shield (hydrogen is effective in reducing neutron energies by elastic scattering processes) astronauts could be better protected against the dangers of radiation exposure during space travel (NASA, 2003).

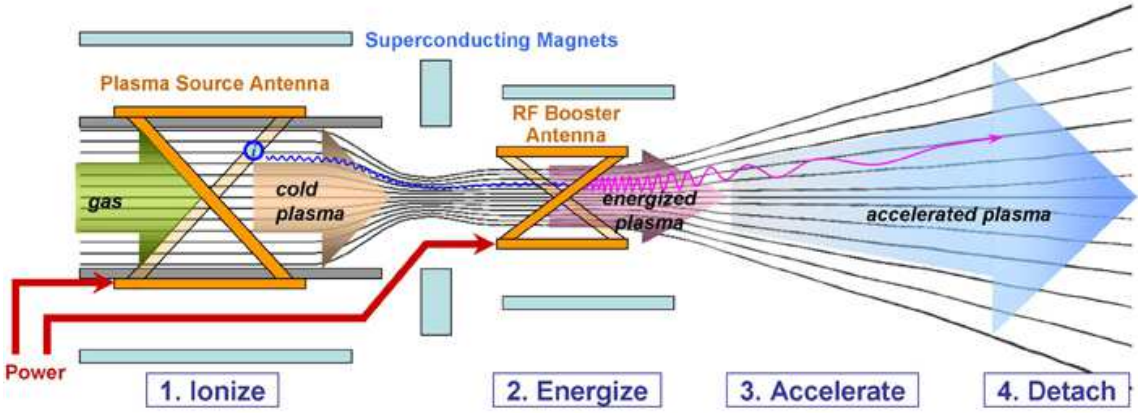

Figure 2.5: Diagram of VASIMR operation (Ad Astra, 2009)

The electrode-less design of the VASIMR (see Figure 2.5) makes it suitable for high power density and long component life due to a reduction in plasma erosion and other material complications (Longmier *et.al.*, 2011). Trajectory studies have shown that a propulsion system of this type offers substantial savings in system mass and/or flight time relative to fixed specific impulse thrusters (Glover *et.al.*, 2005). In VASIMR the available power is divided between the plasma source and the ion cyclotron resonance absorption (ICRA) system which delivers additional energy to the ions in the plasma (Glover *et.al.*, 2005). The engine has the potential for long lifetime, due primarily to the radial magnetic confinement of the plasma in the quasi-neutral flowing plasma stream, which acts to significantly reduce the plasma impingement on the materials of the rocket core (Longmier *et.al.*, 2011).

The gas (xenon, argon, but typically hydrogen) is injected into a tube surrounded by magnets and a series of two RF antennas (known as couplers). The section with the first RF coupler is known as the helicon section, in which a right-hand circularly polarized wave is launched into the plasma (Cassady *et.al.*, 2010). Utilizing this type of source to directionally produce a plasma flow into a high magnetic field with no wasted propellant is a key issue; scaling to a high magnetic field and power has proven to enhance the mass utilization of the thruster (Squire *et.al.*, 2007).

A balance has to be achieved between the mass flow rate of the propellant and the input RF power provided in the helicon stage to achieve an efficient helicon plasma source. The VX-200 prototype can utilize up to 40kW of RF power with a maximum flow rate of

150mg/s of argon propellant (Cassady *et.al.*, 2010).

The ionized gas, now a cold plasma (a 'hot' plasma is almost fully ionized whereas in a 'cold' plasma only a fraction of the propellant has been ionized), flows downstream and enters the second section of the engine. This section, with the second RF coupler, is known as the Ion Cyclotron Heating (ICH) section (Ad Astra, 2009). ICH was chosen as a result of a theoretical analysis performed by Breizman and Arefiev (2004) which indicated that virtually all the energy in an ion cyclotron wave would be transferred to ion perpendicular energy in a very small volume at a point on the gradient of a magnetic nozzle. Highly efficient absorption was predicted along with the prediction that all ions would receive nearly the same energy boost, meaning that ions would leave the nozzle with a narrow energy distribution (Glover *et.al.*, 2005). The plasma is energized further in this section, using left hand polarized slow mode waves launched from the high field side of the ion cyclotron resonance (Longmier *et.al.*, 2011). For a slow mode wave, the total pressure (the sum of particle pressure and magnetic pressure) is approximately constant across the background field. Field aligned gradients of the total pressure drive slow mode waves, and slow waves carry energy predominantly along the background field (Kivelson and Russel, 1995). In the ICH section of the VASIMR engine the plasma reaches temperatures greater than 10^6 (one million) degrees Kelvin (Ad Astra, 2009). This process differs from the ion cyclotron resonance utilized in tokamak fusion plasmas as the particles in the VASIMR engine pass through the coupler only once due to rapid absorption of ion cyclotron waves by the high speed plasma flow (Longmier *et.al.*, 2011). This motivated the elimination of the magnetic bottle which featured in the original design of the VASIMR engine (Glover *et.al.*, 2005).

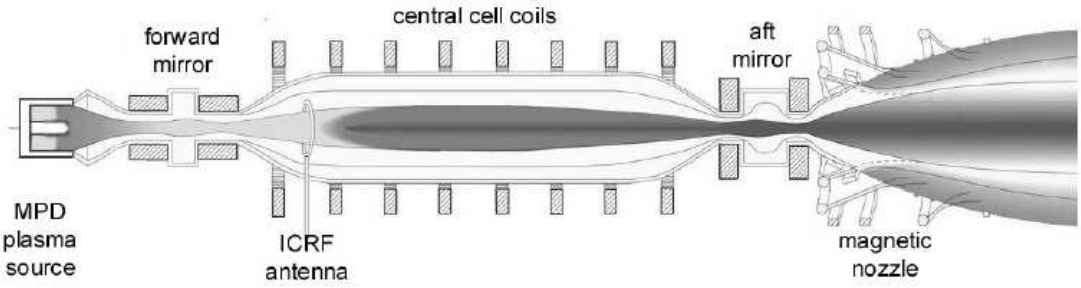

Figure 2.6: Old VASIMR concept - with magnetic bottle (Glover *et.al.*, 2005)

The 1980's VASIMR concept can be seen in Fig.2.6. The magnetic bottle is made up of the central cell coils and the magnetic mirrors, the aim of which was to trap the plasma while it undergoes ion cyclotron resonant heating (ICRH) (Glover *et.al.*, 2005).

The thermal motion of the ions around the magnetic field lines is mainly perpendicular to the direction of travel so the magnetic nozzle at the rear of the engine is needed to convert

this energy into a directed motion and thereby produce useful thrust (NASA, 2004). The plasma accelerates in an expanding magnetic field, a process described by conservation of the first adiabatic invariant μ, as the magnetic field strength decreases in the exhaust region of the engine (Longmier *et.al.*, 2011). The first adiabatic invariant is defined as

$$\mu = \frac{mv_{\perp}^2}{2\mathbf{B}} \tag{2.9}$$

It is conserved when the length scale of the variation of the magnetic field is much greater than the cyclotron radius of the motion.

$$\rho_L \ll L = \mid \frac{B}{\bigtriangledown B} \mid \tag{2.10}$$

2.3.4 A Comparison between Technologies

Ion Thruster	Propellant	Power Requirements (kW)	I_{sp} (s)	Max Thrust (mN)
NSTAR	Xenon	2.3	1900-3100	92
NEXT	Xenon	7.7	4300	236
HiPEP	Xenon	20-50	6000-9000	670
DS4G	Xenon	250	19,300	2500
Hall Effect T220	Xenon	10	2450	500
FEEP	Liquid Caesium	0.006	10,000	1
Helicon Double Layer Thruster	Hydrogen and others	1.5	2000	90
MPDT	Hydrogen, Lithium	100	10,000	100,000
VASIMR	Xenon, Argon	200	30,000	5700
T5	Xenon	4.3	3550	166
T6 model thruster	Xenon	4.5	4300	143

Table 2.1: Table showing a comparison between the power requirements, thrust and specific impulse for several ion thrusters that are currently being researched or have been used in the past. For thrusters that have not yet been flown in space, such as the Dual-Stage 4-Grid thruster, values come from theory and experimentation

It can be seen from Table 2.1 that the VASIMR can produce the highest specific impulse of the thrusters compared above, and has the second highest power requirement after the Dual-Stage 4-Grid (DS4G) ion thruster. The FEEP thruster has the lowest power requirement, but also produces the lowest thrust. It can be seen that xenon is most commonly used as a propellant.

2.4 Past, Current and Future Research and Missions

2.4.1 History and Past Missions

Ion thrusters were first used in space in 1964 when two thrusters were launched on a brief ballistic flight, known as Space Electric Rocket Test 1 (SERT 1), during which the 8cm

cesium contact ion thruster failed to operate due to a high-voltage electrical short circuit while the 10cm mercury electron bombardment thruster operated successfully for 31 minutes (NASA, 2008). This mission was followed by SERT II and an Advanced Technology Satellite (ATS 6), which demonstrated the long lifetime achievable by electric propulsion (Wilbur *et.al.*, 1998). Many more successful tests followed and ion propulsion systems have been widely used for satellite stationkeeping. Electron bombardment ion engines with diameters of 1.3cm to 150cm and input powers of 7W to 130kW have been built and tested (Brophy, 2002). The first time an ion propulsion system was used as the main means of spacecraft propulsion was the NASA Solar Technology Application Readiness (NSTAR) thruster which was used on the Deep Space 1 spacecraft (DS1) from 1998 to 2001. The NSTAR engine was remotely programmable from the ground, enabling engineers to adjust the operation of the thruster as necessary. DS1 achieved an exhaust velocity of 35kms, much greater than the maximum of 4km/s exhaust velocity achieved by a chemical rocket (Deep Space 1, 2001). The NSTAR engine had a screen grid voltage of 1075V, accelerator grid voltage of -180V and could deliver a total ΔV of 4.5km/s (Brophy, 2002). The operating parameters of the NSTAR ion engine were chosen to minimise the production of doubly charged ions, which are responsible for most of the erosion that occurs inside the discharge chamber. When operating at full power, approximately 11% of the ion beam current is composed of doubly charged ions (Brophy, 2002).

ESA's Gravity field and steady-state Ocean Circulation Explorer (GOCE) is the first in a series of 'Earth Explorer Core Missions' and was launched in March 2009 with the goal of mapping the Earth's gravity field. The original 12 months of mapping were completed in 2011, but due to lower fuel consumption than anticipated ESA decided to extend the mission to the end of 2012 (ESA, 2012). The satellite flies in a sun-synchronous dawn-dusk orbit at an altitude of 260km. GOCE uses a QinetiQ T5 Kaufman-type ion thruster with a 10cm diameter for stationkeeping; it has a thrust range of 1 to 20mN with operating power between 55W and 585W and produces a specific impulse ranging between 500s and 1500s. One stated requirement for the GOCE mission thruster was a minimum lifetime of 1000 on/off cycles and the T5 can provide 8500 on/off cycles (Edwards *et.al.*, 2004).

In 2003 the Japanese Aerospace Exploration Agency (JAXA) launched the MUSES-C/Hayabusa mission with the aim of landing the craft on an asteroid in order to collect samples and then returning it to Earth. Hayabusa was the first spacecraft to perform a flyby of Earth using an ion engine as the main thrusters (The Planetary Society, 2010). It carried 65kg of propellant for the ion engine and reached peak thrust of 0.015N, achieving a velocity of 4km/s and a ΔV of 1.4km/s (Kuninaka, 2008). Microwave discharge ion engines were used, which employ electron cyclotron resonance (ECR). Solid electrodes were eliminated in the ECR section in order to make the ion engines more durable and reliable, as in traditional ion engines the solid electrodes are critical parts and cause flaking of sputtered material, leading to grid shorts (Kuninaka, 2008). Hayabusa's ion engines had a diameter of 10cm; four engines were installed and three can generate thrust simultaneously

(Kuninaka, 2008). However JAXA has had trouble with the ion engines on the Hayabusa spacecraft. Of the four engines, A, B, C and D, thruster A was never used due to the engine being found to be 'unstable' after launch, thrusters B and D failed due to failed neutralisers, and the neutraliser in thrusters C was near failure during 2010. However JAXA engineers discovered a way around this problem; they used the neutraliser from thruster A to neutralise the ion beam from thruster B (The Planetary Society, 2010). With thruster C operational and kept in reserve, and thrusters A and B working in this configuration, Hayabusa returned to Earth in June 2010 (JAXA, 2010). Combining two thrusters in this way has never been tested on Earth but an emergency circuit enabled the engineers to modify the thrusters in this way. The two thrusters working together requires twice as much power as is standard; 5kg of propellant was needed to gain 0.2km/s acceleration over 2000 hours (The Planetary Society, 2010).

ESA used ion propulsion on the SMART-1 mission which launched in 2003 and aimed to halo orbit the moon and use infra-red and x-rays to search the south pole of the moon for water. The SMART-1 mission made use of the Hall effect, whereby a current flowing across a magnetic field creates an electric field directed sideways to the current, which is used to accelerate the ions. Solar panels were used to power the mission and the engine generated a thrust of 0.07N, accelerating the spacecraft at a rate of 0.2 millimetres per second per second (ESA, 2009a). At launch, SMART-1 carried 82kg of xenon. As electric propulsion (EP) can produce undesired effects such as contamination and erosion of surfaces due to deposition of sputtered material and ion impingement, SMART-1 was fitted with the EP Diagnostics Package (EPDP). A retarding-potential analyzer (RPA) measured the ion energy and current density distribution, a Langmuir probe (LP) measured the plasma potential, electron density and electron temperature and a quartz-crystal microbalance (QCM) provided contamination data (Estublier, 2008). A summary of these missions along with current and planned missions utilizing ion thrusters as the method of propulsion is provided in Table 2.2.

2.4.2 Current and Future Missions

There are several interesting missions planned for the near future which will utilize the technology of ion propulsion.

The main aim of NASA's Dawn mission is to investigate the conditions and processes acting at the beginnings of the solar system by studying two complementary protoplanets within the asteroid belt, Ceres and Vesta (Rayman *et.al.*, 2006). Dawn launched in September 2007, arrived at Vesta in July 2011 and spent 14 months orbiting the rocky asteroid. It departed Vesta in September 2012 and is due to arrive at Ceres in February 2015; the primary mission is scheduled to end in July 2015 (NASA, 2011). The ion propulsion system is an expanded version of that used on Deep Space 1 and consists of three 30cm thrusters. At the maximum thrust level, with an input power of 2.6kW the thrust is 92mN and at the lowest input power of 0.5kW the thrust is 19mN. The specific

impulse produced ranges between 1900s and 3200s (Rayman *et.al.*, 2006).

Researchers at Ad Astra have developed a VASIMR prototype, the VX-200, which is currently undergoing testing in a vacuum facility. Operating with argon propellant, the prototype reached full power in September 2009 and produced thrust of 5.7N with thruster efficiency of 72% (Ad Astra, 2009). Ad Astra expect to send a flight version of the VASIMR, the VF-200, to the International Space Station in 2014, where performance can be measured without the pressure constraints found in ground based space simulation chambers (Ad Astra, 2009).

BepiColombo is a joint mission between ESA and the Japan Aerospace Exploration Agency (JAXA) under ESA leadership. The BepiColombo mission consists of two spacecraft which will orbit Mercury; the Mercury Planetary Orbiter built by ESA which will study the surface and interior of the planet, and the Mercury Magnetospheric Orbiter built by JAXA which will study the magnetosphere. It is due to be launched in 2016 and should arrive at Mercury in January 2024 (ESA, 2012a). The BepiColombo transfer module will be equipped with four of QinetiQ's T6 ion thrusters, an update of the T5 thruster currently in use on ESA's GOCE spacecraft. A prototype of the T6 was tested at the Jet Propulsion Laboratory; at full power (4.5kW) it produced 143mN of thrust and a specific impulse of 4120s with efficiency of 64%, and optimization for lower flow rates produced a specific impulse of 4300s with efficiency of 66% (Snyder *et.al.*, 2010).

The LISA (Laser Interferometer Space Antenna) Pathfinder is a joint ESA/NASA mission to demonstrate the Laser Interferometer Space Antenna technologies in free-fall, including Gravitational Reference Sensing, drag-free attitude control, micro-Newton thrusters and interferometry with free falling mirrors (ESA, 2012b).The reason for this mission is that some of the technology cannot be used on the ground due to Earth-induced noise (McNamara, 2009) The LISA Pathfinder will carry two payloads, ESA's LISA Technology Package (LTP) which aims to demonstrate that a test mass can be put in a pure gravitational free-fall within one order of magnitude of the requirements of LISA, and NASA's Disturbance Reduction System (DRS), which will maintain the position of the spacecraft with respect to the proof mass (ESA, 2012b). The LISA Pathfinder will use FEEP thrusters which have been developed to match the mission requirements; it will be the first time that ESA will operate a spacecraft with micro-Newton thrusters as the only form of propulsion (ESA, 2012b). It is due to launch in 2014 and the operational phase of the mission will last for approximately 12 months.

Mission Name	Organization	Mission Dates	Propulsion System
SERT 1	NASA	1964	Cesium contact - failed; Kauffman type - successful
SERT 2	NASA	1970 - 1981	Kauffman type
Deep Space 1	NASA	1998 - 2001	NSTAR thruster
GOCE	ESA	2009 - 2012	T5
Hayabusa	JAXA	2003 - 2012	Microwave discharge
SMART-1	ESA	2003 - 2006	Hall effect
Dawn	NASA	2007 - present	Expanded version of NSTAR
BepiColombo	ESA / JAXA	2015	T6
LISA Pathfinder	ESA / NASA	2014	FEEP

Table 2.2: Table showing a summary of past, current and planned missions utilizing ion thrusters as the method of propulsion

This chapter has introduced the concept of ion thrusters, providing an overview of the techniques in use today and the differences between the main types of ion thrusters. A table has been provided for comparison purposes showing performance parameters for a selection of thrusters currently being researched or have been researched in the past, and the use of ion thrusters in past, current and future missions as been discussed. The next section will examine work published by other researchers, focusing on the simulation of ion thrusters.

3 Literature Review

In this section a range of research using simulation codes to study ion thrusters is examined, with the main topics of research being plasma flow through the ion optics, erosion of the ion optics, the effects of varying the grid potentials and charge-exchange collisions. As the aim of this work is to produce a functioning simulation code, it is important to have knowledge of the research that has already been done and the techniques that are in use; this will provide an opportunity to see where any potential gaps in the knowledge base may exist, and to find the most appropriate techniques and up to date theories in order to complete this work.

Wang *et.al.* (2003a) state that ion engines present a wide range of problems relating to plasma flow. They note that plasma flow can be separated into four categories

1) Plasma flow inside the discharge chamber
2) Ion optics plasma flow
3) Near-spacecraft thruster plume – generally focusing on the interactions between the ion thruster plume and the thruster itself
4) Far-field thruster plume – generally focusing on interactions between the thruster plume and the space plasma environment

The research in this thesis is investigating the ion optics plasma flow with regard to performance parameters and rates of erosion. The ions are focused through the thruster by the grids, forming beamlets of ions which combine at the thruster exit to form the thruster plume. The rate of erosion of the ion optics is key in determining the lifetime of the thruster; however it is important to balance the expected lifetime of the thruster with other key performance parameters such as specific impulse, thrust, change of momentum and power efficiency.

Several plasma simulation codes exist, including OOPIC (Tech-X, 2012), VORPAL (Tech-X, 2012), IGUN, and PBGUNS (FAR-TECH, 2012). Often a particle-in-cell (PIC) code is used to simulate charged ions, where each simulation ion represents a large number of real ions. The PIC technique is described in Section 5.

Detailed investigation has been done into the plasma flow around the ion optics by many researchers; several simulations have been developed and some researchers have compared their simulation results with experimental results to validate their models. Peng *et.al.* (1993) developed a 2D single aperture PIC-MCC (particle-in-cell - Monte Carlo collision) code and extended it to a 3D multiple aperture simulation using a null MCC technique to study grid erosion due to charge-exchange (CEX) ions; Wang *et.al.* (2003a) developed a 3D PIC-MCC multi-aperture code to study erosion of the NSTAR thruster optics; Tartz *et.al.* (2008) developed a code based on IGUN to perform 2D simulations in order to study sputtering and erosion of ion optics; Chang *et.al.* (2008) developed a 3D PIC-MCC

code using a null Monte Carlo collision (MCC) technique to study plasma flow through the optics and 'pits and grooves' erosion; Zhong *et.al.* (2010a) developed a 2D axisymmetric PIC code to study the influences of accelerator grid voltage on the plasma sheath upstream of the screen grid and the ion extraction through typical ion optics; Sun *et.al.* (2010) developed a 2D PIC-MCC code to investigate the erosion of ion optics within a three-grid electron cyclotron resonance (ECR) ion thruster. The Monte Carlo Collisions (MCC) method is often combined with the PIC method and is a way of modelling collisions between particles, in which each particle is tested for a collision and the appropriate action is performed if a collision occurs. Coletti *et.al.* (2010) and Coletti and Gabriel (2010) used an ffx code to study dual-stage thrusters, presenting parameters for the ion optics in order to achieve specific impulses of 10,000s and 61,000s and investigating the possible lifetime of the Dual-Stage 3-Grid (DS3G) thruster. The results of the work by Coletti *et.al.* and Coletti and Gabriel will be compared with results obtained from the simulation code written for this thesis in order to verify the performance of the code. Dual-stage ion thrusters will be discussed in more detail in Section 4.

When the ion beamlets are well focused (meaning there is no direct primary ion impaction on the accelerator grid), accelerator grid erosion is caused by the formation of charge-exchange ions; as the velocity of these ions is negligible when they are created, the erosion pattern is determined by the electric field in the deceleration region (Peng *et.al*, 1993). There is a potential gradient in the transverse direction (perpendicular to the beam propagation direction) due to the positive space charge in the ion beamlet and this gradient forces CEX ions out of the primary beam and into the geometric centres between apertures. Experimental observation [(Patterson and Verhey, 1990) and (Rawlin, 1988)] have shown that maximum accelerator grid erosion occurs at the geometric centre between apertures for a hexagonal geometry two-grid accelerator system (Peng *et.al.*, 1993).

Peng *et.al.* (1993) used a modified 2D PIC-MCC simulation method to study this problem. The original 2D single aperture model did not produce the erosion pattern found in ground tests, so the researchers extended the code to a 3D multiple aperture code in which the hexagonal symmetry of the grids was modelled explicitly, which did produce the pitted pattern observed in ground tests. As the hexagonal symmetry was assumed the simulation used a cross section with a 30 degree by 60 degree triangle, comprising only one twelfth of an aperture. As the charge-exchange collision rate is energy and time dependant a null collision Monte Carlo technique was used in the simulation to simulate charge-exchange collisions and sputtering, which will be discussed in more detail in Section 3. The mean extracted ion velocity was determined using the Bohm criterion (where the velocity is determined from the electron temperature and the ion mass) with an assumed electron temperature of 1.5eV. A neutral plasma was assumed to exist at the upstream boundary of the simulation domain and the plasma density was determined from a given beam current of 3.2A. Sputtering yields for xenon ions impinging on a molybdenum surface were taken from Rosenberg and Wehner (1962) and it was assumed that sputtering

yield is independent of the angle of incidence of the impacting ions. Sputtering yields for molybdenum range between 0.06 atoms/ion at an ion energy level of 100eV to 1.06 atoms/ion at an ion energy level of 600eV (Rosenberg and Wehner, 1962). It was also assumed that no geometry changes resulted from the sputtering process. This means that the calculations are valid only for small erosion depths and the simulation is said to be unsuitable for results comparison with experiments in which full penetration of the grid material occurs.

The 3D code produced the concentration of sputtering between grid apertures as seen in experiments and Peng *et.al.* (1993) stated that

> *'the roughly triangular shape and orientation of these erosion contours are exactly the same as observed in experiments'.*

In experiments the mass loss from the downstream surface of the accelerator grid was around 17.8g whereas the simulation produced a result of 23.3g after 890 simulated hours. The approximate total mass of the simulated grids are not stated in the research paper.

Wang *et.al.* (2003a) presented an overview of results from ion thruster modelling studies performed in support of NASA's Deep Space 1 mission and NSTAR thruster, focusing on ion optics plasma flow and near-spacecraft plume. The simulation code used in this work was originally developed in 1993. For computational efficiency the researchers built upon the orthogonal grids and a finite-difference based formulation. An orthogonal grid is where the grid is formed by two sets of lines perpendicular to one another, producing a grid of squares. A method of sub-gridscale placement of boundaries explicitly includes the location of the ion optics in relation to the grid in the finite-difference form of Poisson's equation.

$$\nabla^2\phi(x,y) = \frac{-\rho(x,y)}{\epsilon_0} \tag{3.1}$$

(Birdsall and Langdon, 1985)

where $\rho(x,y)$ is the charge density of the system and $\epsilon_0 = 8.854x10^{-12}F/m$ is the permittivity of free space. ϵ_0 is often set as 1 within simulation codes in order to simplify the code.

Poisson's equation (Eq.3.1) becomes the five-point finite difference form shown in Eq.3.2 in two dimensions and is then solved for all of the potential $\phi_{j,k}$ including all appropriate boundary conditions. The aim of finite difference equations is to find an approximate solution to differential equations. In the finite difference method the derivatives in the differential equations are replaced with finite difference approximations, resulting in a finite algebraic system of equations to be solved in place of the differential equation (LeVeque, 2007).

$$\frac{(\phi_{j-1} - 2\phi_j + \phi_{j+1})_k}{\Delta x^2} + \frac{(\phi_{k-1} - 2\phi_k + \phi_{k+1})_j}{\Delta y^2} = -\rho_{j,k} \tag{3.2}$$

(Birdsall and Langdon, 1985)

Where Δx and Δy are the mesh spacings in the x and y directions. The main part of the simulation used by Wang *et.al.* (2003) has a formulation similar to other ion optics codes [such as that used by Peng *et.al.* (1993)] and is a particle-ion Boltzmann-electron PIC-MCC code for simulations on ion time scale. A 3D PIC code is used, in which multiple apertures can be included explicitly in the simulation domain. Wang *et.al.* (1998) stated that the complex geometries of ion optics are best simulated using tetrahedral cells or unstructured grids and finite-element based formulations to match the geometry of the optics, although this can be significantly more computationally intensive than a standard orthogonal grid PIC code. In the orthogonal grid code the location in memory of quantities defined in neighbouring cells can be found trivially via indexing, while in an unstructured grid the neighbours of a cell must be found by lookups in a table or other methods requiring additional memory references (*ibid.*). No assumptions were made to simplify the upstream and downstream boundary conditions, and the upstream sheath and ion beam extraction from the discharge plasma were determined self-consistently in the simulation.

The model includes three PIC codes, an ion beamlet code, a neutral particle code and a charge-exchange ion code. The propellant ions, charge-exchange ions and neutrals are treated as macro-particles and the electrons are modelled as an isothermal fluid. In the simulation the ion beamlet code is used to simulate ion beam extraction from the discharge plasma and the neutral particle code is used to track the flow of the un-ionized particles of propellant. Once a steady state was achieved for beam ions and neutral particles they were frozen and the charge-exchange ion code was activated, in which particles representing charge-exchange ions are generated in the simulation domain according to the calculated volumetric charge-exchange ion production rate using Equation 3.3.

$$\frac{dn_{cex}}{dt} = n_b(\overrightarrow{x})n_n(\overrightarrow{x})v_b\sigma_{cex} \tag{3.3}$$

(Wang *et.al.*, 2003a)

where the beam ion density $n_b(x)$ is determined by the ion beamlet code and the neutral density $n_n(x)$ by the neutral particle code. The charge-exchange ion collision cross section σ_{cex} is based on experimental data by Pullins *et.al.* (2000).

The code was applied to the ion optics plasma flow for the NSTAR ion thruster, performed for the nominal conditions presented in Table 3.1. The number of cells used in the simulation domain is 30x30x400 with a grid resolution corresponding to the Debye length in the discharge plasma ($\lambda_D \approx 0.0037$cm). The Debye length gives an estimate of the spatial scale over which a plasma ion influences its surroundings, for example a spacecraft can develop a net charge, which will perturb the plasma in the immediate vicinity of the spacecraft. This region is known as the plasma sheath, and the scale size of this region will be λ_D (Kivelson and Russel, 1995). The approximate number of macro-particles used in

the simulation is 1.8 million and that used in the charge-exchange simulation is 9 million. Wang *et.al.* (2003a) describe the process of the simulation as follows:

> *'The propellant ions are extracted from the upstream discharge plasma to form beamlets through the apertures. The beamlets eventually become mixed and neutralized in the far-downstream region. The charge-exchange ions born downstream of the accelerator grid, on the other hand, will backflow towards the accelerator grid'.*

By tracking the ions that impinge upon the grid, the distributions of impingement current density, incident energy and incident angle on the grid surface can be obtained. This allows the depth of erosion on the grid due to charge-exchange ion impingement to be calculated.

The nominal geometric and operating parameters for the NSTAR ion engine optics were given as follows:

	Hole diameter	Grid thickness	Voltage
Screen grid	1.91mm	0.38mm	1074V
Accelerator grid	1.14mm	0.51mm	-180V
	Centre-to-centre hole spacing	Screen-to-accel grid gap	Total accelerating voltage
	2.21mm	0.58mm	1100V

Table 3.1: Geometric and operating parameters for the NSTAR ion engine (Wang *et.al.*, 2003a)

During testing of the NSTAR thruster, laser profilometer measurements and post-test destructive examinations were performed to measure erosion on the accelerator grid; these measurements were used to validate the simulation model. When the measured erosion pattern and depth were compared with the simulation results it was found that

> *'the simulation not only accurately predicts the erosion pattern but also gives excellent quantitative agreement with erosion measurements'*
>
> (Wang *et.al.*, 2003a)

Tartz *et.al.* (2008) developed a 2D grid erosion simulation, in which the ion beam and grid erosion features were simulated for a given grid configuration and thruster parameter set and was then extended to a dynamic simulation, allowing the evolution of grid erosion with operation time to be studied when taking mission profiles into account. They state that the simulation has been validated by experimental results obtained from short erosion experiments, a 3,000 hour accelerated wear test performed by IOM and EADS Space Transportation on the RIT-10 and RIT-22 thrusters.

A commercial 2D ion trajectory code 'IGUN', a code written for simulating ion extraction from plasmas, has been used for the simulation of ion extraction and single beamlet

formation. The neutral density distribution, caused by neutral particles escaping from the plasma chamber, was simulated under the assumption of molecular flow and diffuse reflection by the walls and grid surfaces. Due to the axial symmetry of the grid hole the calculations were performed in two dimensions. The charge-exchange density was obtained from the neutral density and the beamlet ion current density, and as the charge-exchange ions are said to only have a weak influence on the beamlet space charge distribution due to the small number of CEX ions compared to the primary ions, the new ions can be inserted into the original IGUN simulation of the beamlet. For the sputter yield model a revised version of the Bohdansky formula shown in Eq.3.4 combined with the Yamamura formula shown in Eq.3.6 was used. Sputtering is defined as the removal of surface atoms from solid surfaces within the discharge chamber, including the discharge chamber walls and ion optics, due to the impaction of energetic particles. Sputtering is quantified by the sputtering yield, Y, which is defined as the mean number of atoms removed from the impacted surface per incident ion (García-Rosales *et.al.*, 1994)

$$Y(E_{0,\alpha=0\,^\circ\mathrm{C}} = Q s_n^{TF}(\varepsilon)(1-(\frac{E_{th}}{E_0})^{2/3})(1-\frac{E_{th}}{E_0})^2 \tag{3.4}$$

where E_0 is the projectile energy, α is the angle of incidence, s_n^{TF} is the nuclear stopping cross section of the atom and ε is the reduced energy, given by

$$\varepsilon = E_0 \frac{M_2}{M_1+M_2}\frac{a_L}{Z_1 Z_2 e^2} \tag{3.5}$$

(Garcia-Rosales *et.al.*, 1994)

M_1 and M_2 are the masses of the projectile and the target atom respectively, Z_1 and Z_2 are the nuclear charges, a_L is the Lindhard screening length and e is the electron charge.

$$Y(E_0,\alpha) = Y(E_0,\alpha=0)(cos\alpha)^{-f} exp\{f[1-(cos\alpha)^{-1}]cos\alpha_{opt}\} \tag{3.6}$$

(Yamamura *et.al.*, 1983)

where α_{opt} is the angle which corresponds to the maximum of the sputtering yield.

Parameters were determined from measurements the researchers made of relevant grid materials. The erosion rate profile on the grid surfaces led to changes of the grid hole profile. The IGUN simulation code was extended to investigate the time evolution of the erosion; once the original simulation finished the erosion was simulated for a predefined time step, assuming constant beamlet and erosion parameters during the time period. Each surface point was moved according to the local erosion rate and any loops that formed within the code were removed. The simulation was then restarted with the new grid shape and this was repeated until either the defined time limit was reached or the grid was said to be 'substantially damaged'. It was found that the lifetime estimate based on the starting erosion patterns produced too short a lifetime estimate due to the erosion pattern changing over time.

Tartz *et.al.* (2008) define the end-of-life of the accelerator grid as the time when the first accelerator grid hole diameter (originally 1.2mm in diameter on the RIT-XT thruster) reaches the screen grid hole diameter (1.9mm in diameter on the RIT-XT thruster); they state that this is a conservative definition because with such a grid structure further operation would be expected.

	Measured	Simulated
I_{acc}	0.6mA	0.54mA
I_{decel}	0.05mA	0.03mA
Mass loss accelerator	0.11mg/h	0.09mg/h
Ave. erosion rate	61nm/h	70nm/h
Mass loss decelerator	0.02mg/h	0.049mg/h
Ave. erosion rate	$\approx$0	2.8nm/h

Table 3.2: Comparison between measured and simulated results (Tartz *et.al.*,2008)

In order to validate the simulation an accelerated grid wear test was performed on a three grid system made from high density graphite. The test was performed at 'erosion accelerated' conditions at a low mass utilization of 47%, in which erosion was increased in a '*well defined*' way. A good agreement with simulated values was achieved, in which a smooth centered erosion profile (the shape formed by erosion) on the downstream side and an almost flat erosion profile on the upstream side was produced. It was extrapolated that, assuming steady erosion, the end-of-life state would be reached after 5000h. After 1300h of testing a centre-dented erosion profile evolved on the upstream side; It was stated that this profile could not be explained by the considered erosion process and it was assumed that this resulted from changes in plasma properties occurring after this time. A comparison between measured values and simulated values can be seen in Table 3.2.

Chang *et.al.* (2008) defined two accelerator grid end-of-life scenarios; firstly that the grid lifetime may be defined by the point where electron backstreaming can no longer be prevented by the existing power supply due to aperture enlargement, or secondly by structural failure due to 'pits and grooves' material loss. It is stated that the first scenario is believed to dominate grid erosion in a space where neutral particles for charge-exchange collisions come only from the thruster and not background gas present in a testing facility. They presented a three-dimensional PIC-MCC code which was applied to model ion optics plasma flow for a 20cm ion thruster. An 800 hour experiment was performed and the erosion depth of the accelerator grid was measured using the Depth-From-Focus (DFF) method; these measurements were compared with the simulation results. DFF is a method of extracting depth information from two dimensional images, and was chosen for use in this case because of the difficulty in measuring erosion due to the small dimensions of the grid structure.

The simulation was based on Birdsall and Langdon's (1985) PIC method and used Xenon gas with molybdenum optics. The MCC method with the null-collision technique was used to simulate the CEX collisions between the Xenon atoms and ions. Only primary

ions were included in the model, secondary ions were ignored, as the primary ions form the main part of the extracted ion beam. The four planes parallel to the z axis used Neumann boundary conditions. The Neumann boundary condition gives the normal derivative $\frac{d\phi}{dn}$ on a surface, often set as 0. Test particles were injected into the simulation domain at each time step; test particles were assumed to start their trajectories at the upstream boundary with a Bohm velocity, which is determined only from the electron temperature and the ion mass, in the z direction and Maxwellian velocity in the x and y direction. One test particle in the simulation represented around 500 propellant ions and there was around 700,000 test particles in the simulation. In each time step the particles were accelerated by the electric field; Newton's 2nd law was applied to the movement of the test particles and the density of the electrons was given by the Boltzmann relationship. The electron temperature at the upstream boundary was 5eV and at the downstream boundary was 15eV.

It was seen in the simulation that the Xenon ions were focused and extracted by the ion optics to form an ion beam. All particles passed through the grid hole and none directly impinged on the grid as a result of the focusing of the beam. It was seen that the potential contours in the simulation domain changed once the test particles entered the simulation domain. The potential iso-surfaces in the downstream region of the accelerator grid, which were originally flat planes, became strongly concave. The reason given for this change is that the ion number density n_i and electron number density n_e changed in Eq.3.7 after the entrance of the test particles. The Xenon ions were accelerated towards the grid surfaces by the concave electric field and produced the 'pits and grooves' erosion pattern that can be seen in Figure 3.1.

$$\bigtriangledown^2\phi = -\frac{e}{\varepsilon_0}(n_i - n_e) \tag{3.7}$$

Chang *et.al.* (2008) stated that the electron density distribution mainly depends on the local electric potential distribution. It was expected that electrons should be restricted in the discharge chamber and the ion beam downstream of the calculation domain and it was shown in the simulation results that this happened as expected. It was found that the boundary of electrons was concave, as can be seen in Figure 3.2, which was said to show that the plasma in the discharge chamber had a concave sheath; this result agreed with experimental results.

It was also stated that after a CEX collision, if the energy of the CEX ion was high enough it would hit the grid surface and lead to erosion. No threshold energy value for erosion was provided in the research paper. The 'pits and grooves' erosion pattern was found, where the most severe erosion lies in the centre of three grid holes and erosion is also found between these pits. This erosion pattern can be seen in Fig.3.1. This 'pits and grooves' pattern that was found was said to be in good agreement with reported patterns found in previous research. Chang *et.al.* state that the simulation results are '*reasonably consistent*' with the measured erosion depth, except in the simulation region $x > 0.2$ where a

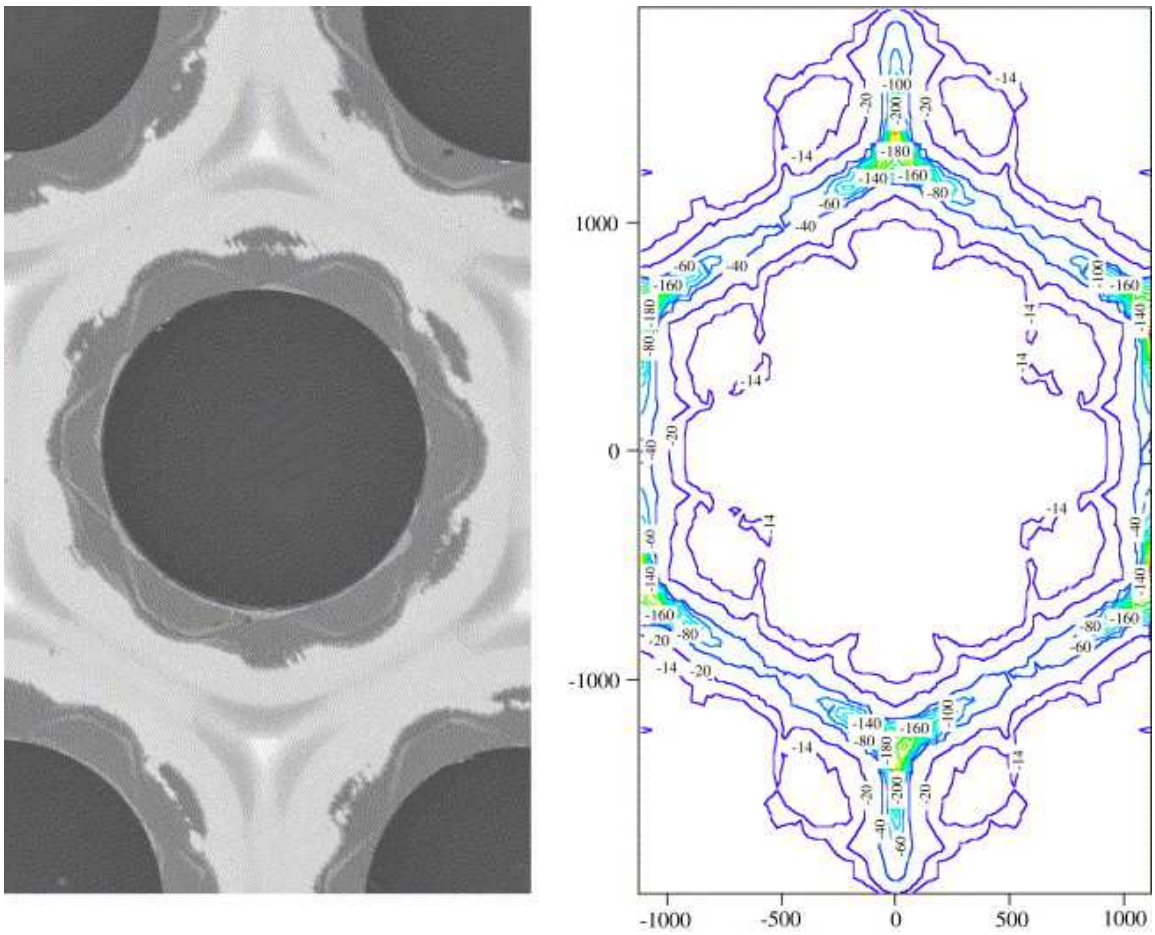

Figure 3.1: Erosion pattern around a single aperture on the downstream face of the accelerator grid of the NSTAR thruster: photograph(left) and results from a simulation performed by Wang *et.al.* (2003a)

large difference is found between the simulation result and measured data. It is suggested that this is due to a modelling error in the simulation - what type of error is not stated.

The relationship between the accelerator grid current and potential was studied and it was found that the accelerator grid current decreases with increased grid potential. The reason given for this is that when the potential increases, the plasma in the discharge chamber is focused into an ion beam and extracted by the optics, and therefore the grid current decreases. Grid current is caused by two types of impingement of charged particles on the grid surface; firstly if the plasma is not well focused into beamlets then ions would impact on the grid surface, and secondly any ions generated in CEX collisions would be attracted by the negative potential of the accelerator grid and impinge on the grid surface. CEX ions can impact on different parts of the accelerator grid; in this research only erosion of the downstream surface of the accelerator grid was studied, but the authors state that the impingement of ions on the grid hole's wall, which will enlarge the hole, is a serious problem (known as barrel erosion) and will be studied in further work by the authors.

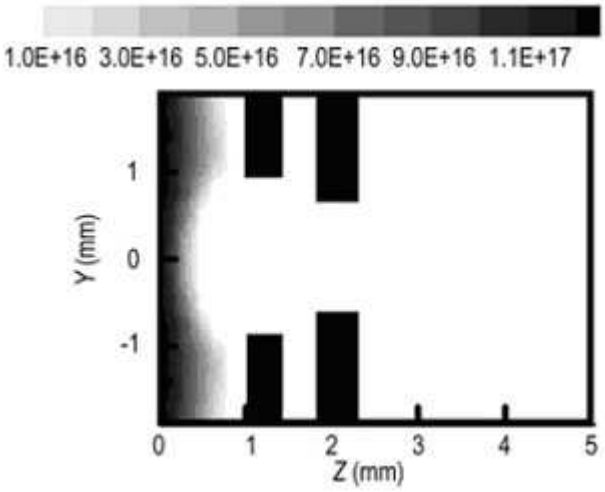

Figure 3.2: Electron density (Chang *et.al*, 2008)

A two dimensional axisymmetric PIC model was used by Zhong *et.al.* (2010a) to study the influence of accelerator grid voltage on the plasma sheath upstream of the screen grid and the ion extraction through typical ion optics. They state that grid erosion caused by direct impingement of beam ions and sputtering of CEX ions is one of the primary causes of failure. It is also stated that any direct impingement of beam ions on the grid is caused by poor focusing of the optics.

A single set of grid apertures was chosen as the simulation domain and the movement of ions was calculated under an electrostatic assumption. It is stated that the assumption of axisymmetry is only valid if the aperture radius is much less than the size of the hexagon around the aperture; however it is said to be '*approximately valid*' in this model if the ion beamlet is well focused. Only single-charged ions were considered in the simulation. A uniform mesh with 200x54 cells was used for the simulation domain and 40 test particles were injected into the domain at the upstream boundary in each time step, which was $1.5x10^{-5}$s. At the end of the simulation there were 70,000 test particles in the simulation domain, with each representing 10,000 ions. The ion distribution was studied and it was found that near the downstream surface of the accelerator grid the ion number in the beamlet boundary is higher than that in the central line, as can be seen in Fig. 3.3.
The authors state that this is caused mainly by the focusing effect of the optics. The potential distribution was also studied and compared with data collected from experiments. It was found that the potential distribution found in the simulation was different to the experimental results but the shapes were in good agreement, and the electrostatic field distribution upstream of the screen grid obtained by the simulation was said to be '*reasonable*'. Zhong *et.al.* (2010a) state that

> *'the simulation result is similar to the experimental data, which also indicated that our code can simulate the ion extraction through the ion optics'.*

The simulation showed a plasma sheath forming upstream of the screen grid; the potential

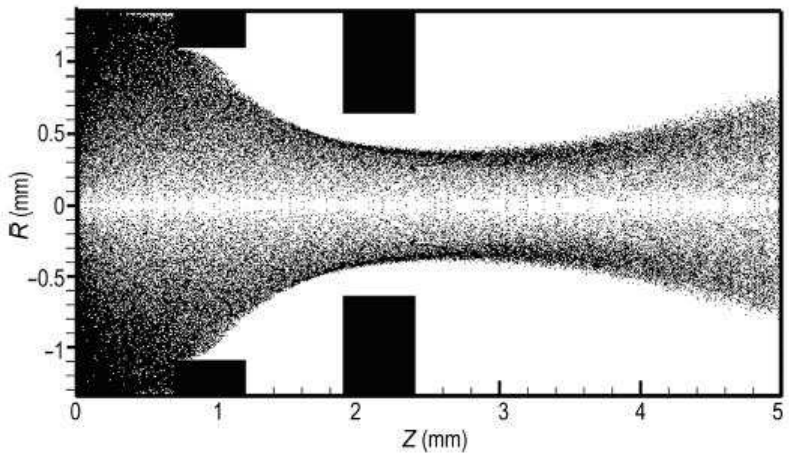

Figure 3.3: Ion distribution within a single screen grid and accelerator grid aperture. A low density of ions can be seen along the centre line of the apertures, while a higher number of ions can be seen near the downstream surface of the accelerator grid. (Zhong *et.al.*, 2010a)

of the screen grid is negative relative to the discharge chamber plasma, which causes ions approaching the sheath to be attracted towards the screen grid while electrons are repelled back into the plasma. This causes the electron density to drop rapidly in the sheath. The position of the sheath boundary was designated as the place where the ratio of electron density to ion density is equal to 0.1. Sheath position and shape are affected by many parameters; when the accelerator grid voltage is less negative, the sheath is positioned close to the screen grid with relatively small curvature and near the upstream surface of the screen grid the sheath was found to be convex to the screen grid aperture. This caused a large number of ions to directly impinge on the accelerator grid. When the accelerator grid became more negative the sheath moved gradually closer to the plasma and the sheath shape changed accordingly. The sheath near the upstream surface of the screen grid became convex to the side boundaries with a large curvature; this caused the beamlet to have a large divergence angle. The simulation showed that the saddle point potential increased with the increase of the accelerator voltages; as the accelerator grid voltage increases the possibility of electron backstreaming increases. If the saddle point potential is higher than the beam plasma potential it will cause a large number of electrons to pass back through the aperture, which could cause erosion within the discharge chamber. As a result of this, Zhong *et.al.* state that the accelerator grid voltage should be kept sufficiently negative to prevent backstreaming. Wang *et.al.* (1998) stated that

> *'electron backstreaming is undesirable because it reduces thruster efficiency; each electron which backstreams into the discharge chamber consumes as much power as a singly ionized propellant ion but does not produce thrust'.*

Sun *et.al.* (2010) simulated a three-grid electron cyclotron resonance (ECR) ion thruster, looking into the erosion of the ion optics and aiming to extend the previous work of Chen (2009). The electrons are regarded as a fluid and assumed to be collisionless and the ions

are regarded as particles and the neutral atoms are set as background. The collisions between ions and atoms are described by the Monte Carlo collision (MCC) method. The computational domain is a two-dimensional axisymmetric structure including a half aperture and a half grid. The three grids (screen, accelerator and decelerator) are electrically isolated from one another and the screen grid potential V_s is set slightly below the plasma potential to extract the ions and screen out the electrons. The accelerator grid (the middle grid) potential V_a is set to a negative potential to provide the accelerating field and the decelerator grid (downstream) potential V_d is usually set at 0V. The mesh sizes of the space satisfy the constraint of the Debye length λ_D, which in a warm plasma is

$$\triangle z, \triangle r < 3\lambda_D \tag{3.8}$$

(Birdsall and Langdon, 1985)

In this study the mesh size is chosen as $\Delta z = \Delta r = 5 \times 10^{-5}$m with a 176x36 uniform mesh adopted in the whole computational domain.
At each time step beamlet ions are injected into the simulation domain from the upstream boundary and the secondary ionized ions are neglected in the simulation due to their small number. The absorption boundary conditions are adopted in the upstream and downstream surfaces and also for the ions which collide with the surface of the grids. For the top and bottom boundaries the reflection boundary condition is used. Boundaries are often chosen to be reflecting when in reality particles would be passing into the next aperture domain and other particles would be flowing into the domain being studied; therefore particles can be reflected back into the simulation domain and considered to be particles flowing in from the neighbouring aperture domains. The velocities of the neutral atoms are around two orders of magnitude lower than those of ions because the neutral atoms are unaffected by the electric field; hence the neutral atoms are set as the background gas, which is unchanged in the code. Only the collisions between ions and the background gas, including elastic collisions and charge-exchange (CEX) collisions are considered.

Most of the results in this study were obtained in a steady state, meaning that the number of particles in the simulation domain remain constant. When looking at the electric potential it was found that CEX collision has little influence on the potential distribution, because of the small fraction of CEX ions compared to the fast moving beamlet ions. A sharp potential drop was found from the upstream of the screen grid to the downstream of the accelerator grid, causing a large axial electric field to accelerate the ions to a higher velocity. On the centre line there is a minimum potential point near the downstream edge of the accelerator grid called the 'saddle point', as can be seen in Fig.3.4. The potential at this point is important to limit electron backstreaming; numerically the saddle point potential was calculated as -12.7V to limit backstreaming. The conclusion was drawn that the design of the current optics satisfies the requirement to prevent electron backstreaming; in this study the saddle point potential was found to be 147.5V according to a model by Williams *et.al.* (2003) and it is stated that this result indicates that the simulation results are reasonable.

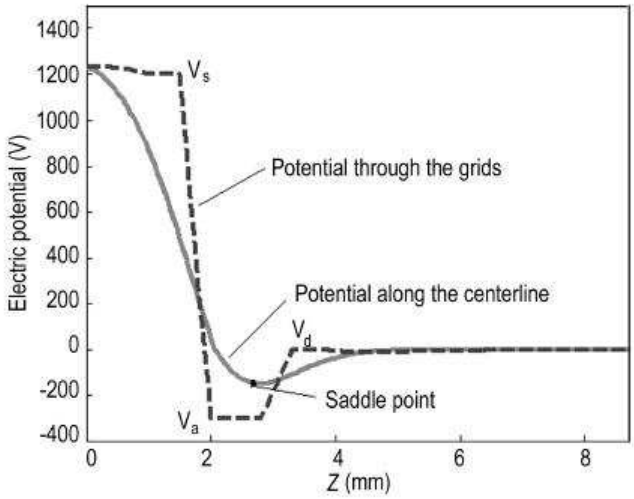

Figure 3.4: Electric potential along the central line and the line through the grids, with CEX collisions (Sun *et.al.*, 2010)

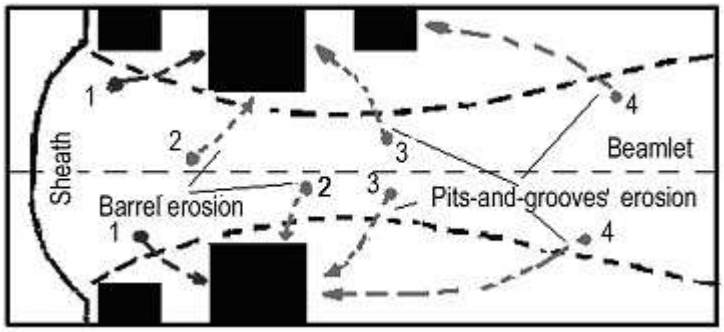

Figure 3.5: Schematic of CEX ion trajectories in three grid (top) and two grid (bottom) ion optics (Sun *et.al.*, 2010)

The ion number density was plotted and it was found the ion number density out of the beamlet region was more than two orders of magnitude lower than the value near the centre line. When CEX collision was neglected the beamlet ions could pass through the grid apertures successfully, without colliding with the grids. Sun *et.al.* stated that the effect of CEX ions colliding with the accelerator grid are significant; some parts of the CEX ions moved towards the upstream side of the accelerator grid while some parts collide with the accelerator grid aperture directly as 'barrel' erosion, while other parts move back from the downstream and cause 'pits and groves' erosion. Barrel erosion causes the enlargement of grid apertures. This was said to confirm the analysis of the accelerator grid erosion types illustrated in the paper. A comparison of the screen currents in the two grid and three grid cases was shown and it was stated that the decrease in the accelerator grid current in the three grid case was due to the decelerator grid preventing the 'pits and grooves' CEX ions from the downstream side. The beamlet velocities in the two cases were similar but the back flow velocity behind the accelerator grid in the three grid case is a little higher than in the two grid case, due to the stronger axial negative electric field in the

gap between the accelerator grid and decelerator grid. It is suggested that the differences in potential gradient in the two cases confirms this; the potential gradient behind the accelerator grid in the three grid case was steeper than that of the two grid case, due to the influence of the zero potential at the decelerator grid. It was also stated that in the three grid case the potential behind the decelerator grid sustains a potential of around 0, matching the central line potential shown in Fig.3.4, whereas in the two grid case there is a strong potential drop behind the accelerator grid. The smooth variation in potential behind the decelerator grid is said to effectively decrease the energies of ions flowing back from far downstream. Although these ions can still collide with the downstream edge of the decelerator grid it is suggested that the damage is so minimal that the erosion of the decelerator grid is almost negligible in the optics system. It is also stated that the decelerator grid can decrease the divergence angle of the beamlet flow and prevent the sputtering materials from moving into the plume region and causing damage to the spacecraft. This is suggested to be an advantage of the three grid system when compared to the two grid, however it has been suggested that the benefits of reducing erosion due to CEX ions provided by the decelerator grid are outweighed by the added complexity (Goebel and Katz, 2008). The ion trajectories in the two grid and three grid cases are shown in Fig.3.5.

Miyasaka *et.al.* (2010) developed a three dimensional particle-in-cell (PIC) code based on the flux-tube code developed by Nakano *et.al.* (2007). This code treats ion fluxes as flux-tubes and is stated to have a low calculation cost and high accuracy levels. In the code the time is integrated by the 4th order Runge-Kutta method and electric potential distributions are obtained from Poisson's equation using a finite element method (FEM). The finite element method is a method for finding an approximate solution for a simplified model. The simplified model is reduced to a form which is solvable by a finite number of numerical operations (Szabo and Babuska, 1991). The computational cost of the simulation is minimized by the use of parallelization and application of symmetry conditions. A rectangular, two grid geometry with 7 hole grids is employed, as was used by Hayakawa (2007), with grid sizes in the discharge and neutralizing regions determined from the respective Debye lengths. Ions, electrons and neutrals are all tracked as particles, and elastic and charge-exchange collisions are evaluated using a direct simulation Monte Carlo method (DSMC).

Collided ions were distinguished by the type of collision and it was found that elastically collided ions and multiple-collided ions (ions which have collided with neutrals more than once) were observed in almost all regions of the simulation domain. In Fig.3.6 the distribution of non-collided ions, collided ions and electrons within the simulation domain are shown.

It was found that charge-exchange ions were mainly generated in the beamlet region from the screen grid hole to the downstream area. The ratio of multiple-collided ions to total collided ions was found to be around 5%, which is stated to be significant. Erosion

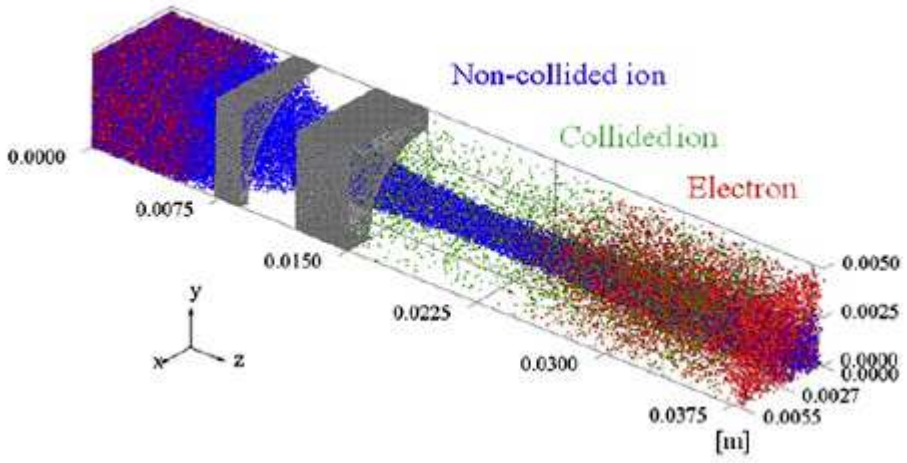

Figure 3.6: Three dimensional distribution of collided and non-collided ions and electrons (Miyasaka *et.al*, 2010)

distributions were calculated from a semi-empirical equation developed by Yamamura et.al. (1983). Current ratios of the accelerator grid current to the beamlet current were evaluated; for the upstream and inner surfaces a ratio of 1.3% was calculated, and a value of 2.7% was calculated for the downstream surface. These values were said to agree well with experimental values. Ions constituting the accelerator grid current to the inner surface were comprised of 93% charge-exchange ions and 7% multiple-collided ions, and on the downstream surface comprised of 92% charge-exchange ions and 8% multiple-collided ions. The ratios of multiple-collided ions on the inner and downstream surfaces were higher than the ratio existing in the entire region, suggesting that '*investigations of the behaviours of multiple-collided ions are important in evaluations of grid erosion*'. It was also found that charge-exchange ions that impact on the downstream surface and the inner surface of grid holes play a key role in the erosion of the accelerator grid, and that the tendencies of the collision energy of multiple-collided ions are different from those of the charge-exchange ions. The researchers also stated that

> *'the characteristics of the collided ions, including the collision distribution and energy, indicate that high-accuracy analyses of the motions of collided ions, including the multiple-collided ions, are important for quantitative evaluations of grid erosions'.*

Zhong *et.al.* (2010b) used a two dimensional PIC code to simulate half of one aperture pair within a two grid ion thruster. The top and bottom boundaries were designated as Neumann boundaries while the upstream boundary where particles were injected and the downstream boundary where particles left the simulation domain were designated as Dirichlet boundaries. Any ions impacting on the grids were deleted from the simulation. Zhong *et.al.* state that near the ion optics system the magnetic field is negligible compared with the electric field and can be ignored within the simulation. Electrons within the simulation were treated as a non-collisional isothermal (constant temperature) fluid,

and ions were injected at each timestep with axial velocity satisfying the Bohm criterion and radial velocity following a Maxwellian distribution. Updated velocities and trajectories of the ions were obtained using a leapfrog integration scheme with second-order accuracy in the time step. In the leapfrog integration scheme, the positions and velocities are 'leapfrogged' over one another, with one being advanced between full timesteps while the other is advanced by half timesteps.

The charge-exchange (CEX) collisions were calculated using an MCC method, and any CEX ions produced were then tracked by the PIC method along with the primary ions until impacting on the grids or exiting the simulation domain. The number of CEX ions in a cell is given by

$$N_{cex} = N_i n_n v_r \sigma_{cex} \Delta t \tag{3.9}$$

where N_i is the number of primary ions within the cell, Δt is the timestep, n_n is the number density of neutral atoms, v_r is the relative velocity of the collision pair and σ_{cex} is the CEX collision cross section, given by

$$\sigma_{cex} = (a - b \ln v_r)^2 x 10^{-20} \tag{3.10}$$

where the constants a and b are equal to -0.8821 and 15.1262 respectively. It was found that the CEX ions exert little influence on the electric potential distribution within the simulation, and it is suggested that this is due to the small number of CEX ions compared to the amount of primary ions. The primary ions were found to achieve maximum velocity near the centre of the accelerator grid hole, with a lower radial velocity than axial velocity. CEX ions were found to be present in almost all regions of the beamlet in varying amounts. CEX ions produced in the large radial site upstream of the screen grid were accelerated to impinge on the screen grid (see Fig.3.7, trajectory A), and were said to have velocities too low to cause obvious damage. However CEX ions produced in the small radial site upstream of the screen grid were generally accelerated past the accelerator grid aperture and are said to do no harm to the optics system but deteriorate the performance of the thruster (trajectory B).

Any CEX ions produced between the downstream surface of the screen grid and the upstream surface of the accelerator grid were accelerated out of the beamlet (see C and D marked trajectories, Fig.3.7). Some of these struck the upstream surface of the accelerator grid, causing sputtering due to high velocity, while others were accelerated onto the inner surface of the accelerator grid aperture, causing a gradual increase in diameter. CEX ions produced within the accelerator grid aperture also impacted on the inner surface of the aperture (see trajectory E) causing aperture enlargement which would eventually result in electron backstreaming. CEX ions produced downstream of the accelerator grid were mainly found to accelerate towards the downstream surface of the grid, causing the 'pits and grooves' erosion pattern as seen in Fig3.1. Any CEX ions formed just downstream

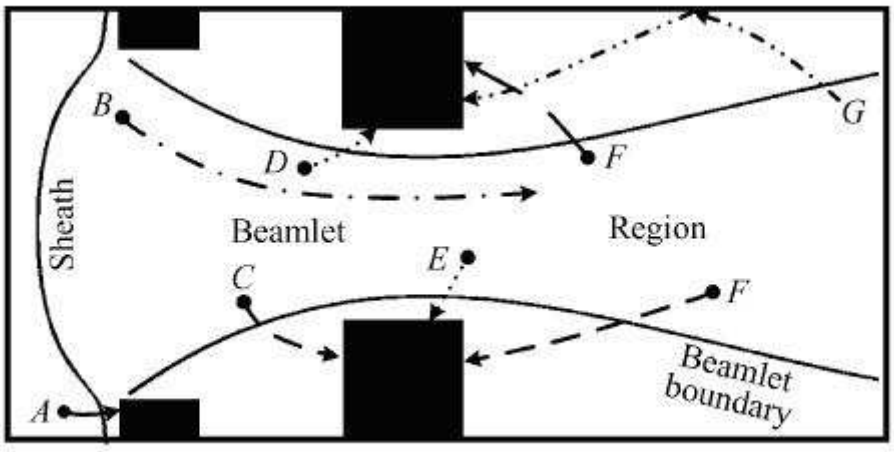

Figure 3.7: Behaviour of CEX ion trajectories (Zhong *et.al.*, 2010)

of the grids are stated to have relatively small velocities and therefore cause only slight erosion, while CEX ions formed further downstream impact with a higher velocity due to the large potential difference experienced, causing the majority of the erosion (trajectory F).

The conclusion reached by the researchers is that any damage caused to the screen grid caused by CEX ions is minimal due to the slow impact velocities, while erosion of the accelerator grid is more serious, especially on the downstream side of the grid.

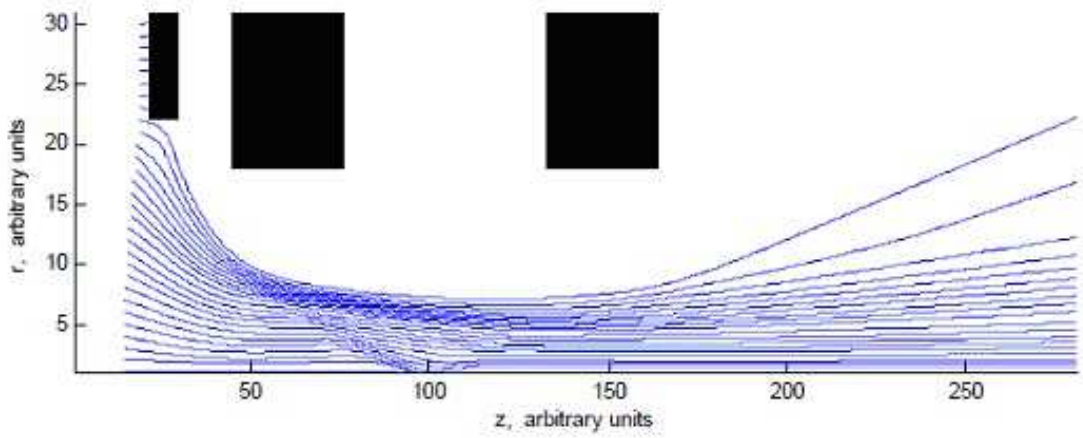

Figure 3.10: Particle streamlines, specific impulse 10,000s (Coletti *et.al.*, 2010)

Coletti *et.al.* (2010) used a 3 dimensional ffx simulation code in order to study dual stage ion thrusters. The ffx code analyses a 3 dimensional rectangular region, using a uniformly spaced Cartesian mesh with each direction having a different mesh spacing, following the flow chart shown in Fig. 3.8 (Farnell *et.al.*, 2003). They discovered that the fourth grid

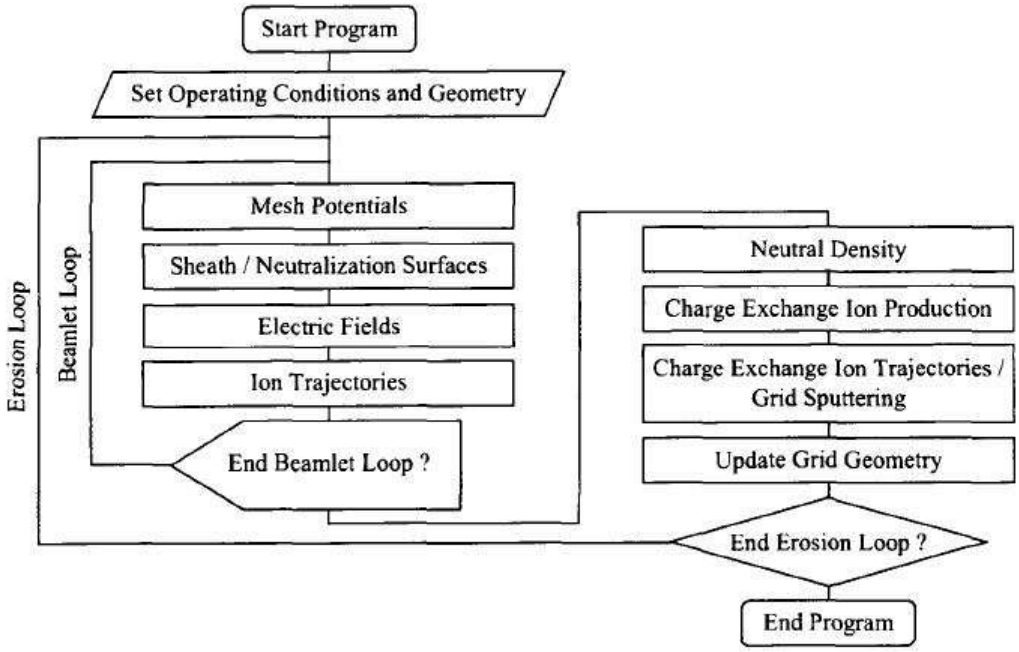

Figure 3.8: Flowchart of the ffx simulation code (Farnell *et.al.*, 2003)

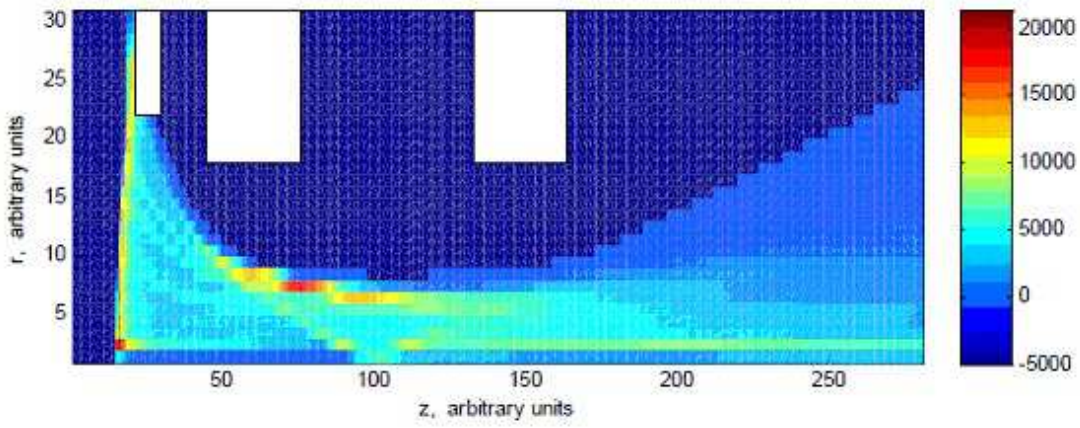

Figure 3.9: Beam ion density, specific impulse 10,000s (Coletti *et.al.*, 2010)

in the Dual-Stage 4-Grid thruster (discussed further in Section 4) was not necessary (as suggested by Goebel and Katz, 2008) and provided thruster specifications in order to produce specific impulses of 10,000s and 6,100s. The beam ion densities and ion streamlines for the 10,000s case are shown in Fig.3.9 and Fig.3.10.

This work was then extended by Coletti and Gabriel (2010), using a grid geometry shown in Table 3.3. It was found that using the specified geometry no direct ion impingement occurred and CEX ion impingement was found to be lower in the DS3G than in the reference gridded ion engine (GIE).
Grid power loading and erosion rates were also found to be lower in the DS3G, and erosion

	Aperture radius	Grid thickness	Voltage
Grid 1	1mm	-	8120V
Grid 2	0.7mm	4x Grid 1	6120V
Grid 3	0.7 - 1mm	4x Grid 1	-120V
Grid spacing	Centre	Edge	
1st - 2nd	0.5mm	1mm	
2nd - 3rd	1.5mm	1.5mm	

Table 3.3: Table showing grid parameters chosen by Coletti and Gabriel (2010)

of the second grid in the DS3G was found to occur very fast for the first 5000 hours of operation and then become very slow. The third grid was found to display almost no change in aperture radius with a marked decrease in thickness over time; this is said to be due to most of the impaction on the third grid coming from CEX ions produced downstream of the grid and therefore impacting on the downstream side of the grid, resulting in thickness reduction and pits and grooves erosion. Grooves with a depth of around 0.1mm and pits of around 0.25mm in depth were discovered; these values are close to those measured on the NSTAR ion optics. The predicted lifetime for the DS3G was said to be around 45,000 hours, compared with the lifetime of the reference GIE of 37,000 hours. The researchers conclude that the DS3G provides improved performance when compared to the reference GIE without any reduction in lifetime expectations, and suggest that the next step is to build a prototype of the DS3G in order to confirm the results achieved through simulation.

This chapter has provided an overview of research performed in the area of performing simulations of ion thrusters. As the dual stage ion thruster concept is fairly new there is less research available than for other ion thruster designs, providing an area of research where significant contributions may be made. It has been suggested that the dual stage design should not include the fourth grid from the original concept; this work will aim to build upon this idea, comparing the two designs and looking at the issue from a different perspective to the research discussed above. Gaining multiple views on an issue is important in order to reach an appropriate conclusion, therefore this work will stand alongside the research on dual stage thrusters already in existence, providing an alternative simulation tool which will look at different aspects of the research question.

4 Dual Stage Ion Thrusters

4.1 The Dual-Stage 4-Grid Ion Thruster

This section will provide an introduction to the concept of the dual stage ion thruster, a recent concept that takes the idea behind the conventional gridded ion engine and manipulates the original design in order to produce a more effective ion thruster. The dual stage ion thruster has been chosen as the focus of this work as it further develops the concept of the gridded ion engine, providing substantial improvements in performance over the traditional gridded ion engine. This means that missions requiring a high specific impulse not achievable using traditional gridded ion engines can now be attempted with the dual stage design.

The Dual-Stage 4-Grid ion engine (known as the DS4G) was developed at ANU (the Australian National University) for ESA (the European Space Agency) and was successfully tested in 2005 in a space simulation chamber (ANU, 2010). The concept was proposed by D. Fearn, with inspiration being taken from Controlled Thermonuclear Reactor (CTR) experiments, in which ion sources are used to inject highly energised neutral particles into fusion reactor experiments (Bramanti and Walker, 2006). Two stage ion sources are used in these fusion experiments as it was found that with a single stage ion source a decrease of beam power flux density was unavoidable with the increase of acceleration energies above a certain threshold due to electric breakdown problems (Ohara, 1978).

The gridded ion thrusters discussed in Section 1 use two or three grids to accelerate the ions, whereas the DS4G employs 4 accelerating grids. This additional fourth grid, when used in an optimised configuration, could theoretically make the DS4G thruster up to 10 times more efficient than current state-of-the-art ion thrusters. Schematic diagrams of the four grid system can be seen in Fig. 4.1. In a gridded thruster with a two or three grid configuration the ions are extracted and accelerated in one stage, and due to physical constraints (desire to avoid high-voltage breakdown) the extraction potential between the first and second grids is limited to 5kV, which limits the maximum thrust density the engine can produce. The DS4G enables the extraction and acceleration to be separated into two separate stages, allowing very high accelerating potentials (up to 30kV) to be applied to the second stage without any adverse effects to the extraction stage (ANU, 2010). This high acceleration potential allows a high velocity to be reached while using light gases such as hydrogen as fuel (Bramanti and Walker, 2006).

It is suggested that a single 20cm diameter DS4G thruster could operate at 250kW power to produce a 2.5N thrust and a specific impulse of 19,300s using Xenon propellant operating at a 30kV beam potential (Bramanti and Walker, 2006). The very high ion beam potentials on the grids that would be possible with the 4-grid design would significantly increase the exhaust velocity, specific impulse, power density and thrust density compared with 3-grid thrusters. However this high performance *'comes at the expense of a high*

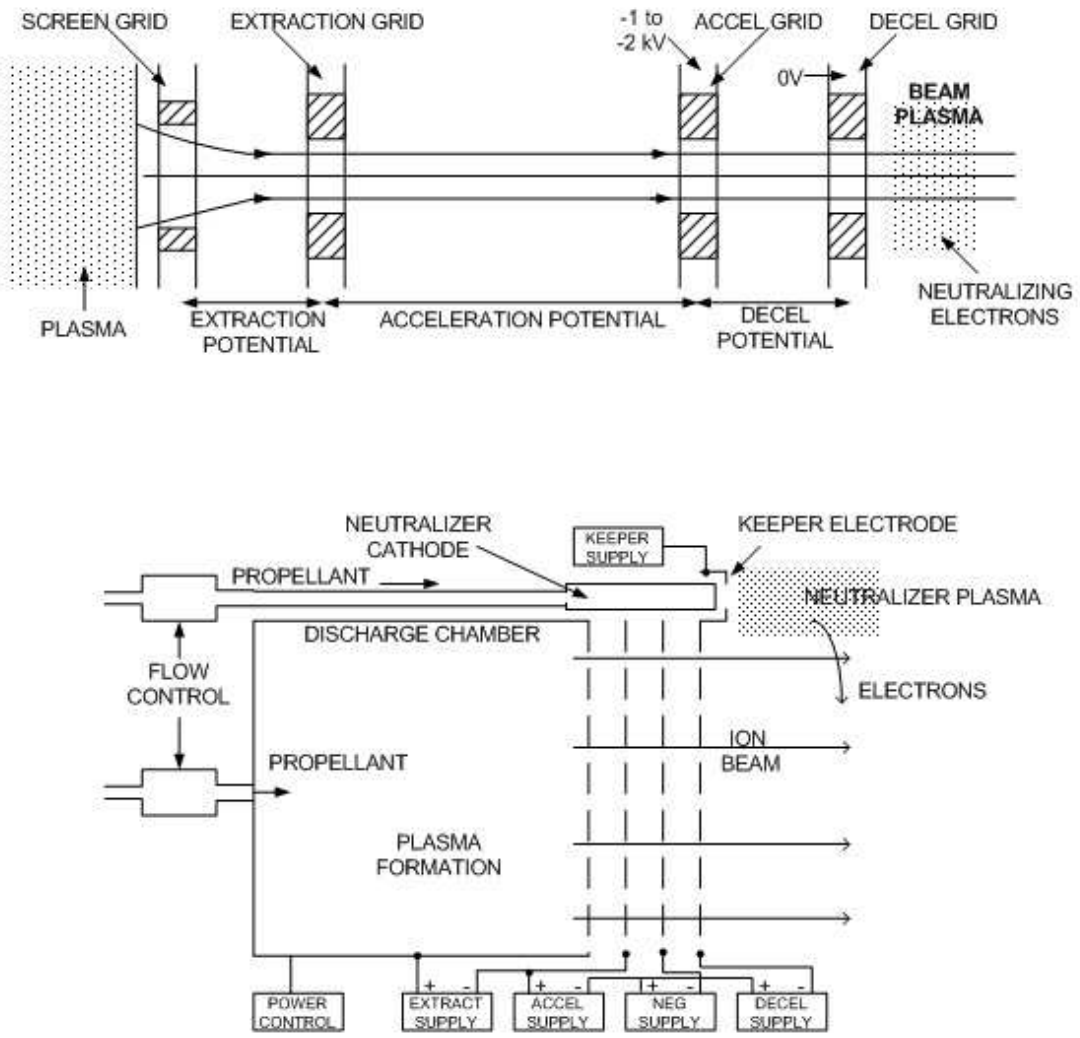

Figure 4.1: Schematics of the four accelerating grids (top) and the full discharge chamber (bottom) (Bramanti and Walker, 2006)

power-to-thrust ratio' (approx. 110 W/mN), therefore the DS4G would likely only be compatible with lightweight power systems (Bramanti *et.al.*, 2009). The addition of the fourth grid also greatly increases the complexity of the thruster. In the DS4G the screen grid has the same function as in a conventional GIE and the second grid is the extraction grid, the function of which is to provide a potential difference in order to extract the ion current. The extraction grid does not aim to accelerate ions to high velocities. The third grid in the system is the acceleration grid, where a very high potential difference can be applied with relation to the extraction grid, enabling high specific impulse to be obtained while maintaining a constant ion beam current density, making an increase in thrust density possible (Coletti and Gabriel, 2010).

The screen grid would be at a high positive potential, providing the initial acceleration for the ions. The extraction grid would be at a high positive potential slightly lower than that of the screen grid, with V_{12} giving the extraction potential.

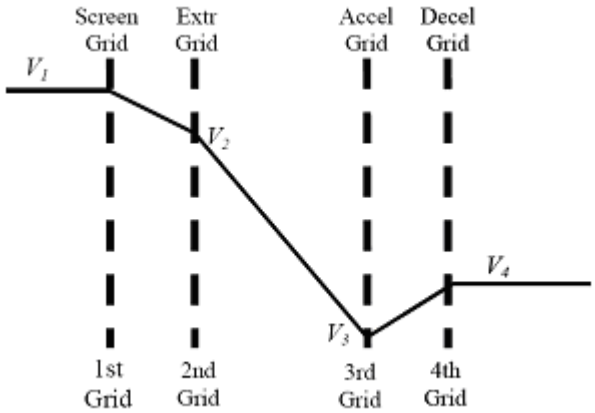

Figure 4.2: Voltage profile of the grids in the DS4G (Coletti *et.al.*, 2010)

$$V_{12} = V_1 - V_2 \tag{4.1}$$

The acceleration grid would be at a slightly negative potential, providing a large potential difference for acceleration as can be seen in Fig. 4.2 and reducing or preventing electron backstreaming; the deceleration grid would be at a zero voltage (Coletti and Gabriel, 2010). Research by Coletti *et.al.* (2010) suggests that the DS4G system theoretically only provides advantages over a conventional GIE in terms of thrust density if the voltage difference applied in the second stage is 0.6 times that of the first stage or greater; however this does not take into account ion impingement and related problems. The acceleration to extraction voltage ratio is given by

$$\Gamma = \frac{V_2 - V_3}{V_1 - V_2} \tag{4.2}$$

The research states that due to the added complexity of the fourth grid, the DS4G would be a viable option for values of Γ greater than 1, as operation at low values of Γ result in a decrease in the extraction current (Coletti *et.al.*, 2010). This means that the DS4G thruster may only be suitable for missions where the required thruster performance would call for a configuration with a high voltage difference in the second stage. This constraint would not apply to the DS3G thruster discussed in Section 4.3 due to the removal of the fourth grid, meaning that the three grid version of the thruster may be applicable to a wider range of potential missions.

During testing in 2005 the prototype thruster produced an exhaust plume with total acceleration potentials as high as 30kV and a velocity of 210km/s, four times faster than other competing thrusters (ANU, 2010). The prototype thruster was operated in the 1-2kW power range with a thruster diameter of 5cm, though due to high power density it is scalable to power levels of almost 1MW with a 50cm beam diameter (Walker *et.al.*, 2006).

4.2 Testing

4.2.1 The DS4G Prototype

The original aim of the prototype testing was to produce and test a Single Aperture Four Electrode (SAFE) configuration with an aperture diameter of 1mm. However it was decided that in order to fully demonstrate the DS4G concept a system consisting of four electrodes, each containing 43 apertures of a 1mm diameter, would be produced and tested (Bramanti and Walker, 2006).

The prototype DS4G thruster was based on a 5cm diameter cylindrical ceramic discharge chamber and was fuelled with Xenon gas. The RF discharge was energised by a 3-turn antenna coiled around the discharge chamber, biased to the screen grid voltage and was fed from an RF system operating at 13.56MHz. The high voltage 4 grid system was then attached to the discharge chamber. However this set up is not applicable for use in space and was intended to demonstrate the principle of the thruster and identify any critical issues for the future (*ibid*).

The prototype consisted of three major subsystems; the mechanical subsystem including the clamping mechanism, the Radio-Frequency (RF) subsystem comprising of the gas injector, ceramic plasma source tube, 3-turn antenna, stand of transformer, impedance matching box and RF generator, and the high voltage (HV) subsystem comprising of the grid module, two HV power supplies and one LV power supply.

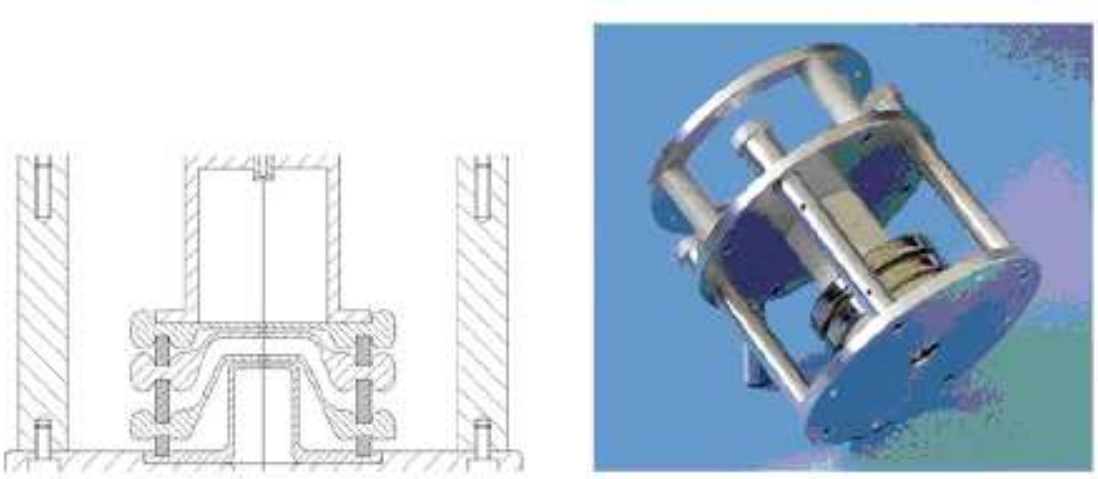

Figure 4.3: Schematic and photograph of the DS4G prototype (Bramanti and Walker, 2006)

The test campaign for the DS4G took place in two phases, conducted by the Advanced Concepts Team from ESA with support from the Electric Propulsion Section and ANU. The testing took place in the CORONA vacuum facility at ESTEC during November 2005 and May 2006. The RF CORONA test facility (CTF) enables both pressure and temperature to be controlled in order to simulate real life scenarios. The aim of the test campaign was firstly to demonstrate the feasibility of the four grid thruster concept,

secondly to verify the improvements in performance when compared to traditional GIEs, and thirdly to investigate critical design issues and technological challenges (Bramanti and Walker, 2006).

4.2.2 Test Results

The first stage of testing began with thermal and high voltage breakdown tests. The thruster was found to be able to operate with RF plasma discharge at power levels of up to 600W for over 45 minutes, providing the researchers with high levels of confidence in the RF subsystem operation. Voltages on the first two grids reached 30kV and 27kV respectively in the vacuum conditions during the breakdown tests, providing confidence in the HV subsystem.

The SAFE configuration was used to demonstrate reliable extraction of high voltage beams without ion impingement, then testing began on the 43 aperture prototype (Bramanti and Walker, 2006). The first stage of testing of the 43 aperture DS4G prototype was considered a success and the thruster produced excellent results in terms of thrust, SI, beam density and beam divergence. Negligible (around 1%) direct ion impingement on the grids was recorded, and propellant utilization efficiency was high at around 70%. However as this stage of testing was only intended to demonstrate the principle of the thruster the grid ion optics were not optimised and efficiency was low (*ibid*).

In the second stage of testing in 2006 the aim was to improve the efficiency, using a revised grid design with an increased open area ratio of 61%. Higher electrical efficiency, total efficiency, total thrust and power densities were achieved. Mass utilization was improved from 70% to 80%-96% by specific targeting of the beam current in relation to mass flow rate, compared to 85%-92% achieved by conventional ion thrusters.

	Typical test case	Best value	Operating parameters	
Thrust (mN)	2.7	5.4	Beam potential (kV)	10 - 17.5
Beam potential (kV)	15	17.5	Extraction potential (kV)	1.5 - 5
Specific impulse (s)	14000	14500	First electrode (beam) current mA	4 - 33
Mass utilization efficiency	0.96	0.96	RF power (W)	20 - 316
Electrical efficiency	0.66	0.75	Beam power (W)	80 - 398
Total efficiency	0.63	0.7	Total efficiency	0.4 - 0.7
Beam divergence (deg)	4.6 - 5.3	3.8	Electrical efficiency	0.5 - 0.75
Total power (W)	300	614	Beam divergence	3.8 - 6.2
RF power (W)	101	316	Mass flow rate (mg/s)	0.01 - 0.05
Thrust density (total) (mN/cm^2)	0.86	1.7	Beam diameter (cm)	2
Total beam power density (W/cm^2)	64	126	Grid open area ratio	61%

Table 4.1: DS4G laboratory prototype operational parameters and performance results during the second stage of testing in May 2006 (Bramanti and Walker, 2006)

The table above shows the performance statistics of the DS4G during the second stage of testing. However these values are pessimistic as they assume that all currents collected

by the extraction and accelerator grids are due to direct ion impingement and so the grid currents have been subtracted from the beam current and this reduced beam current has been utilized in calculating the above performance parameters. It is not possible to assess actual impingement currents with available data. When the extraction and acceleration grid currents were ignored the performance statistics increase to typically 3.7mN at the nominal 2.7mN thrust level and to 6.75mN at 5.4mN (Bramanti and Walker, 2006). These results have been taken from the executive summary of the testing, which concludes that

'*future benefits justify the research and development effort made*'

(Bramanti and Walker, 2006).

4.3 The Dual-Stage 3-Grid Ion Thruster

4.3.1 Justification for Removal of the Deceleration Grid

A modified design of the DS4G, known as the Dual-Stage 3-Grid (DS3G) ion thruster, has been suggested by Coletti *et.al.* (2010). This research suggests the removal of the deceleration grid which is used in the DS4G at a zero voltage, with its sole function being to limit the downstream erosion by charge-exchange (CEX) ions and prevention of pits-and-grooves erosion. In conventional GIEs this function is provided in some systems by the third grid; Goebel and Katz state in their book 'Fundamentals of Electric Propulsion: Ion and Hall Thrusters' (2008) that although the three grid systems have a potentially longer life than the two grid systems due to this reduction in erosion and generate less sputtered material into the plume that can be deposited on the spacecraft, these benefits are offset by the increased complexity of including the third grid in the system. Coletti *et.al.* (2010) suggest that this same principle be applied to the DS4G thruster, resulting in a dual stage, three gridded system and greatly reducing the complexity of the thruster.

The third grid in the DS3G changes the erosion pattern normally found within traditional GIEs; CEX ions produced between the first two grids impact on the extraction grid instead of the accelerator grid, causing aperture enlargement. It is suggested that widening of the extraction grid aperture has less severe consequences than widening of the accelerator grid aperture (Coletti and Gabriel, 2012). Any CEX ions produced between the second and third grids are accelerated downstream due to the large potential difference in the area, causing no damage to the ion optics (Coletti and Gabriel, 2012).

Lifetime analysis carried out by Coletti and Gabriel (2010) suggests that the third grid results in a longer lifetime compared with traditional GIEs. As erosion occurs within the ion optics and the apertures widen the minimum centerline potential increases; once this value exceeds a certain threshold electrons start backstreaming into the thruster, causing high power losses and defocusing the beam, resulting in failure of the thruster. It was found that the minimum centerline potential was consistently higher for a typical GIE than for the DS3G, resulting in a longer operating lifetime for the DS3G (*ibid*). The authors extrapolated their data to predict lifetime of the thrusters, finding a value of

about 25,000 hours for the typical GIE and about 50,000 hours for the DS3G, showing a significantly longer potential lifetime for the DS3G.

4.3.2 Suggested Operational Parameters

Coletti and Gabriel (2010) presented a design for the ion optics of the DS3G. They suggest that for optimum performance the apertures on the screen grid should be around 1mm in diameter, while the extraction grid and acceleration grid aperture diameters should be around 30% smaller. The apertures on the acceleration grid should be the same as the extraction grid apertures at the centre and the same as the screen grid at the edge.The extraction grid and acceleration grid thicknesses should be four times that of the screen grid. The gap between the first and second grids was chosen to be 0.5mm at the centre of the grids and increasing to 1mm at the edges of the grids while the gap between the second and third grids should be constant, with the best value found to be 1.5mm. This value was selected in order to maximise the focusing of the ion beam while avoiding ion impingement and arcing between the grids (Coletti and Gabriel, 2010). The suggested voltages for the grids are 8120V for the screen grid, 6120V for the extraction grid and -250V for the acceleration grid. The main parameters are summarised in the table below.

	Thickness	Aperture diameter (mm)	Voltage (V)
Screen grid	-	1	8120
Extraction grid	4x screen grid	0.7	6120
Acceleration grid	4x screen grid	0.7 - 1	-250

Table 4.2: Table showing a summary of the suggested operational parameters for the grids on the DS3G

4.4 Engineering Issues Relevant for Study by Simulation

4.4.1 Erosion and Sputtering

As a result of the high plasma temperature and density in the discharge chamber, internal erosion of the discharge chamber materials may become apparent over long operation. Bramanti *et.al.* (2009) suggest that application of sputter-resistant coatings (ie graphite or tantalum) would alleviate this problem, as would constructing the discharge chamber from graphite. Grid erosion due to sputtering is of high concern; high acceleration between extraction and acceleration grids ensure a low beam divergence and by limiting extraction potential (to below 5kV) and beam current density it can be ensured that extracted beamlets are well within their grid holes (Coletti and Gabriel, 2010). However despite this some ion impingement will occur (including charge-exchange ions) and it has been suggested that manufacturing grids from low sputter rate materials (such as graphite) would be prudent to minimize the effects of sputtering. Coletti and Gabriel (2010) suggest that in the DS3G ion thruster system, erosion is due to CEX ions as when the chosen gap of 1.5mm between the extraction grid and acceleration grid is used, no direct ion impingement occurs.

It is known that accelerator grid erosion is caused mainly by the formation of charge-exchange (CEX) ions, which are created by charge-exchange collisions between fast beam ions and neutral propellant atoms. This theory was first presented by Kerslake in 1963. Since the ion source is never perfect it will always have some neutral efflux out of the thruster; charge-exchange collisions are inevitable (Peng *et.al.*, 1993). Accelerator grid lifetime can be defined either by the point where electron backstreaming can no longer be prevented by the power supply due to aperture enlargement, or by structural failure due to 'pits-and-grooves' material loss. Fig. 4.4 shows where within the thruster the CEX ions are produced which cause the two types of erosion. The former mechanism is believed to dominate grid erosion in space, where neutrals for CEX collisions come only from the thruster, not the source gas within a vacuum facility (Chang *et.al.*, 2008).

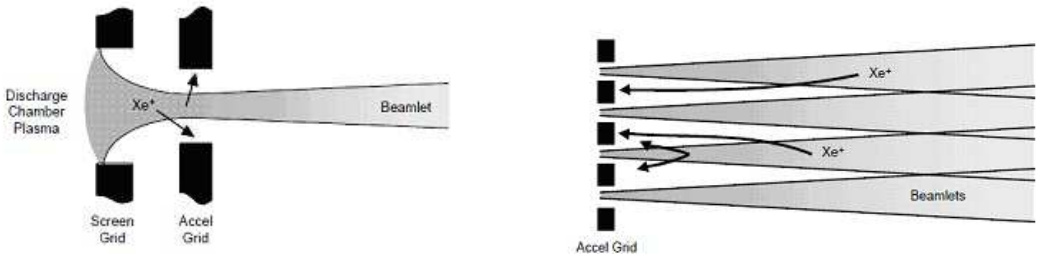

Figure 4.4: Figures showing where CEX ions are produced, causing the two types of erosion. Left: barrel erosion causing aperture enlargement. Right: pits and grooves erosion

Experiments have shown that the maximum erosion occurs at the geometric centre between apertures for a hexagonal geometry two-grid system. As the velocities of CEX ions are negligible when created the charge-exchange erosion pattern is determined by the electric field in the deceleration region. There is a potential gradient in the transverse direction due to the positive space charge inside the ion beam, which tends to force CEX ions out of the primary beam and into this geometric centre between apertures. This is where the lowest potential occurs and therefore where maximum sputtering erosion occurs (Peng *et.al.*, 1993). The charge-exchange collision rate is energy and time dependant. Accelerator grid erosion also occurs via ion bombardment (Chang *et.al.*, 2008).

As stated above, it has been found that the extra grid in the DS3G results in altered erosion patterns when compared to a traditional GIE. CEX ions produced between the first two grids result in increased aperture size (known as 'barrel erosion') on the extraction grid as opposed to on the acceleration grid in a traditional GIE. Any CEX ions produced between the second and third grid are accelerated out of the thruster due to the high potential gradient in the area, causing no damage to the ion optics (Coletti and Gabriel, 2012).

4.4.2 Maximization of Key Performance Parameters

Key performance parameters for ion thrusters include the thrust, specific impulse, change in momentum, power efficiency and rate of erosion. In this work the layout of the ion optics along with the voltages applied to them for both the DS3G and DS4G will be studied and manipulated in order to attempt to find the most efficient configuration in terms of the parameters stated above.

This chapter has provided an introduction to the concept of dual stage ion thrusters, which this work will now focus on. The following chapter will discuss some current simulation techniques and will then introduce the simulation code that has been written for this work, including the steps the simulation code takes and the method used to verify the simulation in order to ensure that the simulation code is producing accurate results.

5 Simulation Development

This chapter will focus on the simulation code. It will begin with a short introduction to the different simulation methods available and will then discuss the simulation code that has been written for this work. The sections below will include a discussion on the main equations used within the simulation code, the method used to choose the original input parameters and a discussion on verification of the simulation performance and results.

5.1 Simulation Techniques

5.1.1 Particle In Cell

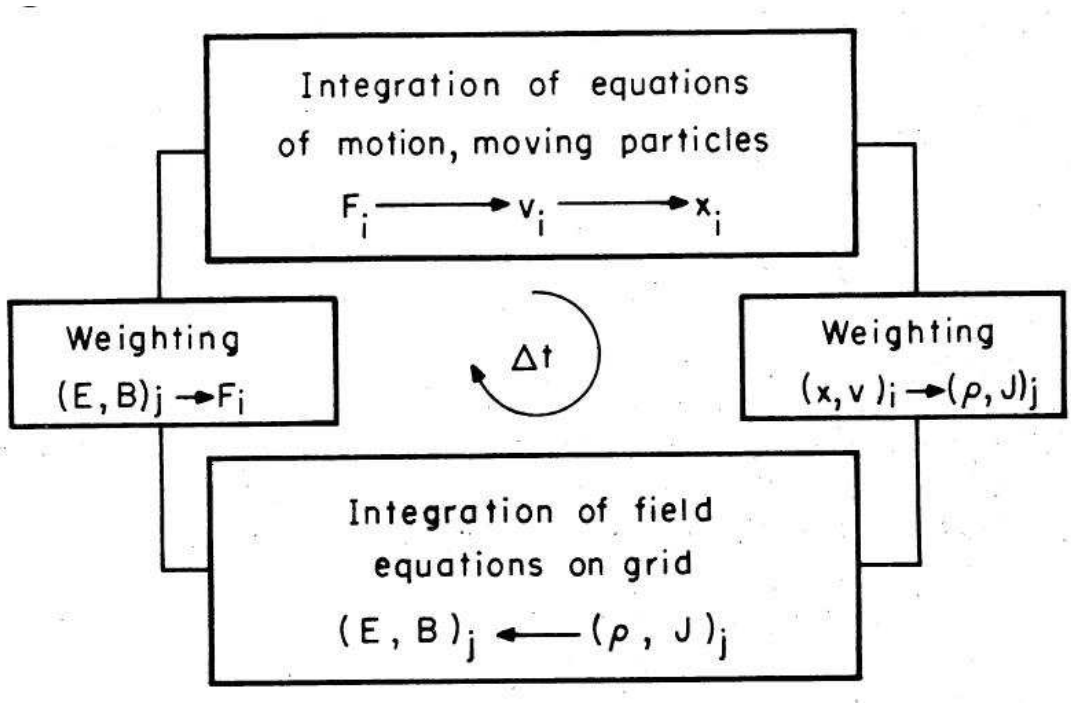

Figure 5.1: Flowchart showing the PIC process (Birdsall and Langdon, 1985)

When simulating the motion of particles it would be far too time consuming to calculate the forces acting on each particle individually. In particle in cell (PIC) simulations a mathematical grid is imposed on the simulation domain; the charge density is calculated at the grid points by interpolating charge from the particle positions, the potential and the electric field values are calculated from the charge density, the fields can then be interpolated back to the particle positions and the new particle positions can be calculated (Smith, 2006). This process is shown in the flowchart in Fig.5.1. A single simulation particle represents a large number of real particles, and is known as a 'super particle'.

In the simulation code the particle parameters are first inputted in real values and conversion factors are then applied to calculate the charge of the super particle. Conversion factors are used to change many of the input parameters relating to the simulation into

computer units in order to streamline the program and reduce complexity.

The particle-in-cell method has been chosen to produce a simulation code for this work and will be discussed in more detail later in this section.

5.1.2 MHD

The simplest method of modelling the behaviour of a plasma while including most of the macroscopic properties of a plasma in fluid model is the magnetohydrodynamics (MHD) method, consisting of a single composite fluid (hydrodynamic) model with Lorentz force effects for the plasma along with Maxwell's equations for the electromagnetic fields (Callen, 2006). In MHD simulations the plasmas are highly polarizable, quasi-neutral fluids, and the electric fields are calculated self-consistently from Ohm's law, Ampere's law and the charge continuity equation, therefore use of Gauss' law is not required. A wide range of phenomenon can be described by the MHD equations in small gyroradius, magnetised plasmas. The MHD method is stated to be '*the fundamental, lowest order model used in analysing magnetised plasmas*' (Callen, 2006)

5.1.3 Hybrid

In a hybrid simulation code one or more of the plasma species are treated as a fluid while the rest are treated as particles. For example in several codes simulating the behaviour of ion thruster optics the ions are treated as particles using standard particle-in-cell techniques while the electrons are treated as a fluid.

5.2 PIC Techniques

5.2.1 Particle Position Weighting Schemes

The calculations used to interpolate the particle positions to the grids and then the fields back to the particles are called weighting, and the chosen order of the weighting scheme determines the shape of the simulation superparticles. The same weighting scheme should be used to firstly weight the particles to the grids and then to interpolate the force on the particles from the electric field in order to eliminate self-force, ensure conservation of momentum and prevent numerical instabilities arising in the code (Birdsall and Langdon, 1985).

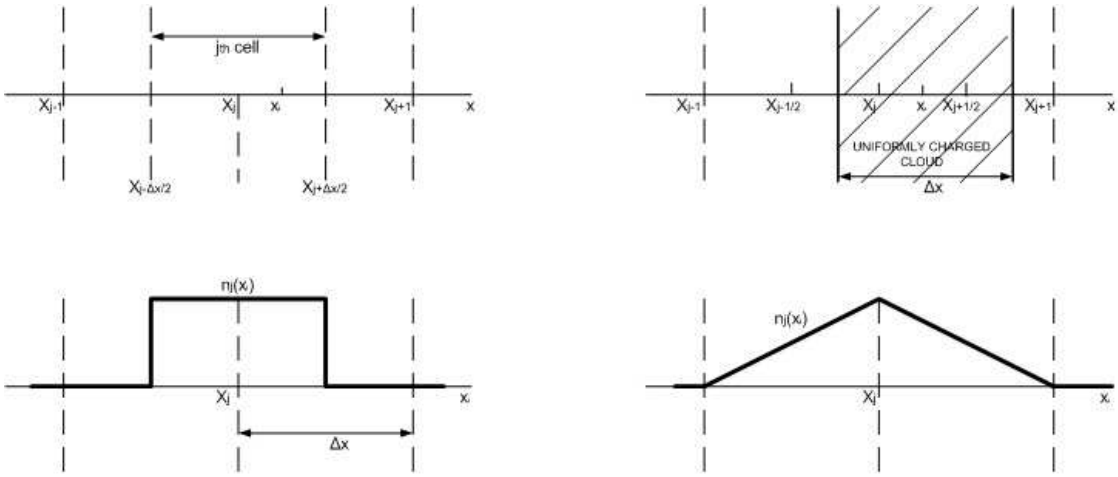

Figure 5.2: Diagram of zero order (left) and first order (right) weighting schemes in one dimension (Birdsall and Langdon, 1985)

Zero order weighting, known as nearest grid point (NGP), counts the number of particles within one grid's width of a grid point j and assigns the number to that point. This leads to the particle having a rectangular shape of width Δx. The advantage of this weighting method is that it is not computationally intensive, as only one grid point look up needs to be done per field calculation. Diagrams of the weighting schemes and resulting particle shapes for zero and first order weighting in one dimension are shown in Fig. 5.2. However particles entering or exiting grid cells lead to sharp fluctuations in the fields, so to reduce the noise in the fields a higher order weighting scheme is required.

First order weighting, during which the charge of the particle is linearly weighted to the four nearest grid points (in two dimensions), produces fields with less noise than NGP weighting but is more computationally intensive, requiring three more grid look-ups in each time step. This method is also known as cloud-in-cell (CIC) as the particles appear as finite sized rigid clouds, particle-in-cell (PIC) or bilinear weighting. The weights for bilinear weighting scheme are given by

$$\rho_{j,k} = \rho_c \frac{(\Delta x - x)(\Delta y - y)}{\Delta x \Delta y} \tag{5.1a}$$

$$\rho_{j+1,k} = \rho_c \frac{x(\Delta y - y)}{\Delta x \Delta y} \tag{5.1b}$$

$$\rho_{j+1,k+1} = \rho_c \frac{xy}{\Delta x \Delta y} \tag{5.1c}$$

$$\rho_{j,k+1} = \rho_c \frac{(\Delta x - x)y}{\Delta x \Delta y} \tag{5.1d}$$

where ρ_c is the charge of the superparticle.
Second and higher order weighting schemes use quadratic or cubic splines in order to round off the roughness in particle shape and further reduce noise in the charge density

and fields. Second order weighting (quadratic spline or QS) distributes the charge of each particle between nine grid points, resulting in an almost circular particle shape.Higher order weighting schemes require additional computing power and therefore the computational intensity should be balanced against acceptable levels of noise appearing in the fields. In this simulation code the first order weighting scheme was chosen.

5.2.2 Field Calculations

At the beginning of each simulation run the static potential distribution and hence the electric fields are calculated using Matlab's built in PDEtool. These fields are produced by the voltages applied to the grids and other areas of the discharge chamber. Poisson's equation is solved on a triangular mesh using Dirichlet boundary conditions on the boundaries of the simulation domain and the resulting field results are imported into the simulation code, and the grid is converted from triangular to rectangular. The computational mesh is shown in Fig. 5.3 and the potential distribution within the simulation domain calculated using the PDEtool within Matlab, along with arrows showing the strength and direction of the electric field, is shown in Fig. 5.4. Dirichlet boundary conditions specify the value of the solution at the boundary, whereas Neumann boundary conditions specify the value of the derivative of the solution at the boundary (LeVeque, 2007).

$$TriangleQuality = \frac{4a\sqrt{3}}{h_1^2 + h_2^2 + h_3^2} \tag{5.2}$$

The accuracy of the calculation results depends on the sizes and shapes of the computational mesh applied to the domain. The quality of the mesh is particularly important along the boundary of the simulation domain, as it should be fine enough to resolve the boundary layer equations in detail. A poor quality computational mesh can slow the calculation speed and introduce large round-off error into the results (Shewchuk, 2002). The computational mesh shown in Fig. 5.3 is colour coded according to the quality of the triangles within the mesh. The quality of each triangle is calculated using Eq.5.2, where a is the area of the triangle and h_1,h_2 and h_3 are the side lengths of the triangle. If the triangle quality is greater than 0.6 it is said to be of an acceptable quality. It can be seen in Fig. 5.3 that all the mesh triangles have a quality of 0.7 or higher therefore the calculation should produce results that have an acceptable degree of accuracy.

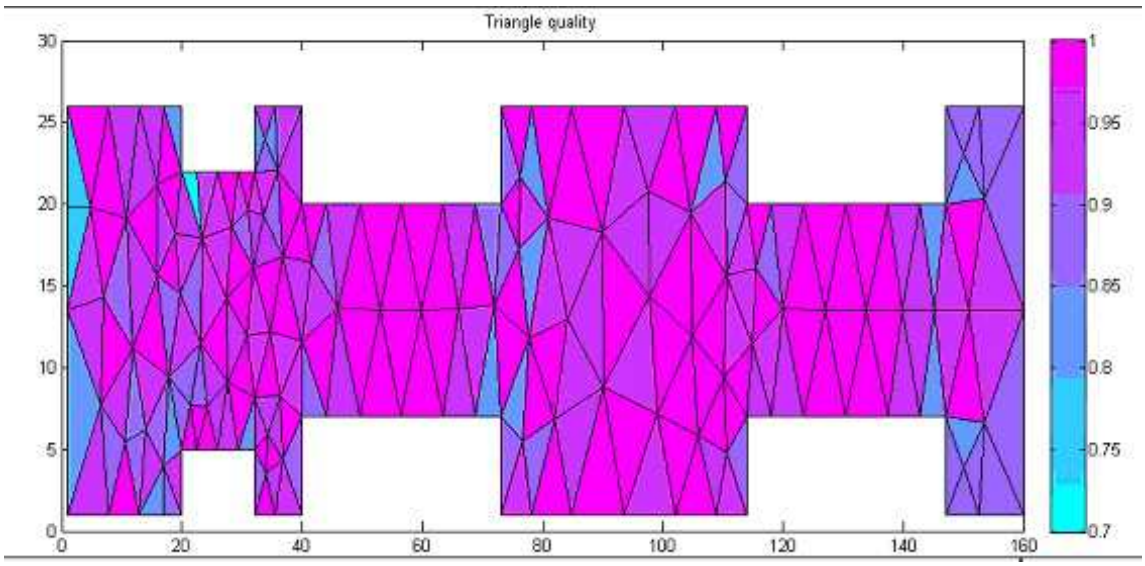

Figure 5.3: The computational mesh, colour coded to show the quality of each triangle. The three pairs of white areas represent the accelerator grids within the DS3G thruster

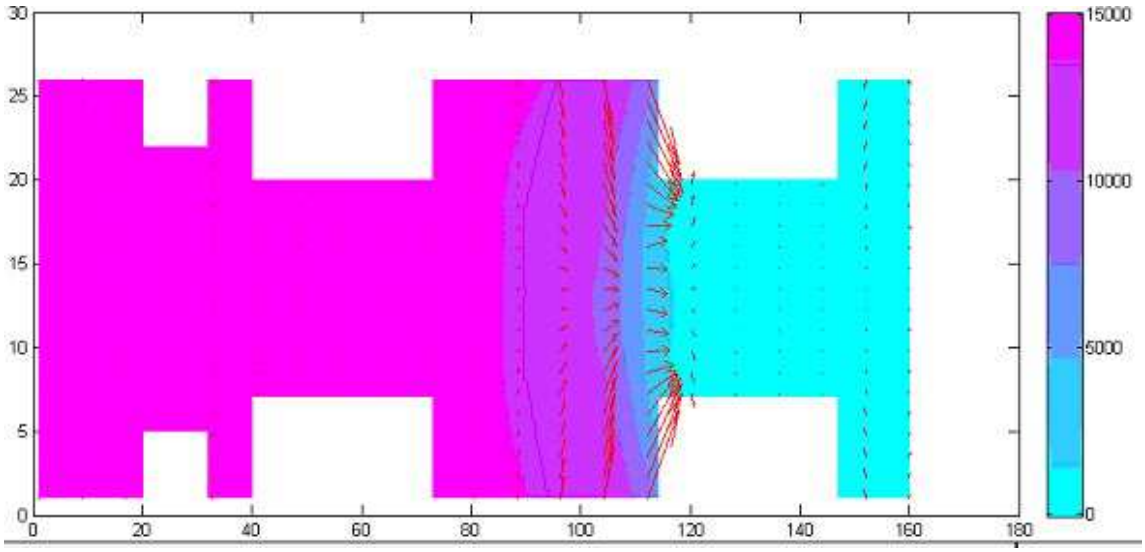

Figure 5.4: Initial potential within the simulation domain, with arrows showing the direction and strength of the electric field. Potential given in volts, arbitrary computer units along x and y axis of simulation domain

At each following timestep the dynamic fields resulting self consistently from the particle movement are calculated. The charge densities within the simulation domain due to the particles are weighted to the grid points using the weighting scheme shown in Eq.5.1 and become the right hand side of Poisson's equation, shown in Eq.5.3.

$$\bigtriangledown^2\phi = \frac{-\rho(x,y)}{\varepsilon_0} \tag{5.3}$$

The electric fields can then be calculated from ϕ using

$$\mathbf{E(x)} = - \bigtriangledown \phi(\mathbf{x}) \tag{5.4}$$

The PDEtool was chosen for the calculation of the initial fields because it provided a slightly more accurate result than was obtained by using a command line prompt. Within the simulation, Poisson's equation is solved using a built-in function of Matlab (*poicalc*), in which the solution is obtained from the charge densities at the grid points by sine transforms in the first direction and a tridiagonal matrix solution in the second direction, on the rectangular mesh. The triangular mesh used for the initial field calculations is converted to a rectangular mesh in the simulation code in order to allow it to be used with the chosen Matlab function.

5.2.3 Choice of Input Parameters

In many simulation codes the parameters and variables are normalized to optimise the numerical calculations. Parameters are originally defined in the simulation code in real units, then conversion factors are applied in order to obtain the parameters in computer units, similar to natural units. This is done to simplify calculations within the simulation code, and at the end of the simulation any relevant output parameters such as particle velocity are converted back into real units. Some parameters, such as the super particle mass M and the plasma frequency ω_p are set as 1 within the simulation code. ε_0 in Poisson's equation (Eq. 5.3) is also set to 1 within the code. All conversion factors used within the simulation code were taken from work by Birdsall and Langdon (1985) and a full list is shown in Appendix A.

For the first part of the research, in which grid configurations and voltages were manipulated in order to produce a stated specific impulse, the starting grid configurations were taken from work on the DS3G by Coletti and Gabriel (2010) and from data on the prototype DS4G shown in Table 4.1. The starting voltage V_1 for each required specific impulse is given by

$$V_1 = \frac{1}{2}\frac{M_i}{q}(g_0 I_{sp})^2 \eta_m \tag{5.5}$$

where η_m is the propellant utilization efficiency, taken from results obtained from testing of the DS4G prototype, M_i is the ion mass, q is the charge of an ion and I_{sp} is the required specific impulse.

The minimum voltage required for the third grid (V_3) in order to avoid electron backstreaming (where electrons flow backwards from the beam plasma into the thruster) is given by

$$V_3 = V_{bp} + Tln[2\frac{I_e}{I_b}\sqrt{\pi\frac{M_e}{M_i}\frac{V_1 - V_{bp}}{T}}] \tag{5.6}$$

(Coletti *et.al.*, 2010)

where V_{bp} is the beam plasma potential, which can be set to 0 for the first estimate, T is the electron temperature in eV, $\frac{I_e}{I_b}$ is the maximum backstreaming to ion beam current ratio, which is set as 0.001.

The table below shows the starting voltages calculated using Eq. 5.5 and Eq. 5.6 for specific impulses of 10,000s and 15,000s.

Specific Impulse (s)	V1	V3 (minimum required)
10,000	6294V	-41.3V
15,000	14,163V	-39.3V

Table 5.1: Voltages calculated from Eq. 5.5 and Eq. 5.6 for specific impulses of 10,000s and 15,000s

5.3 Diagnostic Techniques

5.3.1 Electric Field, Potential, Charge Density

Plots were produced showing the original potential, ϕ, at timestep 1, the charge density, ρ contributed to the system by the ions entering the simulation domain and the electric field. Examples can be seen in Figs. 5.5 to 5.9. The following figures show example results for the DS3G simulation, where the first grid has an applied voltage of 14,000V, the second 13,000V and the third 0V.

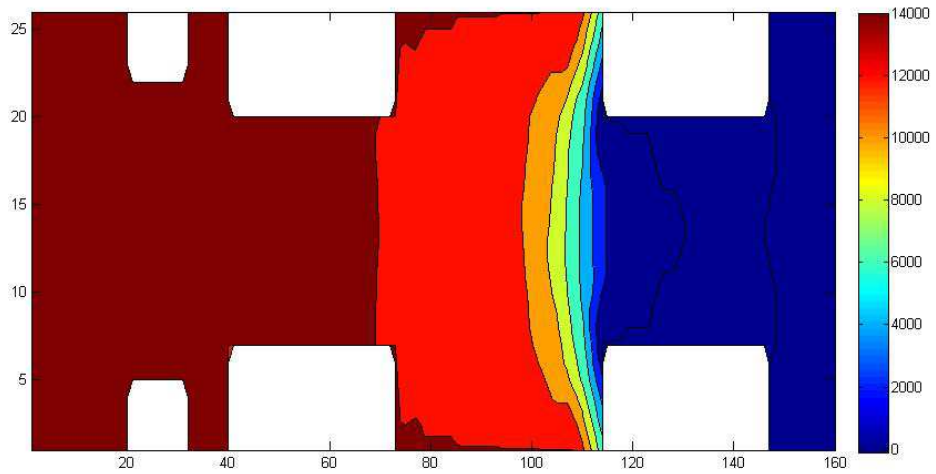

Figure 5.5: Potential within the simulation domain at timestep 1. The strong change in potential can be seen in the gap between the second and third grids. Units of potential are shown in real units (in V), simulation dimensions in arbitrary computer units

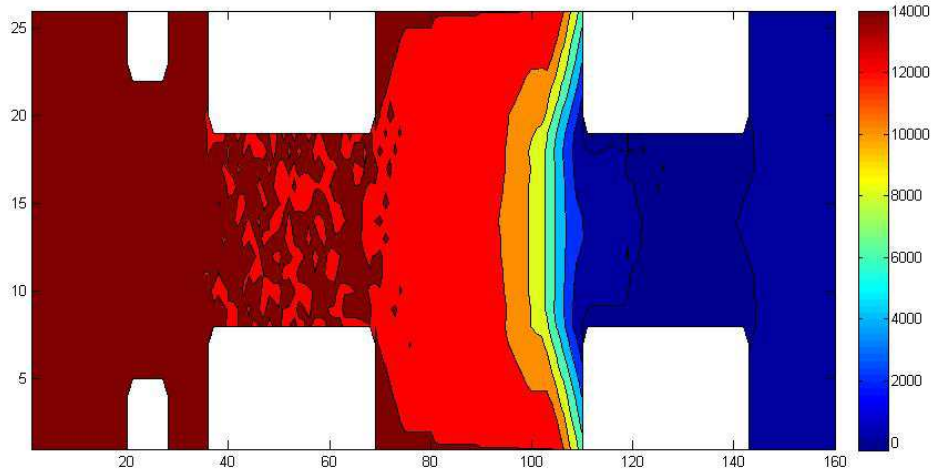

Figure 5.6: Potential at a later timestep once particles were travelling through the system. A slight alteration in the potential within the second aperture can be seen when compared to the previous figure, due to the presence of simulation superparticles. Units of potential are shown in real units (in V), simulation dimensions in arbitrary computer units

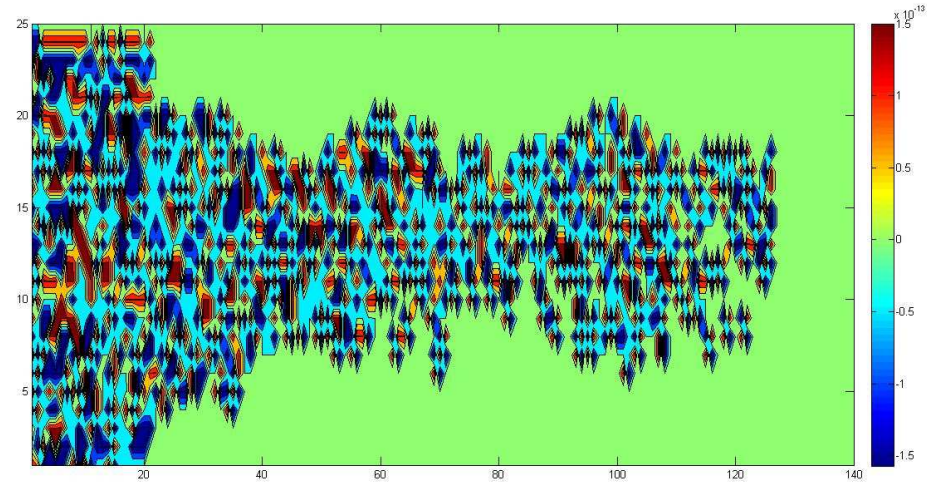

Figure 5.7: Charge density contribution from the particles within the simulation domain. The accelerator grids are not shown in this figure. Units of charge density shown in real units (Cm^{-2}), simulation dimensions in arbitrary computer units.

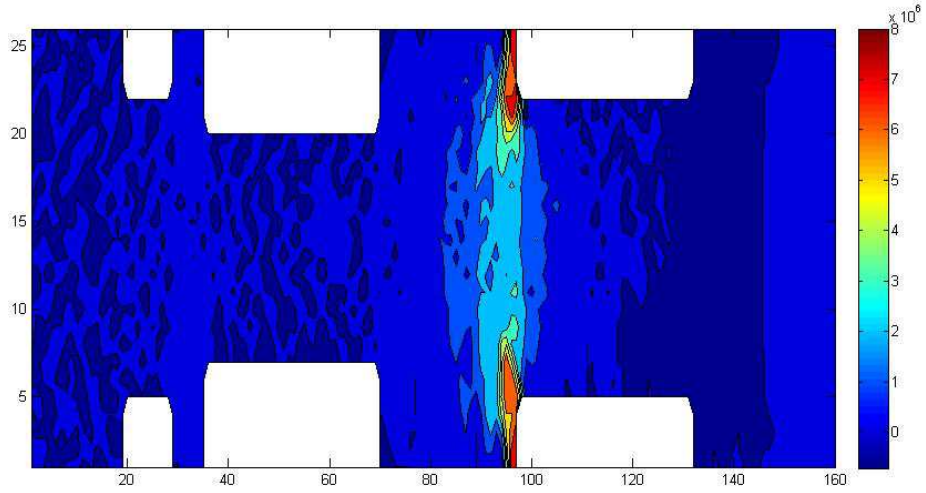

Figure 5.8: X component of the electric field. Units of electric field shown in real units (V/m), simulation dimensions in arbitrary computer units.

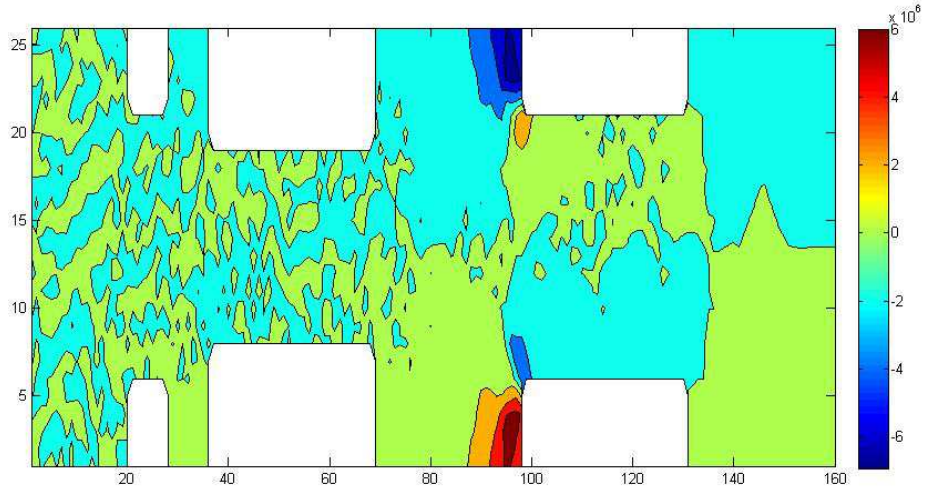

Figure 5.9: Y component of the electric field. Units of electric field shown in real units (V/m), simulation dimensions in arbitrary computer units

These diagnostics are useful for showing that the field equations within the simulation code are producing accurate results.

5.3.2 Velocity and Momentum

The change of momentum and exit velocities produced by the simulation can be compared to that calculated theoretically from the voltage applied to the ion optics using Eqs. 5.7 and 5.8.

The exit velocity of the ions passing through the right side of the simulation domain is

used to calculate the specific impulse and thrust produced, using Eqs. 5.10 and 5.9.
The theoretical change of momentum is calculated from the impulse equation,

$$\triangle p = q\frac{\triangle V}{\triangle x} \triangle t \tag{5.7}$$

where $\triangle t$ is the change in time, $\triangle V$ is the potential drop over the distance $\triangle x$ and q is the charge on an ion.
The theoretical exit velocity of the ions is calculated from

$$v_E = \sqrt{\frac{2qV_b}{M}} \tag{5.8}$$

where V_b is the net voltage within the system, q is the charge of an ion and M is the mass of an ion.
The thrust produced within the simulation is calculated using

$$F = \dot{m}_i v_{E-sim} \tag{5.9}$$

where $\dot{m}_i$ is the mass flow rate of the ionized propellant and v_E is the exit velocity of the ions leaving the simulation domain.

The specific impulse produced within the simulation is calculated from the thrust, F , using the following equation

$$I_{sp} = \frac{F}{\dot{m}_p g} \tag{5.10}$$

where $\dot{m}_p$ is the mass flow rate of propellant in kg/s, taken from the prototype DS4G test results and g is the acceleration of gravity, $9.81 m/s^2$.

5.4 Software

Several programs exist for the general simulation of plasmas, for example OOPIC, VORPAL and IGUN. It was decided that a PIC code would be self written for the simulation of ion thruster optics in order to aid understanding of the processes occurring within the ion thruster and to be used as a design tool.

The software package Matlab was chosen to write the code due to previous familiarity with the use of the software along with availability of built in functions relevant to the PIC code.
There are several advantages to writing and developing a new PIC code; firstly, writing a code from the basics builds understanding of the theories and equations behind the functioning of ion thrusters and motion of the ions. A simple simulation code can be written at first, and then built upon until the required level of complexity is achieved.

Disadvantages include the length of time that is needed to fully develop a functioning simulation, including the debugging process which can be particularly time consuming.

Any further research has to wait until the code is fully functioning and producing accurate results.

5.5 The Simulation Code

5.5.1 Development of the Simulation Code

A simple PIC code for simulating the flow of solar wind around a charged plate, written by L. Brieda (2010) and available online was studied to gain an understanding of the basics of particle in cell simulation techniques. A basic PIC simulation of a single set of apertures was then produced, in which nearest grid point weighting was used and the majority of variables were not normalised. Results plots were produced showing the potential distributions, electric fields and charge density distributions to ensure the simulation was producing realistic results.

Once this simple code was producing acceptable results it was extended; the weighting system was changed to first order, and the normalization scheme defined by Birdsall and Langdon (discussed in section 5.2) was employed in order to simplify the simulation process. The conversion factors were then applied to any results produced in order to display them in SI units for comparison and verification purposes.

Several parts of the code, for example the initialisation of the simulation domain including the position of the ion optics, the weighting of the particles to the grids and the calculation of the potential distribution using Poisson's equation were placed in separate m-files to create functions to be called by the main Matlab script. This was done to aid reading of the code and simplify the modification and debugging process. The simulation code was named PICSIE (Particle in Cell Simulation for Ion Engines) and shall be referred to as such throughout this work.

A timestep of $\Delta t = 0.2$ in computer units was chosen, converting to a timestep of $\Delta t = 4.5 * 10^{-9}$s in real units. This timestep was found to provide results with a good level of accuracy when compared to results taken from other research on the DS3G and results from testing of the DS4G prototype (see Section 4.2), while allowing a full evolution of the simulation, run to the steady state condition (to the point where changes in results from timestep to timestep become minimal) to be completed within 13 hours.

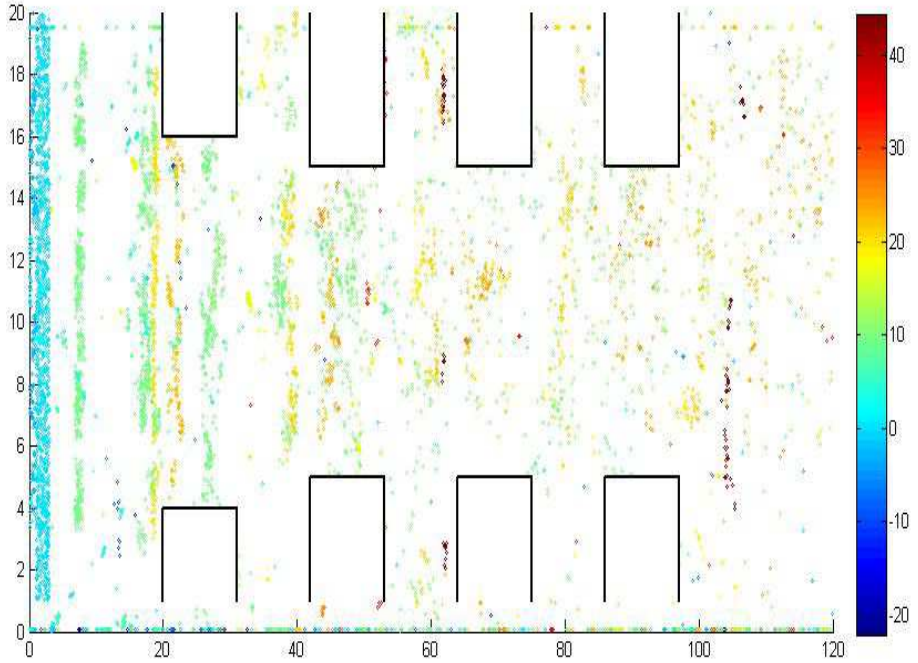

Figure 5.10: Particle positions within the 4-grid simulation domain, colour coded with respect to particle velocity in computer units - particle clumping occurring

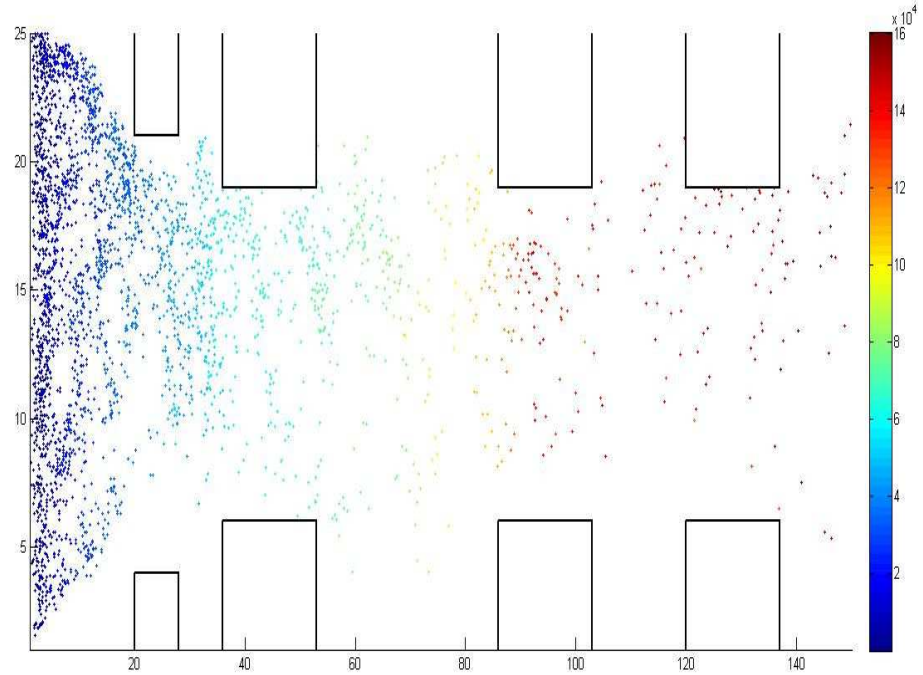

Figure 5.11: Particle positions within the 4-grid simulation domain, colour coded with respect to particle velocity in real units - no particle clumping occurring

A larger timestep of $\Delta t = 1$ produced instabilities whereby particles appeared in clumps

within the simulation domain. This is shown in Fig.5.10. The particle positions are colour coded according to velocity, and it can be seen that the velocities of the particles are not evolving consistently as they pass through the simulation domain. With the smaller timestep it can be seen in Fig.5.11 that the particle positions are much more uniform as they flow through the simulation domain, and the velocities of the particles (as denoted by the colour coding) increase uniformly as the particles progress through the simulation domain.

5.5.2 Iteration Process

At t=0 the simulation parameters are converted to computer units and initial field results are imported into the simulation code. Particles are then injected along the left hand side of the simulation domain, randomly spaced and with a Maxwellian velocity distribution. The bilinear weighting system is then applied using the group of equations shown in Eq.5.1 in order to interpolate the particle positions to the grid points and thereby calculate the charge density on the grid. The potential distribution and electric field are then calculated using equations (5.3) and (5.4), and the same weighting system is then used to weight the calculated fields back to the particles. The forces acting on each particle can then be calculated, and the new particle velocity and hence the new particle position can then be calculated. After normalization the leapfrog particle mover (Birdsall and Langdon, 1985) uses Eq. 5.11. The leapfrog scheme is an explicit, second order integration method, in which the discretization of the variables (position and velocity) are staggered in time (Oran and Boris, 1987).

$$(\frac{v\Delta t}{\Delta x})_{new} = (\frac{v\Delta t}{\Delta x})_{old} + \frac{q}{m}\frac{E_{old}(\Delta t)^2}{\Delta x} \tag{5.11a}$$

$$(\frac{x}{\Delta x})_{new} = (\frac{x}{\Delta x})_{old} + (\frac{v\Delta t}{\Delta x})_{new} \tag{5.11b}$$

The boundary conditions of the simulation are then applied; reflective boundaries are applied at the left, upper and lower edges of the simulation domain, and particles are allowed to flow freely out the right side of the simulation domain. As particles cross the boundary at the right the velocity of each particle and its position on the y axis are recorded for analysis purposes. The boundaries on the ion optics are set to absorb any particles that come in contact with them, meaning that the particles are counted then deleted from the simulation.

Reflective boundary conditions are applied on the upper and lower boundaries as in a real ion thruster particles passing through where these boundaries are in the simulation domain would pass into the next aperture area, and a similar amount of particles would be flowing the other way, from the neighbouring apertures into the studied aperture area. Therefore any particles crossing the boundaries can be reflected and considered to be particles that have passed into the simulation domain from the neighbouring aperture area.

On the left side of the simulation domain, any particles that cross that boundary, exiting the simulation domain, would be drawn back towards the ion optics by the electric fields and therefore a reflective boundary can be applied at this point.

Once the boundary conditions have been applied, the timestep is advanced and the cycle is repeated. Once a set number of timesteps is reached, final calculations are done, including the specific impulse, thrust, change in momentum and power efficiency for diagnostic purposes. The flowchart in the following section shows the order of the simulation stages in PICSIE.

5.6 Program Flow Chart

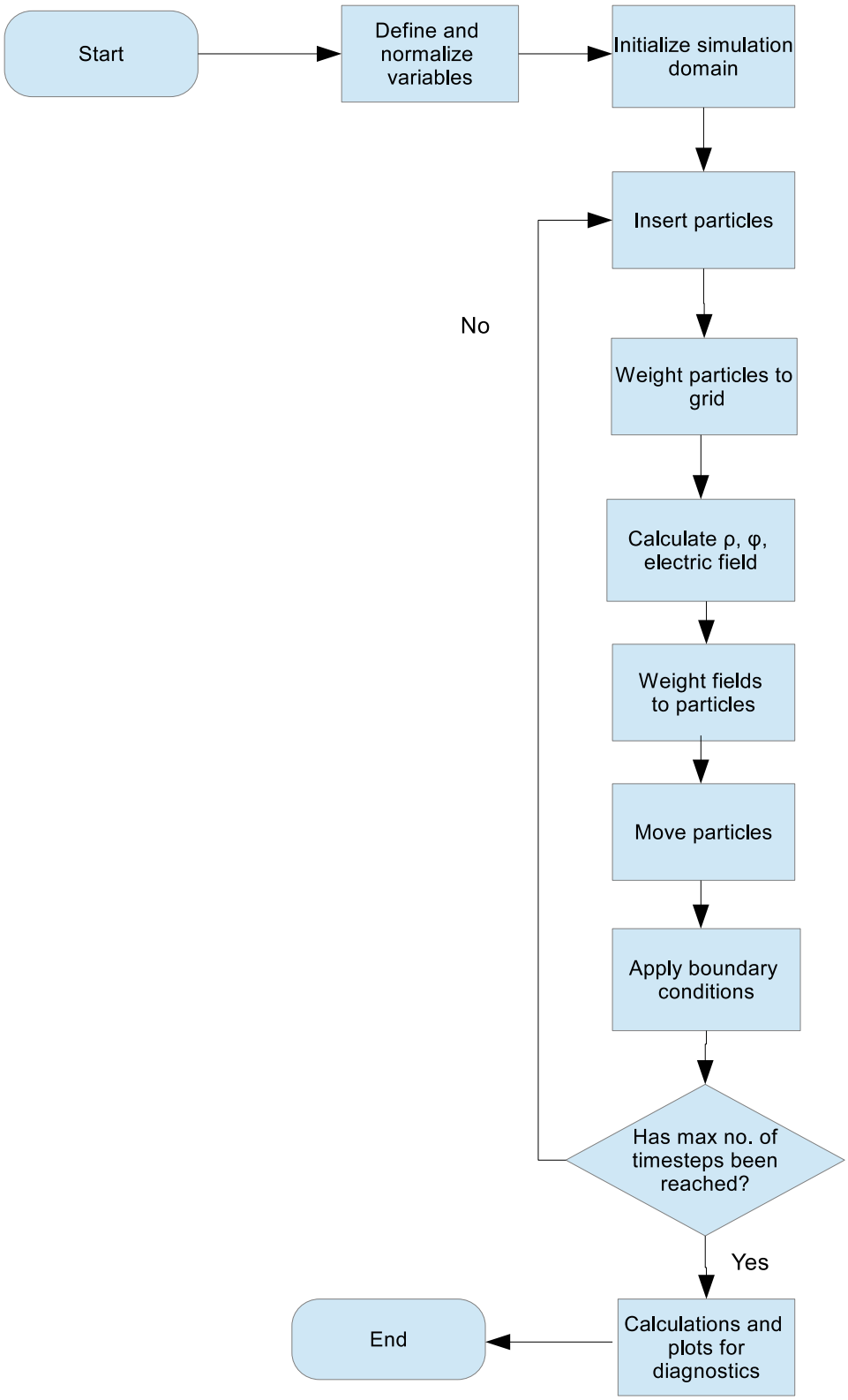

Figure 5.12: Flowchart showing the order of steps taken within PICSIE

5.7 Simulation Geometry

The length conversion factor Lf results in one cell width $\Delta x = \Delta y = C$ in computer units being equal to 0.06mm, as shown in the calculation below.

$$C(computerunits) * Lf = C(realunits) \tag{5.12}$$

$$0.2 * 3.0388 * 10^{-4} = 6.0776 * 10^{-5}(m)$$

The relevant simulation geometry parameters were then calculated from this value, including the total size of the simulation domain, the aperture sizes and the ion optics diameters.

5.8 Verification of Simulation Results

5.8.1 Dual-Stage 4-Grid Results Comparison

The table below shows a comparison between the results obtained from the prototype DS4G thruster tested in a vacuum chamber in 2006, and the results obtained from PICSIE.

Grid	Voltage	Parameter	Prototype Test Results	Simulation Results
Screen	15,000	Thrust (mN)	2.7 - 5.4	5.13
Extraction	13,000	Specific Impulse (s)	14,000	17,455
Accelerator	-200	Power Efficiency	0.4 - 0.7	0.65
Decelerator	0			
Aperture size	0.7 - 1mm			

Table 5.2: A comparison between results taken from the results of the testing of the DS4G prototype in a vacuum chamber and results obtained from the DS4G version of PICSIE

It can be seen from the table above that while the simulation result for the specific impulse is slightly higher than that obtained from the prototype testing, possibly due to the fact that the prototype set up was not optimized, the simulation results for thrust and power efficiency fall within the range obtained by the prototype.

5.8.2 Dual-Stage 3-Grid Results Comparison

The table below shows a comparison between the results presented by Coletti *et.al.* (2010) from their simulation of the DS3G ion thruster and the results obtained from PICSIE.
It can be seen from Table 5.3 that the results from PICSIE match very closely with those obtained by Coletti *et.al.* (2010) from their ffx simulation code. The result obtained for the thrust matches exactly and the result obtained for the specific impulse is only very slightly different.

The tables above show that both versions of PICSIE are producing results consistent with both experimental tests (Table 5.2) and simulations developed by other researchers (Table 5.3).

Grid	Voltage	Parameter	Result taken from Coletti *et.al.* (2010)	Simulation result
Screen	8120	Thrust (mN)	3	3
Extraction	6120	Specific Impulse (s)	10,000	10,244
Acceleration	-120	Power Efficiency	*Not Stated*	0.51
Aperture size	0.7 - 1mm			

Table 5.3: A comparison between results taken from simulation research by Coletti *et.al.* (2010) and results obtained from the DS3G version of PICSIE

5.8.3 Comparison of Calculated and Simulated Parameters

	DS4G	DS3G
Calculated $\triangle p$	$7.1 * 10^{-18}$	$7.4 * 10^{-18}$
Simulated $\triangle p$	$6.6 * 10^{-18}$	$1.1 * 10^{-17}$

Table 5.4: This table shows values for change of ion momentum for both the DS3G and DS4G, comparing values from theoretical calculations to those produced by PICSIE

The table above shows that the 4 grid version of PICSIE is producing slightly more accurate results in terms of change of ion momentum than the 3 grid code, when comparing the values produced by PICSIE to those calculated from Eq.5.7. However the results produced be the 3 grid version of PICSIE can still be considered to be reasonably accurate.

5.9 Research to be Carried Out

The first part of the research using PICSIE makes use of both the three grid and four grid versions of the code. Initial voltages were chosen as detailed in Section 5.2.3 in order to produce two specific impulses, 10,000s and 15,000s, as would be set by the functional requirements of a design for a specific space mission. During the planning stages for a space mission, scientists would look for an engine that can produce specified results in terms of thrust, specific impulse, power efficiency and lifetime. Therefore it is important that the design of a thruster can be manipulated in order to change the resulting performance parameters if the thruster is to be suitable for a wide range of missions. This stage of the research will show that the two thruster designs can be manipulated to produce two specific performance parameters without showing a negative impact on other performance indicators, as would be required if the thrusters were chosen for a space mission.

The voltages and ion optics layout were varied in order to find the most efficient combination of acceleration voltage and grid layout to produce the desired specific impulse. Once the most efficient configurations for each case are found, the three grid and four grid cases can be compared in an attempt to verify the suggestion made by Coletti *et.al.* (2010) that the fourth grid in the dual stage system provides benefits that are outweighed by the added complexity of including the extra grid. Including the extra grid means additional work in manufacturing and installing the grid, and provides another component of the thruster

that may fail. Therefore it is important in terms of both design and manufacturing effort, and expected thruster performance, that conclusions are reached regarding the benefits and disadvantages of including the fourth grid in the dual stage thruster design.

The second part of the research focuses on the three grid layout. An accelerating voltage of 15,000V was applied to the ion optics in PICSIE and the grid layout was then manipulated in order to find the configuration that produced the best results in terms of high thrust, high specific impulse, high power efficiency and low ion impaction on the grids. The parameters varied within the simulation were grid diameter, aperture diameter and spacing between the grids. This would allow comparisons to be made with other types of ion thruster, showing which thruster would produce better performance at an optimum configuration when the applied voltage is set at a certain level. It is possible that the parameters of a space mission may specify a maximum power output or available voltage, therefore it is important that a method of finding the most efficient thruster configuration for a set voltage is known in order to make the thruster available to compete on the open market for space mission contracts. Finding the most efficient grid configuration for a set voltage can reveal a lot about the internal physics of a gridded ion thruster discharge chamber; small changes in measurements can result in large changes in output parameters.

In the third part of the research a wave was propagated through the plasma in the discharge chamber, through the grid apertures. The aim of this was to see if the wave would result in improvements in key performance parameters, possibly resulting in a method of achieving improved performance in gridded ion thrusters without requiring significant increases in power consumption or major redesign efforts. If it was found that ions within the apertures were propelled through the thruster by the motion of the wave it may be possible to produce a thruster that required very little voltage applied to the grids but could still achieve good results in terms of thrust or specific impulse, meaning that less fuel would need to be carried on the spacecraft and therefore reducing the weight of the craft, or allowing the spacecraft to operate at distances far away from the sun where solar power cannot be used.

This chapter has introduced the simulation code that will be used in this research, including the techniques used in the simulation code and an introduction to the research questions that will be studied in this work. The following chapter will present some results obtained from the simulation.

6 Simulation Results and Analysis

This chapter presents results obtained from the simulation code, focusing on the problems that were introduced in the previous chapter.

6.1 Specific Impulse: 10,000s

The specific impulse, which is one of the measures of the performance of the ion thruster, represents the force produced by the thruster with respect to the amount of propellant used per unit of time. It is calculated within PICSIE from

$$I_{sp} = \frac{T}{\dot{m} g_0} \tag{6.1}$$

where T is the thrust calculated in PICSIE and $\dot{m}$ is the mass flow rate of propellant, the value of which was taken from results from the testing of the DS4G prototype thruster in a vacuum chamber. This was used as it came from a real situation as opposed to a simulation and although the prototype was not fully optimized it provides an idea as to the true performance of the thruster. The same parameters were used for the three grid simulation, as it can be assumed that the two thruster designs are identical up to the point where the grids begin and therefore parameters such as the mass flow rate of propellant can be assumed to be the same for the two designs.

When designing an ion thruster for a particular mission the design will be based on ΔV mission requirements, including the specific impulse the thruster should produce. The simulation runs detailed in this section focused on varying the grid layout and voltage profile within the thruster with the aim of producing a chosen specific impulse, and as such could be used as a design tool.

With the aim of producing a specific impulse of 10,000s, a higher value than would be produced by a traditional ion thruster but not approaching the theoretical maximum that could be produced by a dual-stage thruster, the grid configurations and applied voltage profiles for both the 3 grid and 4 grid cases were manipulated with the aim of finding the configuration that would result in the best performance for the two thrusters. Parameters used to measure the performance include the thrust, change of ion momentum, beam focusing and power efficiency, against the constraint of achieving a particular specific impulse.

6.1.1 Dual-Stage 4-Grid Simulation

Once the simulation reached a steady state, calculations were performed on the output values to determine several key parameters for analysis purposes, in particular engine performance. Outputs produced by the simulation runs included

- the exit velocities of the ions

- their point of exit on the y-axis, providing information on ion beam collimation and therefore the degree to which the ion optics are focusing the ion beam
- the amount of simulation ions that collided with the accelerating grids and were absorbed

The specific impulse, thrust, power efficiency and change in ion momentum produced by the simulated thruster and the ion beamlet focusing could then be examined in terms of their underlying cause.

Parameter	Initial Value	Parameter	Initial Value
Screen voltage	6294V	Screen thickness	0.5mm
Extraction voltage	4294V	Other grids	1mm
Acceleration voltage	-200V	Grid spacings	0.5mm/1mm/1mm
Deceleration voltage	0V	Aperture diameter	1mm/0.7mm

Table 6.1: Table showing initial input values for the four grid layout, aiming to produce a specific impulse of 10,000s

Initial input parameters were taken from information on the testing of the DS4G prototype and from theoretical calculations, and are shown in Table 6.1. The input values were then varied to observe the results with an aim of improving performance.

A selection of performance plots produced by the 4 grid version of PICSIE are shown below, along with tables showing descriptions of the varied parameters where necessary.

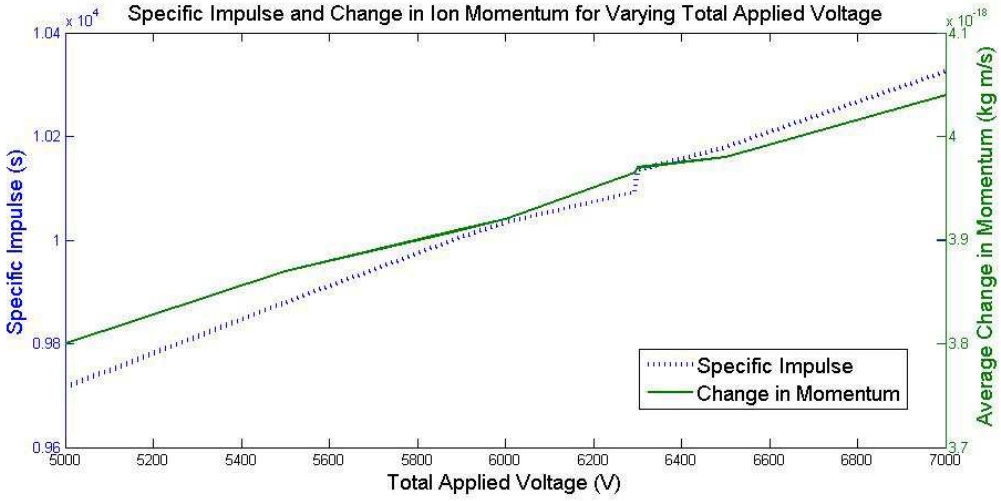

Figure 6.1: Line plot showing the specific impulse and change in momentum produced by the simulation when the total accelerating voltage applied to the grids was varied

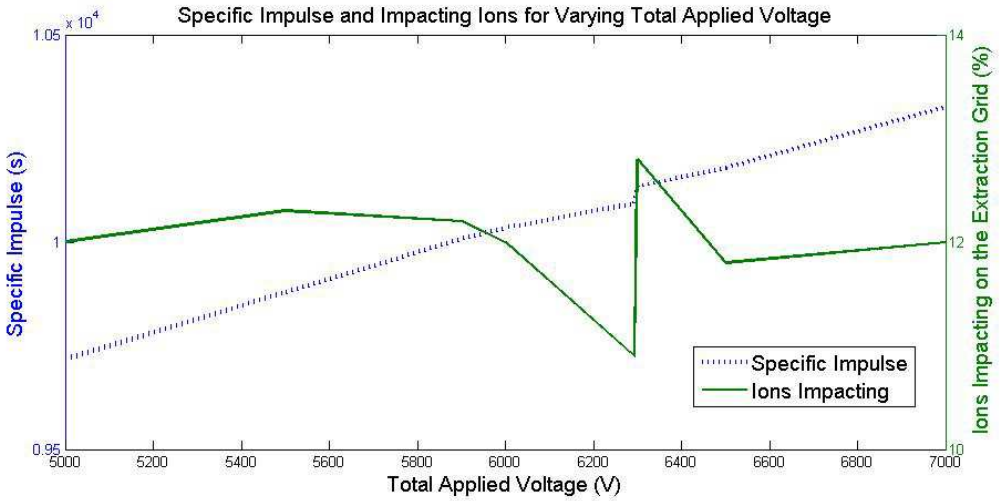

Figure 6.2: Line plot showing the specific impulse produced by the simulation and the number of ions impacting on the acceleration grid when the total accelerating voltage applied to the grids was varied

Run No.	Description
1	Drop of 1000V in the Extraction stage, Grid 3 set at -100V
2	Drop of 2000V in the Extraction stage, Grid 3 set at -100V
3	Drop of 2000V in the Extraction stage, Grid 3 set at -150V
4	Drop of 2000V in the Extraction stage, Grid 3 set at -200V
5	Drop of 3000V in the Extraction stage, Grid 3 set at -100V
6	Drop of 1500V in the Extraction stage, Grid 3 set at -100V

Table 6.2: Table showing a description of the simulation runs where the voltage profile applied to the accelerating grids was varied from a set screen grid voltage

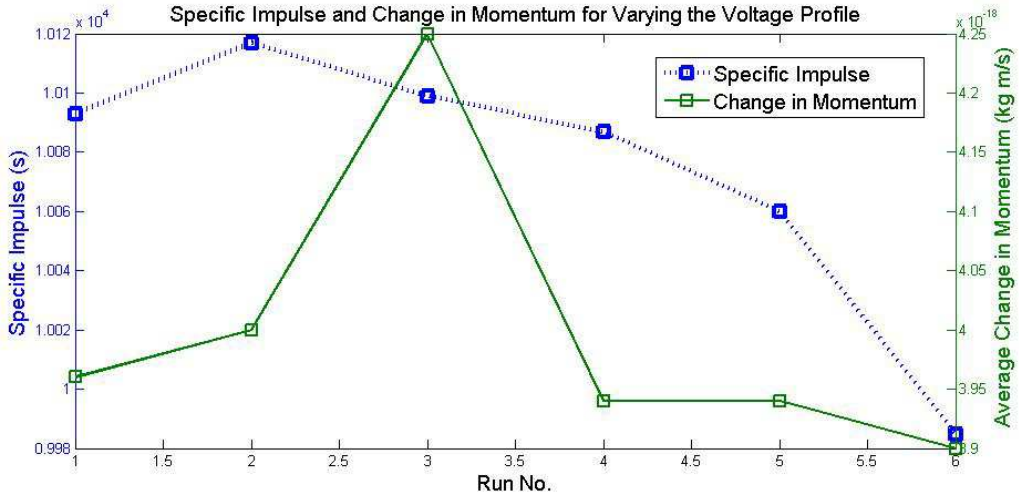

Figure 6.3: Line plot showing the specific impulse and change in momentum produced by PICSIE for simulation runs in which the voltage profile across the grids was varied. A description of the simulation runs is shown in Table 6.2

Run No.	Description		
	Screen Aperture	Extraction Aperture	Acceleration Aperture
1	0.9mm	0.6mm	0.6mm
2	1mm	0.7mm	0.7mm
3	1.5mm	1.05mm	1.05mm
4	1.5mm	1.2mm	1.2mm

Table 6.3: Table showing a description of the simulation runs where the aperture size was increased with run number

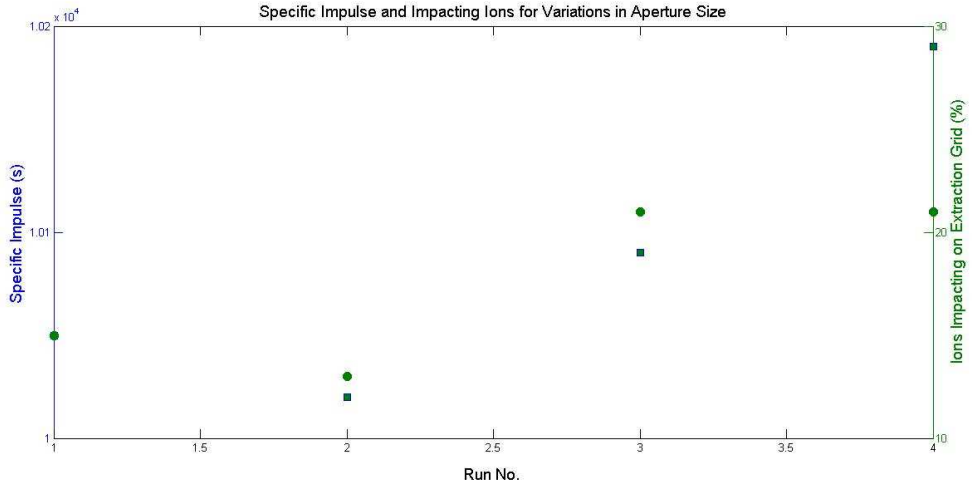

Figure 6.4: Line plot showing the specific impulse produced by PICSIE and the percentage of simulation ions that collided with the extraction grid for simulation runs in which the aperture size was increased. A description of the simulation runs is shown in Table 6.3

Run No.	**Description: Gap1/Gap2/Gap3**
1	0.5mm/1mm/1mm
2	0.5mm/2mm/1mm
3	1mm/2mm/1mm
4	0.5mm/2mm/2mm

Table 6.4: Table showing the simulated variations in spacings between the accelerating grids

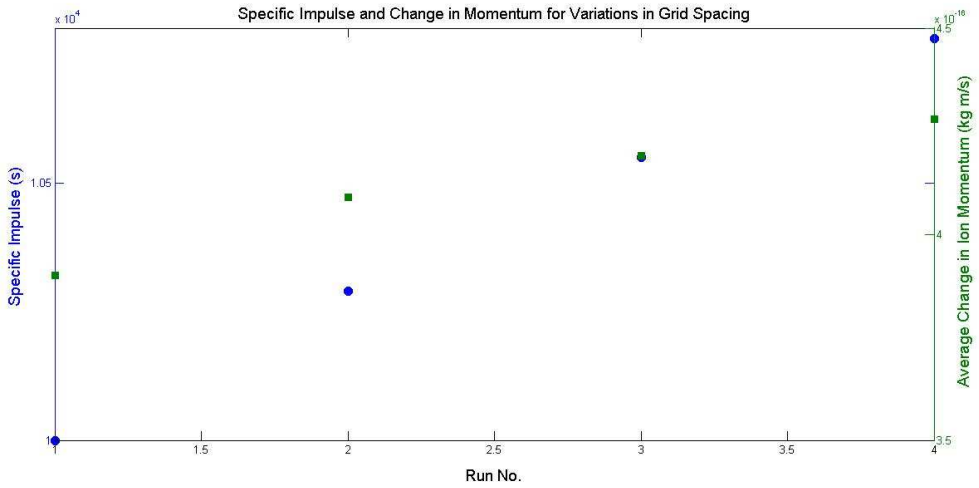

Figure 6.5: Line plot showing the specific impulse and change in ion momentum produced by PICSIE for simulation runs in which the spacings between the accelerating grids were varied, with a fixed voltage profile. A description of the simulation runs is shown in Table 6.4

It can be seen in Fig.6.1 that as the total applied voltage is increased the I_{sp} and average change in ion momentum also increase. The total applied voltage is the voltage difference between the first grid and the third grid (as the fourth grid is set to 0V).

It can be seen in Fig.6.3 that the highest average change in ion momentum was produced in Run no.3, where a voltage drop of 2000V was applied in the extraction stage and a voltage of -150V was applied to the acceleration grid. An increase of almost 1% can be seen when compared to the previous simulation run.

The spacings between the grids were varied, with run numbers and corresponding measurements shown in Table 6.4. Gap 1 refers to the spacing between the screen grid and extraction grid, Gap 2 refers to the spacing between the extraction grid and acceleration grid, while Gap 3 refers to the spacing between the acceleration grid and deceleration grid. It can be seen in Fig.6.5 that the two lines indicating changes in specific impulse and change in ion momentum do not share the same gradient. While both parameters increase steadily throughout the simulation runs the specific impulse increases at a slightly higher rate than the change in momentum. The aperture sizes were then varied, starting with measurements slightly smaller than those suggested in previous research (see Section 3) and increasing to a maximum aperture size of 1.5mm for the first grid. The simulation run numbers corresponding to the different aperture sizes can be seen in Table 6.3.

6.1.2 Dual-Stage 3-Grid Simulation

Initial input values for the three grid version of PICSIE were taken from other researchers' work on the DS3G thruster (Coletti *et.al.*, 2010) and from theoretical calculations (Equations 5.5 and 5.6). These initial values are shown in the table below. These inputs were

then adjusted to observe the results.

Parameter	Initial Value	Parameter	Initial Value
Screen Voltage	6294V	Screen Thickness	0.5mm
Extraction Voltage	4294V	Extaction/Acceleration Thickness	2mm
Acceleration Voltage	-120V	Extraction gap/Acceleration gap	0.5mm/2.5mm
		Aperture Diameter - Screen/others	1mm/0.7mm

Table 6.5: Table showing the initial input parameters for the three grid layout, aiming for a specific impulse of 10,000s

The plots below show the connection between increase in specific impulse and increases in ion momentum produced by PICSIE and in the amount of simulation ions being absorbed by the extraction grid as the total voltage applied to the accelerating grids was altered.

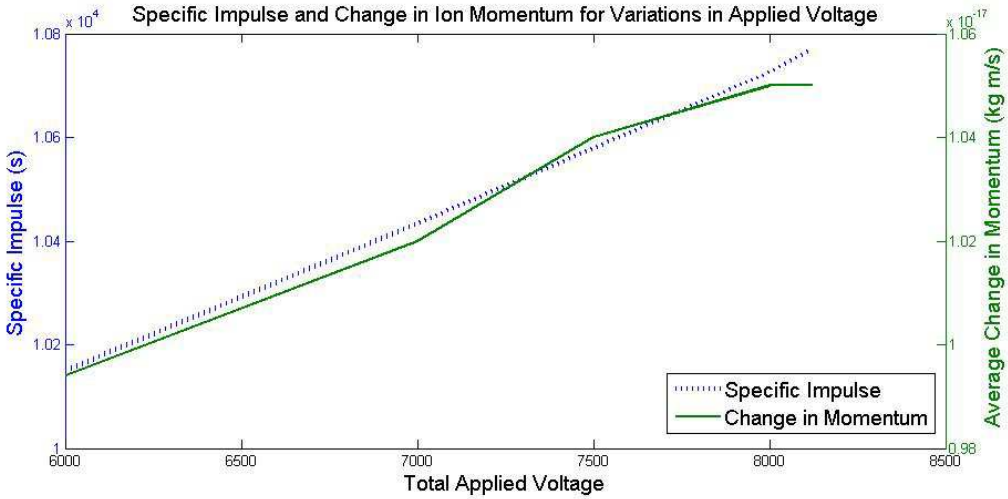

Figure 6.6: Line plot showing the specific impulse and change in momentum produced by PICSIE when the total accelerating voltage applied to the grids was varied

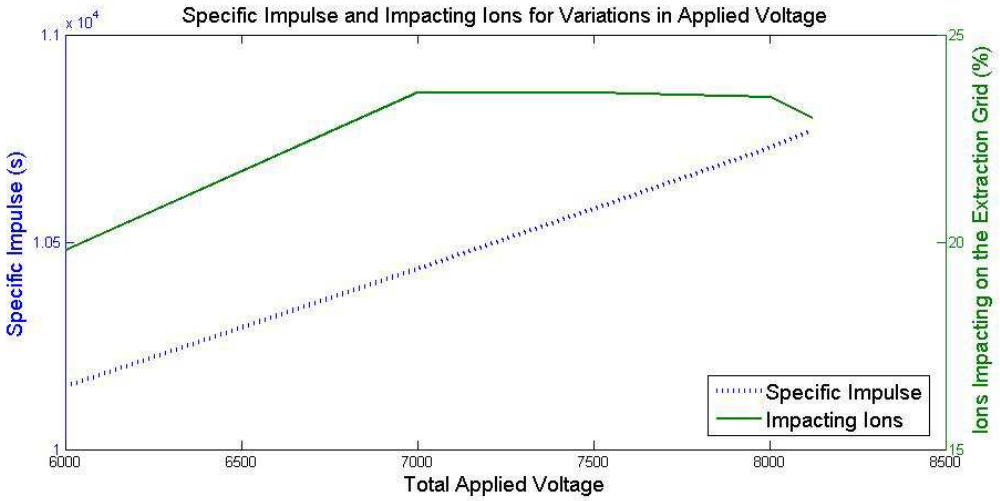

Figure 6.7: Line plot showing the specific impulse produced by the simulation and the amount of simulation ions colliding with the extraction grid when the total accelerating voltage applied to the grids was varied

The similar gradients of the increase in specific impulse and the increased change of momentum can be seen in Fig.6.6, although a slight cross over can be seen at 7500V, suggesting a strong correlation between specific impulse and change in momentum. However, although the three grid and four grid cases produce similar specific impulse values, the average change in ion momentum observed in the two cases are strikingly different. Therefore, although it can be said that as the specific impulse increases so does the average change in ion momentum, a specific value of specific impulse cannot be linked to a specific value of change in momentum.

6.2 Specific Impulse: 15,000s

The simulation process was then repeated with the aim of producing a specific impulse of 15,000s. It can be deduced from Equation 2.1 that a higher specific impulse would maximise the useful payload of a spacecraft, therefore an ion thruster than could produce a specific impulse of 15,000s, considered high in comparison to other thrusters, would be desirable.

6.2.1 Dual-Stage 4-Grid Simulation

Initial values for the grid layout are as shown in Table 6.1, and initial values for the voltage profile are shown in Table 6.6.

Grid	Voltage
Screen	14,163V
Extraction	12,163V
Acceleration	-100V
Deceleration	0V

Table 6.6: Table showing the initial voltage profile for the four grid layout, aiming to produce a specific impulse of 15,000s. Actual specific impulse produced:16,478s

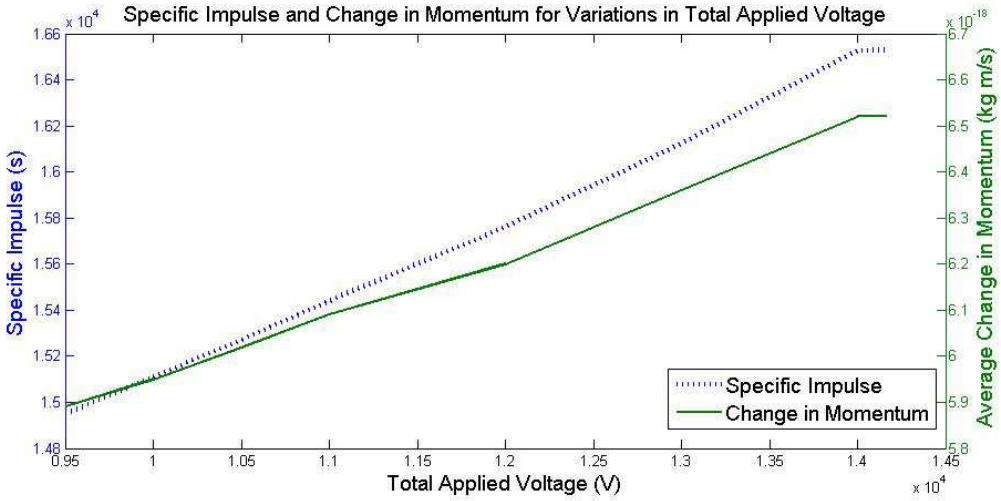

Figure 6.8: Line plot showing the specific impulse and change in momentum produced by the simulation when the total accelerating voltage applied to the grids was varied

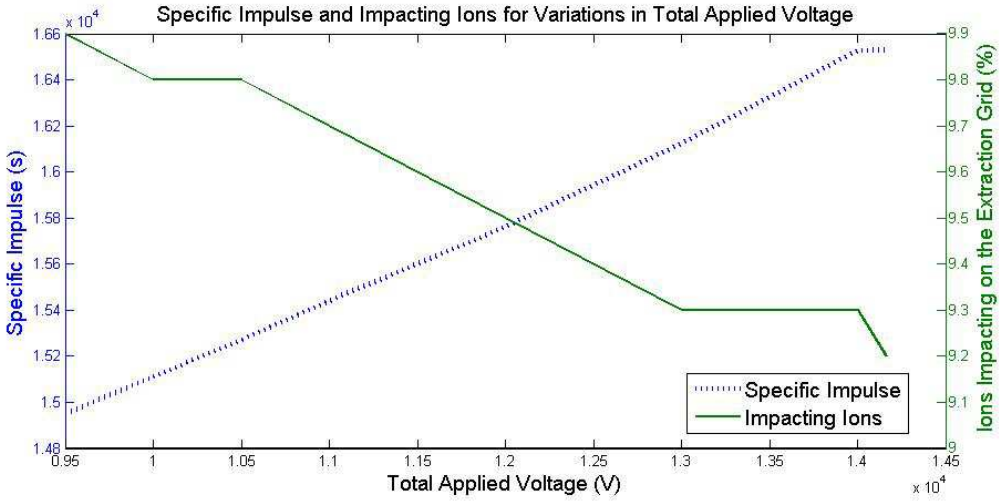

Figure 6.9: Line plot showing the specific impulse produced by PICSIE and the amount of simulation ions colliding with the extraction grid when the total accelerating voltage applied to the grids was varied

Run No.	Description: Gap1/Gap2/Gap3
1	0.5mm/1mm/1mm
2	0.5mm/2mm/1mm
3	1mm/2mm/1mm
4	0.5mm/2mm/2mm

Table 6.7: Table showing the simulated variations in spacings between the accelerating grids

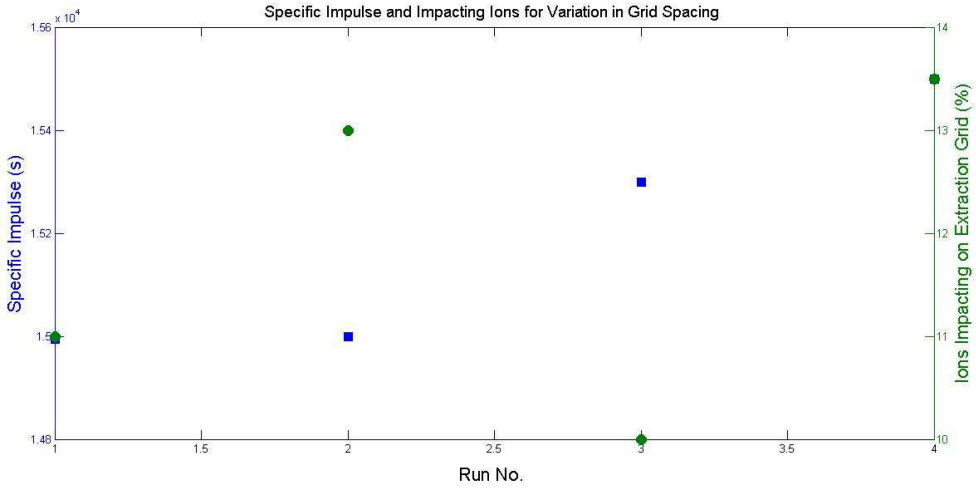

Figure 6.10: Line plot showing the specific impulse produced by PICSIE and the amount of simulation ions colliding with the extraction grid when the spacings between the accelerating grids was varied. Refer to Table 6.7 for description of simulation runs.

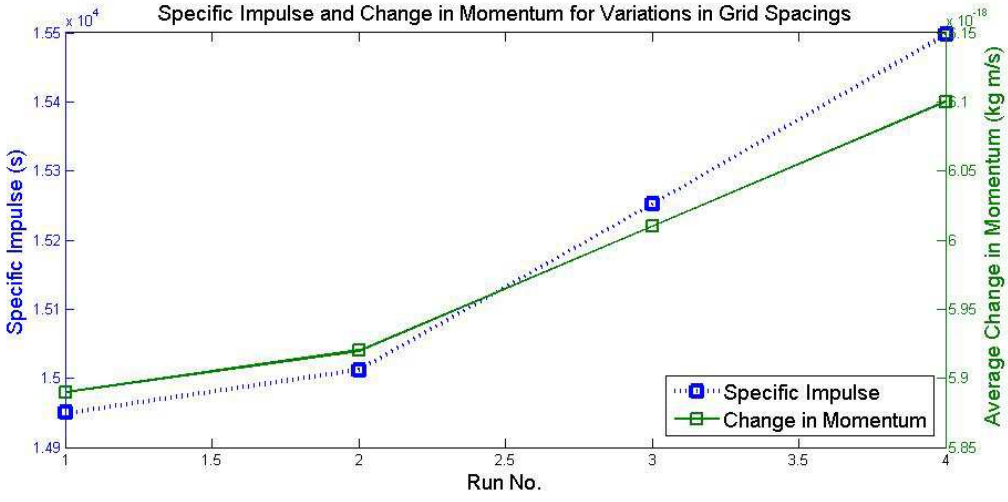

Figure 6.11: Line plot showing the specific impulse and change in ion momentum produced by PICSIE when the spacings between the accelerating grids were varied. Refer to Table 6.7 for description of simulation runs.

The spacings between the grids were varied, with simulation run numbers and corresponding measurements shown in Table 6.7. Gap 1 refers to the spacing between the screen grid

and extraction grid, Gap 2 refers to the spacing between the extraction grid and acceleration grid, while Gap 3 refers to the spacing between the acceleration grid and deceleration grid. Figure 6.8 shows the changes in specific impulse and average change in ion momentum as the total applied voltage was increased; as previously observed, there is a strong correlation between the two parameters. This correlation can also be observed in Figure 6.11 as the spacings between the grids are varied. Figure 6.9 shows a strong negative correlation between the number of ions impacting on the extraction grid and the specific impulse produced by the thruster as the voltage is increased. This is possibly due to the increased voltage forcing a greater degree of beam collimation on the ion beamlet, reducing impact on the grids. It can be seen in Fig.6.10 that while the specific impulse increases throughout the simulation runs there is more variation in the number of ions impacting on the extraction grid. However despite seemingly large variations in ion impaction when compared to specific impulse, due to the scale of the graph these variations in ion impaction are small (around 3% variation).

6.2.2 Dual-Stage 3-Grid Simulation

With an aim of producing a target specific impulse of 15,000s using the three grid thruster layout, the initial grid layout was as shown in Table 6.5 and the initial voltage profile is shown in the table below.

Grid	Voltage
Screen	14,163V
Extraction	12,163V
Acceleration	-120V

Table 6.8: Table showing the initial voltage profile for the three grid layout, aiming to produce a target specific impulse of 15,000s. Actual specific impulse produced: 16,484s

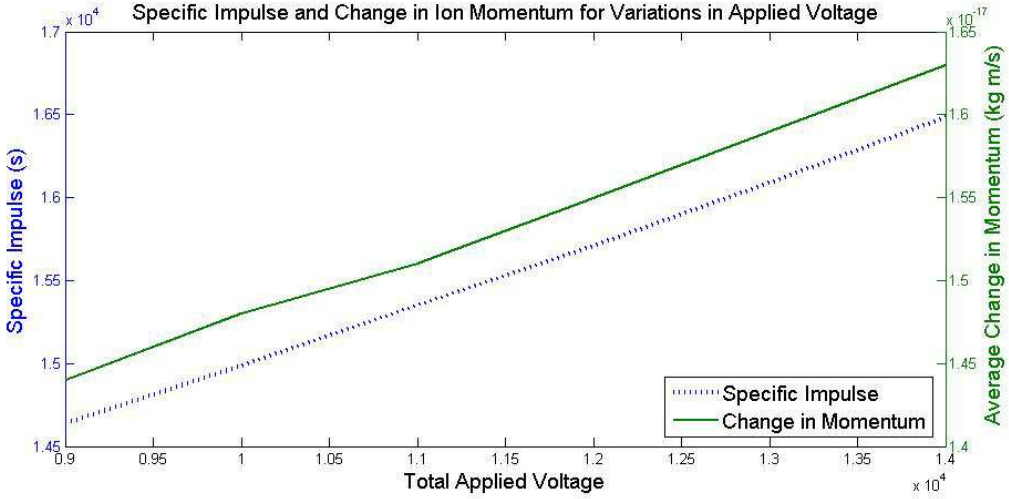

Figure 6.12: Line plot showing the specific impulse and change in momentum produced by PICSIE when the total accelerating voltage applied to the grids was varied

The strong positive correlation between specific impulse and average change in ion momentum that has been observed above can be seen again in Figure 6.12. However due to the scale on the figure the increase in specific impulse shown in the figure is significantly greater than the increase in the average change in ion momentum.

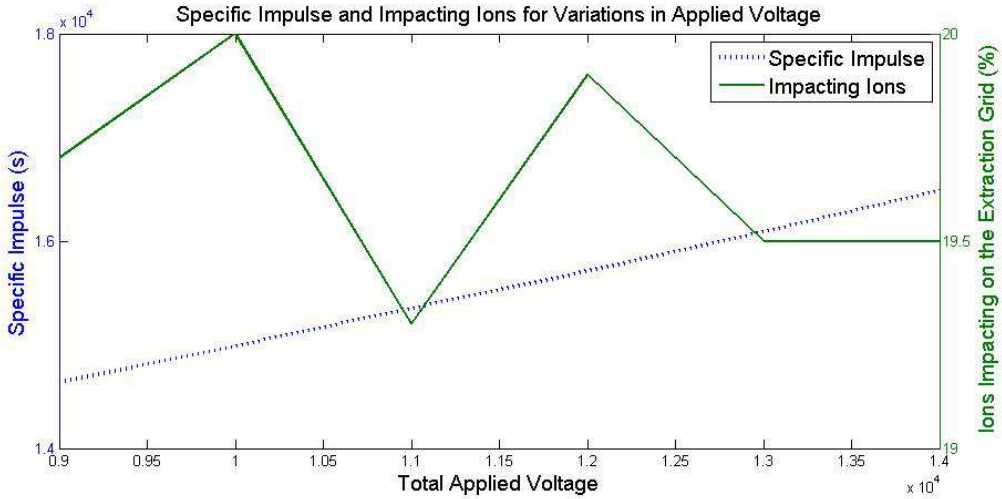

Figure 6.13: Line plot showing the specific impulse produced by PICSIE and the amount of simulation ions colliding with the extraction grid when the total accelerating voltage applied to the grids was varied

In Figure 6.13 sharp fluctuations in the number of ions impacting on the extraction grid can be seen. However, it can be observed that due to the scale on the axis these fluctuations account for changes of less than 1% in real terms and the effect is not as dramatic as the figure suggests.

6.3 Optimization of the DS3G Configuration

This part of the research focuses on applying a set voltage profile to the accelerating grids within the three grid thruster and varying the configuration of the grids, with the aim of producing the maximum possible specific impulse and change in ion momentum while minimising the amount of simulation ions impacting on the grids and achieving the best focusing of the ion beamlet.

Accelerating Grid	**Applied Voltage**
Screen Grid	15,000V
Extraction Grid	14,000V
Acceleration Grid	-100V

Table 6.9: Table showing the voltage profile applied to the three grid layout

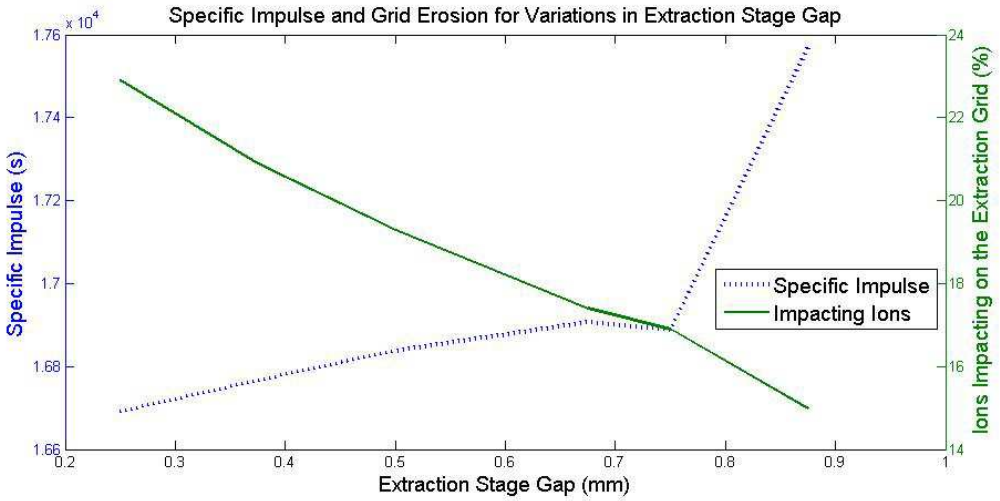

Figure 6.14: Line plot showing the specific impulse produced by PICSIE and the amount of simulation ions colliding with the extraction grid when the gap between the screen grid and extraction grid was varied

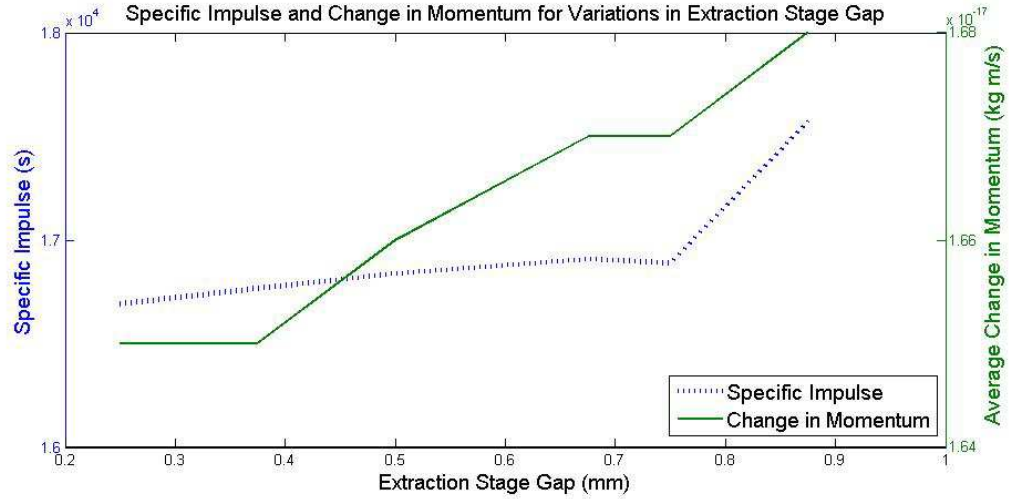

Figure 6.15: Line plot showing the specific impulse and change in momentum produced by PICSIE when the gap between the screen grid and extraction grid was varied

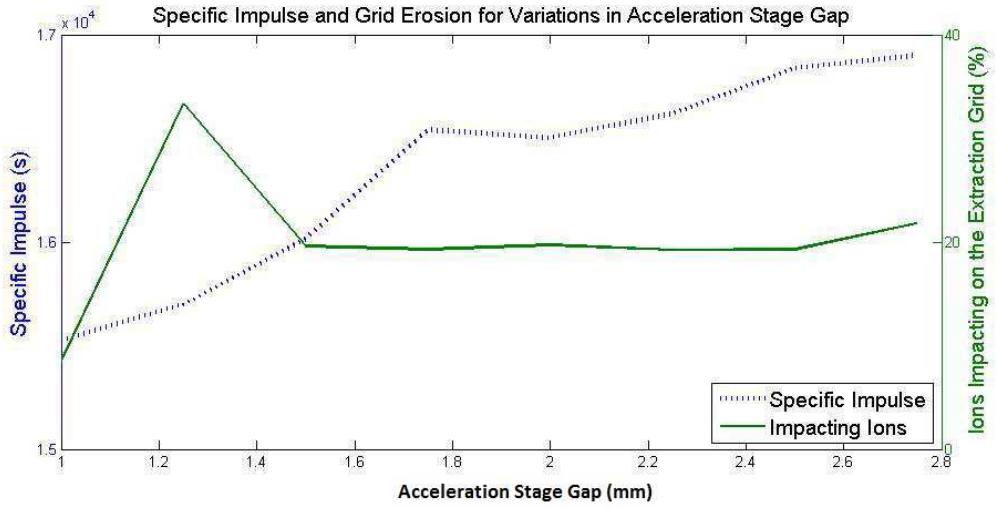

Figure 6.16: Line plot showing the specific impulse produced by PICSIE and the amount of simulation ions colliding with the extraction grid when the gap between the extraction grid and acceleration grid was varied

The plots shown in Fig.6.14 to Fig.6.16 show the variation in the specific impulse produced by PICSIE as the spacings between the grids are varied along with the amount of particles impacting on the second grid, which relates to the focusing of the ion beam. A higher number of ions impacting on the extraction grid indicates poor collimation of the ion beam, indicating that the grids are not properly focusing the ions through the apertures. Figure 6.14 shows a strong negative correlation between the specific impulse and the number of ions impacting on the grids as the extraction stage gap is varied. A larger extraction stage gap results in a higher specific impulse and fewer ions impacting on the grid, suggesting that the size of this gap impacts on the degree of collimation of the ion beamlet. Figure 6.15 shows that the average change in ion momentum also increases as the extraction stage gap increases; however the correlation between these two parameters is not as strong in this case as in the results presented in the previous sections, suggesting that another parameter has an impact on the degree of correlation between these two parameters.

Figure 6.15 shows a sharp increase in the number of ions impacting on the extraction grid at an acceleration stage gap of around 1.25mm. In previous figures showing the impact of ions on the extraction grid the small scale on the axis has led to the effect of small changes being exaggerated in the figure. However this is not the case here, as it can be observed that at around 1.25mm an increase of around 10% occurs. Although further simulation runs using acceleration stage gaps around this length would be needed to achieve a firm understanding of the reason for this increase, it suggests that an acceleration stage gap of 1.25mm should be avoided.

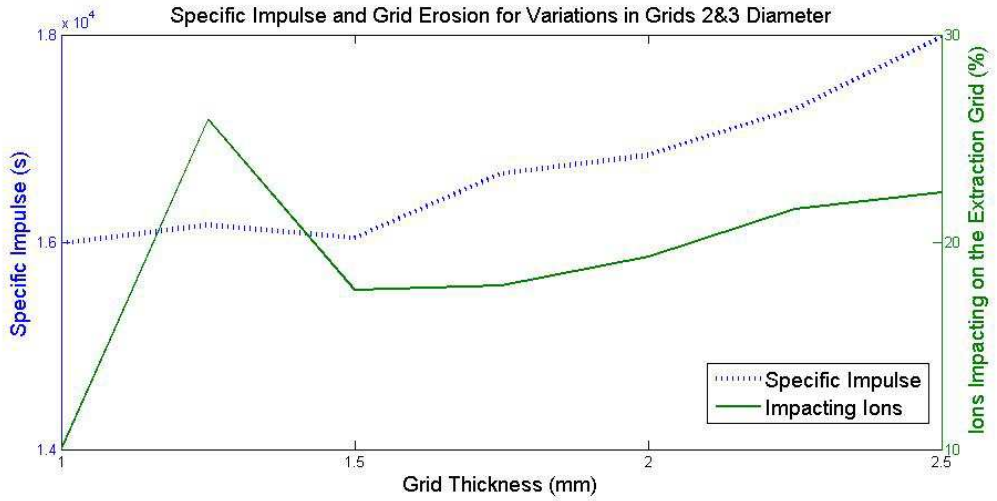

Figure 6.17: Line plot showing the specific impulse produced by PICSIE and the amount of simulation ions colliding with the extraction grid when the diameters of the second and third grids were varied

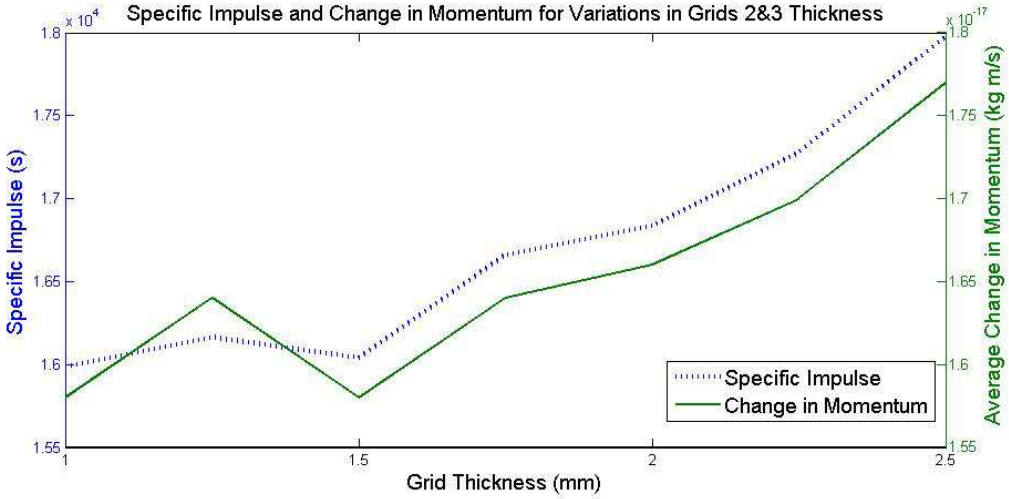

Figure 6.18: Line plot showing the specific impulse and average change in ion momentum produced by PICSIE when the diameters of the second and third grids were varied

A less significant increase (of around 6%) in the number of ions impacting on the grid can be seen in Figure 6.17 for a grid thickness of 1.3mm, suggesting that this grid thickness should be avoided in order to achieve a good degree of beam collimation. Figure 6.18 shows a small increase in the average change in ion momentum at this grid thickness, although due to the scale on the figure the difference in real terms is very small.

Parameter	**Chosen Value**
Grid Thickness: Screen/Extraction/Acceleration	0.7mm/2mm/2mm
Grid Spacing: Gap1/Gap2	0.6mm-0.9mm/2.5mm
Aperture diameter	1mm/0.7mm
Parameter	**Simulation Result**
Specific Impulse	17,280s
Thrust	5.1mN
Change in Momentum	1.7e-17 kg m/s

Table 6.10: Table showing the chosen values for the accelerating grids layout and the results produced by PICSIE for a total applied voltage of 15,000V

For a total applied voltage of 15,000V the grid configuration producing the best results as determined by specific impulse, thrust, change in ion momentum and beam collimation and the results produced by PICSIE are shown in Table 6.10. A thrust of 5.1mN and a specific impulse of 17,280s were found to be the maximum available for the set voltage while minimizing the ions impacting on the grids and maximising the ion beamlet focusing, as determined by the spread of exiting ions along the y axis of the simulation domain.

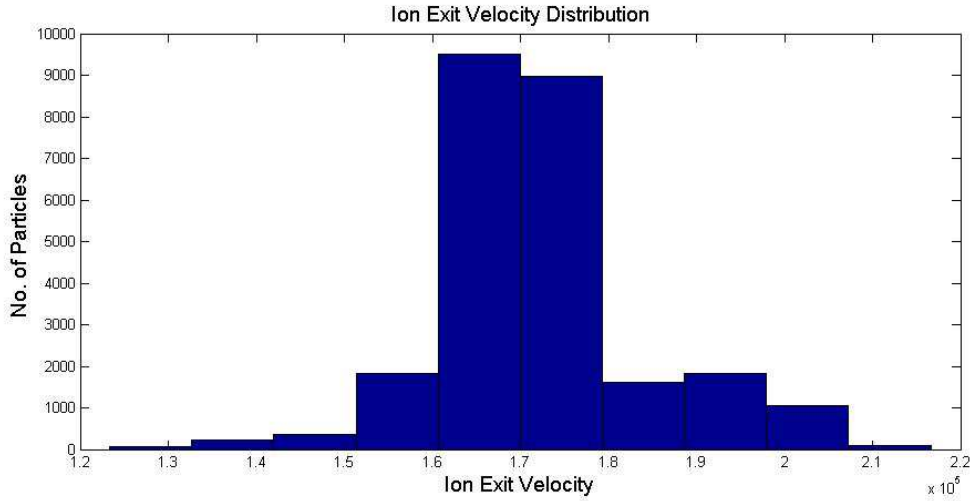

Figure 6.19: Histogram showing the distribution of particle exit velocities, in real units

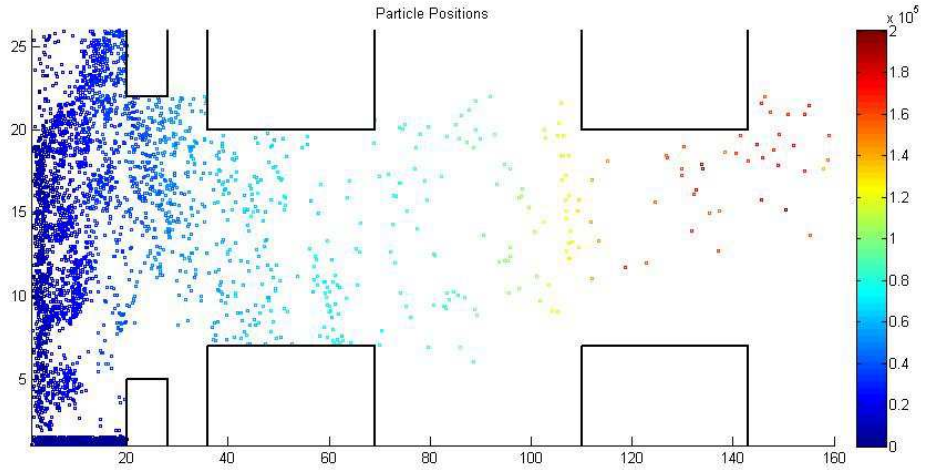

Figure 6.20: Scatter plot of the particle distribution within the simulation domain, colour coded with respect to the velocity of the particles. Simulation dimensions shown in computer units, colour coded in real units

Plots taken from a simulation run using the values shown in Table 6.3 are shown in Figs.6.19 and 6.20. The distribution of the particle velocities as they exit the simulation domain is shown in Fig.6.19 and a scatter plot of the particle positions within the simulation domain is shown in Fig.6.20, colour coded to show the velocity of the particles.

Figure 6.19 shows the distribution of particle velocities as they exit the simulation domain; the distribution is still approximately Maxwellian, corresponding to the Maxwellian distribution of the particle velocities as they entered the simulation. The particles maintaining their velocity distribution indicates that the majority of particles receive roughly the same increase in velocity when passing through the thruster. Figure 6.20 shows that the particle velocities increase at the expected points within the simulation domain, receiving a significant increase in velocity as they approach the acceleration grid.

6.4 Introducing Waves Into the Thruster

This part of the research focuses on using a directed wave within the plasma to test the novel idea of propelling the particles through the ion engine. The aim is to discover whether propagating a wave through the plasma within a dual-stage ion thruster could increase the specific impulse, thrust and change in momentum produced by the thruster.

The reasoning behind beginning an investigation into the concept of propagating a wave through the plasma within the discharge chamber is that it was thought that if a wave travels through the centre of a grid aperture, any ions that happen to be in the path of the wave would be propelled along by the motion of the wave, potentially increasing the speed of these particles. However there could be negative consequences to this, for example if the motion of the wave forces particles out of the collimated ion beamlet and into the grids, resulting in erosion, or results in increased interaction between the ion beamlets in

neighbouring grid apertures.

6.4.1 Oscillating Grid Potentials

An attempt was made to introduce a wave into the plasma within the simulation domain. Firstly an oscillating potential was applied to the ion optics; two frequencies of oscillation were simulated, firstly with the potential changing at each timestep and secondly changing every 5 timesteps. The aim was to oscillate the potential at a frequency that corresponded to the time taken for a particle to pass from one grid aperture to the next. Two frequencies of oscillation were examined due to the fact that the time taken for a particle to pass from the first aperture to the second is greater than that taken for a particle to pass from the second to the third aperture. Two oscillating frequencies were studied, firstly oscillating the screen grid potential between 15,500V and 14,500V and then oscillating the screen grid potential between 15,000V and 0V. The extraction grid potential followed a reverse pattern in each case, while the acceleration grid oscillated between -150V and -50V in the first case and remained at -100V in the second case.

	Oscillation each Δt	Oscillation each 5 x Δt
Specific Impulse (s)	16.786	16,817
Change of Momentum (kg m/s)	1.65e-17	1.65e-17
Thrust (mN)	4.9	4.9
Ions Impacting on Extraction Grid (%)	19.6	19.2

Table 6.11: Table showing the results obtained when oscillating grid potentials

	Optimized Grid Layout
Specific Impulse (s)	16,848
Change of Momentum (kg m/s)	1.67e-17
Thrust (mN)	5
Ions Impacting on Extraction Grid (%)	19.7

Table 6.12: Table showing the results produced by the optimized grid configuration

This method of introducing a wave into the plasma was found to produce no changes in specific impulse, thrust and change in ion momentum when compared to the standard fixed potential grid system, as can be seen in Table 6.11 and Table 6.12. It was therefore considered to be an unproductive route and no further research was pursued in this direction during this work. An alternative method of propagating a wave through the discharge chamber was then investigated.

6.4.2 Ion Acoustic Waves

An ion acoustic wave was propagated through the centre of the simulated aperture to see if this would affect the performance of the thruster. There were many possible types of waves that could have been chosen for this work and there was no particular reason behind the choosing of the ion acoustic wave. The intention of this was to investigate the concept

of waves within the discharge chamber plasma, and if no benefits were found or if negative consequences resulted from this type of wave being used within the ion thruster there are many other types of waves which could be investigated.

The equation of momentum for the ions in an ion acoustic wave is

$$m_i n\{\frac{d\mathbf{v}}{dt} + (\mathbf{v}\cdot\nabla)\mathbf{v}\} = -\gamma k_B(T_i + T_e)\nabla n \tag{6.2}$$

where m_i is the mass of an ion, n is the number density of the ions, $\mathbf{v}$ is the ion velocity, γ is the heat capacity ratio, k_B is the Boltzmann constant and $T_{i,e}$ are the ion and electron temperatures. The phase velocity of the ion acoustic wave is given by

$$\frac{\omega}{k} = \sqrt{\frac{\gamma}{k}_{B0(T_i+T_e)} m_i} \tag{6.3}$$

The simulation code was modified to include the ion acoustic wave, propagating it through the centre of the grid apertures. During the simulation, any particles that happened to be in the path of the wave had their motion manipulated to correspond to interaction between the wave and the ions. Changes of direction and acceleration due to the wave were applied to the particles along with the standard leapfrog particle mover used throughout this work. An ion acoustic velocity of 1200m/s was used in the simulation (Goebel and Katz, 2008).

	Ion Acoustic Wave	Optimized Grid Layout
Specific Impulse (s)	16,854	16,848
Change of Momentum kg m/s	1.66e-17	1.67e-17
Thrust (mN)	5	5
Ions Impacting on Extraction Grid (%)	19.7	19.7

Table 6.13: Table showing a comparison of the results produced when introducing an ion acoustic wave into the plasma and the results produced when using the optimized grid configuration

A comparison of the results produced during this simulation run and the results produced by the optimised grid layout is shown in Table 6.13.

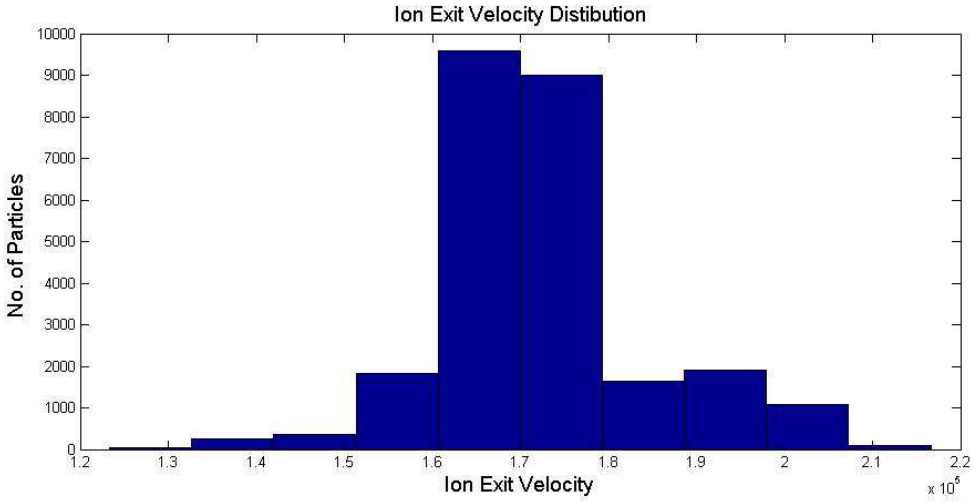

Figure 6.21: Histogram showing the distribution of particle exit velocities, in real units, when an ion acoustic wave was propagated through the plasma inside the ion thruster

It can be seen when comparing the particle exit velocity distributions shown in Fig. 6.19 and Fig. 6.21 that the inclusion of a wave in the ion thruster system produces no significant changes in terms of ion exit velocity when compared to the optimised three grid configuration discussed earlier. There were also no differences found in terms of change in ion momentum or beamlet focusing.

The results show no effect arising from the introduction of an ion acoustic wave within the discharge chamber. This lack of impact was unexpected, and may be due to the effects being very subtle, or due to assumptions made within the simulation hiding any effects that may have occurred. Other types of waves may produce a more obvious effect, either positive or negative, and although no benefits were found during this work this would be an interesting avenue of research to continue in the future. A full investigation of the concept of propagating waves though the discharge chamber would take significant modification of the simulation code, and will be considered for future work.

In this chapter the results obtained using the simulation code PICSIE have been presented. The following chapter will discuss these results, aiming to reach some conclusions on the original research questions.

7 Discussion

This chapter will discuss the results presented in the previous chapter. Conclusions will be presented on the configurations chosen for the two thrusters in order to produce two different specific impulses, a comparison of the performance of the two thrusters and a conclusion on whether the three grid or four grid thruster design should be the focus of research. A set voltage is then applied to the three grid configuration and a conclusion is reached on the most efficient grid configuration for that voltage profile.

7.1 Specific Impulse: 10,000s

7.1.1 Dual-Stage 4-Grid Simulation

The results produced during the simulation runs aiming to produce a specific impulse of 10,000s are shown in Section 7.1, with the results for the four grid thruster shown in Section 7.1.1.

In Fig.6.2 a reduction then sudden sharp increase can be seen in the change in ion momentum for the four grid case, with the sudden increase corresponding with a small increase in specific impulse. This shows that as the total applied voltage increases from 5500V to 6300V the number of ions impacting on the extraction grid decreases while the specific impulse increases steadily. When the total applied voltage reaches 6300V the specific impulse increases slightly while the number of ions impacting on the grid increases dramatically. However at higher voltages, while the specific impulse continues to gradually increase, the number of ions impacting on the extraction grid decreases. This suggests that a total accelerating voltage of 6300V should be avoided for this grid configuration as it may result in high erosion levels on the extraction grid.

It can be seen in Fig.6.4 that the number of ions colliding with the extraction grid remains the same for runs no.3 and no.4 (a description of the parameters used for each simulation run can be found in Table 6.3); this suggests that the large screen grid aperture results in such poor beam collimation that even a larger extraction grid aperture could not make a difference to the number of ions impacting on this grid.

The results produced by PICSIE were analysed and the most efficient voltage profile and accelerating grid layout were found. The aim of this was to achieve the required specific impulse (10,000s) with high power efficiency and good focusing of the ion beam. Poor focusing results in loss of thrust and ions in the plume can impact on the outer parts of the spacecraft causing damage, therefore minimal ion beam divergence is required (Goebel and Katz, 2008).

Parameter	Chosen Value
Screen Grid Voltage	5900V
Extraction Grid Voltage	3900V
Acceleration Grid Voltage	-100V
Deceleration Grid Voltage	0V
Aperture diameter - Screen/Others	1mm/0.7mm
Grid Thicknesses	Screen grid: 0.5mm, Others:2mm
Grid Spacings - Gap1/Gap2/Gap3	0.5mm/2mm/1mm

Table 7.1: Table showing the parameters chosen to provide the most efficient performance for the 4 grid thruster while producing a target specific impulse of 10,000s

An acceleration grid voltage of -100V was chosen along with a drop of 2000V in the extraction stage. It can be seen in Fig.6.3 that this was the configuration for Run No.2 (described in Table 6.2) and resulted in the highest specific impulse. Although Run No.3 (with an acceleration grid voltage of -150V) produced a higher change in ion momentum, there was a reduction in specific impulse compared to Run No.2. The aperture diameters were chosen to be 1mm for the Screen Grid and 0.7mm for the other grids; this corresponds to Run No.2 in Fig.6.4. It can be seen that although these parameters produce a slightly lower specific impulse when compared to the other runs (described in Table 6.3) it also resulted in the lowest number of ions impacting on the extraction grid, showing that these aperture diameters resulted in the highest degree of beam collimation. Having a higher degree of beam collimation reduces barrel erosion within the grid apertures, resulting in increased thruster lifetime; these aperture diameters were chosen because they produced a degree of beam collimation which would have the least impact on thruster lifetime.

7.1.2 Dual-Stage 3-Grid Simulation

The results for the three grid version of PICSIE aiming to produce a specific impulse of 10,000s can be seen in Section 6.1.2. It can be seen in Fig.6.7 that a saturation level seems to be reached on the amount of particles impacting on the extraction grid at a total applied voltage of 7000V suggesting that increasing voltage above this point does not reduce beam collimation at the first grid, while a slight drop is seen at 8000V. Further simulation runs would be needed to discover whether this saturation effect is found with all grid configurations and initial starting voltages. A linear increase can be seen in the specific impulse as the total applied voltage is increased.

The results produced by PICSIE were analysed with the aim of achieving a balance between high specific impulse, high thrust, high power efficiency and low ion impaction on the grids, finding the most efficient voltage profile and accelerating grid layout were found to achieve a target specific impulse of 10,000s.

Parameter	Chosen Value
Screen Grid Voltage	6000V
Extraction Grid Voltage	5000V
Acceleration Grid Voltage	-100V
Aperture diameter	1mm/0.7mm
Grid Thicknesses	Screen grid: 0.5mm, Others:2mm
Grid Spacings - Gap1/Gap2	0.5mm/2.5mm

Table 7.2: Table showing the parameters chosen to provide the most efficient performance for the 3 grid thruster while producing a target specific impulse of 10,000s

An extraction stage voltage drop of 1000V was found to produce the required specific impulse while maintaining a good degree of ion beamlet collimation, therefore keeping barrel erosion to a minimum. This will help extend the lifetime of the thruster by reducing the widening of grid apertures. The grid apertures were chosen to be the same as for the four grid case, as the same pattern of results was found when manipulating the aperture diameter. An acceleration stage gap of 2.5mm was chosen, a value slightly higher than the 2mm chosen for the four grid design. This was due to the larger distance providing an increase in the average change in ion momentum without negatively impacting on the beam collimation.

7.2 Specific Impulse: 15,000s

7.2.1 Dual-Stage 4-Grid Simulation

The results from the simulation of the four grid thruster with parameters chosen with the aim of producing a specific impulse of 15,000s can be seen in Section 6.2.1.

It can be seen in Fig.6.9 that as the total applied voltage increases, the specific impulse increases while the number of ions impacting on the extraction grid decreases. Although this was not seen in the results for a specific impulse of 10,000s it is possible that there is a causal relationship, with the reduced specific impulse at lower voltages being a direct result of the large number of ions impacting on the extraction grid, or that the higher voltages result in a greater degree of beam collimation at the screen grid, resulting in fewer ions impacting on the extraction grid.

The results produced by PICSIE were analysed and the most efficient voltage profile and accelerating grid layout were found for a target specific impulse of 15,000s.

Parameter	Chosen Value
Screen Grid Voltage	9500V
Extraction Grid Voltage	8500V
Acceleration Grid Voltage	-200V
Deceleration Grid Voltage	0V
Aperture diameter	1mm/0.7mm
Grid Thicknesses	Screen grid: 0.5mm, Others:2mm
Grid Spacings - Gap1/Gap2/Gap3	0.5mm/2mm/1mm

Table 7.3: Table showing the parameters chosen to provide the most efficient performance for the 4 grid thruster while producing a target specific impulse of 15,000s

The grid aperture diameter in this case corresponds to that chosen for the 10,000s case. This is because the same effects were seen when manipulating the aperture diameter, and maintaining a good degree of beam collimation is an important aspect for achieving efficient thruster performance without compromising potential lifetime. The same grid spacings were also chosen in this case, suggesting that it is the applied voltage that needs to vary to achieve a certain specific impulse while the thruster configuration remains efficient for a range of applied voltages and resulting specific impulses. A deceleration grid voltage of -200V was chosen, a lower value than that chosen for the 10,000s case; this was found to maintain a good degree of beam collimation without negatively impacting on the resulting thrust and specific impulse.

7.2.2 Dual-Stage 3-Grid Simulation

The results from the simulation of the three grid thruster aiming to produce a specific impulse of 15,000s can be seen in Section 6.2.2. The correlation between specific impulse and change in ion momentum seen in previous results can also be seen in Fig.6.12. In Fig.6.13 a steady increase in specific impulse can be seen as the applied voltage is increased, while the number of ions impacting on the extraction grid varies. However the amount of impacting ions is varying by only around 0.5%, as the scale on the right hand side of Fig.6.13 indicate that this plot shows a zoomed in view of the results. These results would appear as a fairly straight line with a slightly negative gradient when viewed on a larger scale. This corresponds to results seen in Fig.6.9, although to a lesser degree.

The results produced by PICSIE were analysed and the most efficient voltage profile and accelerating grid layout were found to produce a target specific impulse of 15,000s.

Parameter	Chosen Value
Screen Grid Voltage	10,000V
Extraction Grid Voltage	9000V
Acceleration Grid Voltage	-100V
Aperture diameter	1mm/0.7mm
Grid Thicknesses	Screen grid: 0.5mm, Others:2mm
Grid Spacings - Gap1/Gap2	0.5mm/2.5mm

Table 7.4: Table showing the parameters chosen to provide the most efficient performance for the 3 grid thruster while producing a specific impulse of 15,000s

A total applied voltage of 10,000V was found to produce the required specific impulse of 15,000s. An acceleration stage gap of 2.5mm was chosen; it can be seen in Figure 6.16 that the number of ions impacting on the grid remained stable for an acceleration stage gap of 1.5mm or larger up to a gap of 2.5mm while the specific impulse produced in the simulation increased with the size of the gap. Therefore the gap of 2.5mm was chosen to produce the maximum possible specific impulse without an increase in the number of impacting particles. In Figure 6.17 a sharp increase in the number of ions impacting on the extraction grid can be seen when the extraction grid and acceleration grid have diameters of 1mm, therefore this grid thickness should be avoided. Thicknesses of 2mm were chosen in order to produce a high specific impulse and change in ion momentum (as shown in Figure 6.18) while limiting the increase in the number of particles impacting on the extraction grid.

7.3 Comparison of the 3 and 4 Grid Thrusters Simulation Results

For a desired specific impulse of 10,000s a comparison of the chosen thruster parameters and simulation results is shown in the table below.

Parameter	**Simulated DS4G**	**Simulated DS3G**
Screen Grid Voltage	5900V	6000V
Extraction Grid Voltage	3900V	5000V
Acceleration Grid Voltage	-100V	-100V
Aperture Diameter	1mm/0.7mm	1mm/0.7mm
Grid Spacings	0.5mm/2mm/1mm	0.5mm/2mm
Grid Thickness	0.5mm/2mm	0.5mm/2mm
Parameter	**DS4G Simulation Result**	**DS3G Simulation Result**
Specific Impulse (s)	10,280	10,183
Thrust (mN)	3	3
Power Efficiency	0.426	0.43
Change in Ion Momentum (kg m/s)	4.02e-18	9.97e-18

Table 7.5: Table showing a comparison between applied voltages, grid configuration and simulation results for the 3 and 4 grid versions of PICSIE aiming to produce a specific impulse of 10,000s

It can be seen in Table 7.5 that the simulated three and four grid thrusters employ a slightly different voltage profile; this can also be seen in 7.1. The total applied voltage is slightly greater (100V greater) in the three grid case, and the four grid case uses an extraction stage drop of 2000V while the three grid case uses a drop of 1000V. This shows

that including the fourth grid in the thruster design means that a greater drop in voltage in the extraction stage is required to achieve the same specific impulse. This implies that the three grid design is more efficient, requiring a more gentle potential gradient in order to produce the same results. However, applying a more gentle potential gradient to the extraction stage could have an impact on erosion patterns, which would be an interesting area for further study. An acceleration voltage of -100V was found to produce the best performance in both cases in terms of maximum thrust, high power efficiency and a good degree of beam focusing. The same aperture diameters, grid thicknesses and grid spacings are used for both cases. The most striking difference between the three grid and four grid cases are the change in ion momentum produced in the simulation; this is significantly higher in the three grid case; there is no obvious reason for this difference, and further study in this area would be beneficial to fully understand the consequences of the high average change in ion momentum.

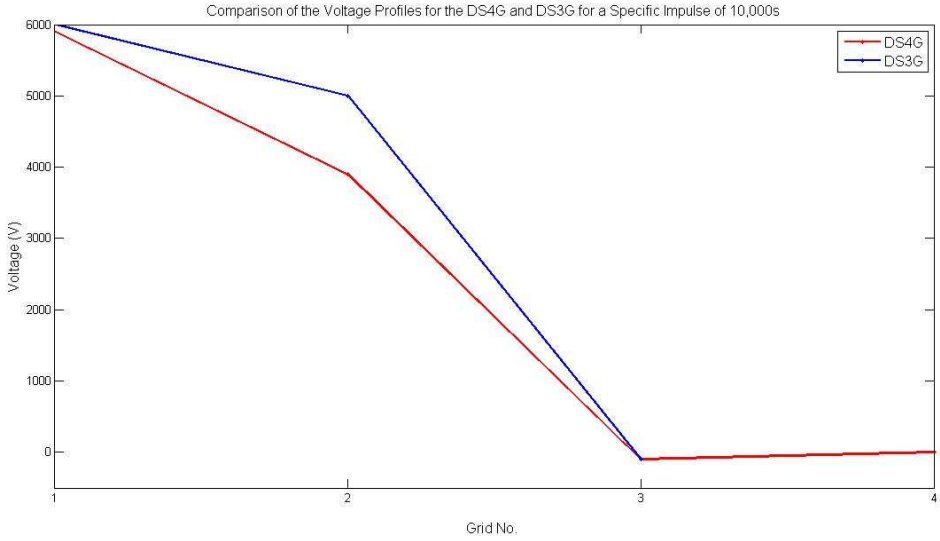

Figure 7.1: Figure showing the voltage profiles for the DS4G and DS3G to produce a specific impulse of 10,000s

The specific impulses produced in both cases were close to the desired specific impulse of 10,000s; the four grid simulation produced a specific impulse of 10,280s while the three grid simulation produced 10,183s and both cases produced a total thrust of 3mN. The power efficiency was slightly higher in the three grid case, 0.43 compared with 0.426, but the main difference between the two cases was the change in ion momentum produced by PICSIE. The four grid case produced a change in momentum of 4.02e-18 kg m/s while the three grid case produced a change in momentum of 9.97e-18 kg m/s, providing a significant improvement (almost 150%) over the four grid case.

For a desired specific impulse of 15,000s a comparison of the chosen thruster parameters and simulation results is shown in the table below.

Parameter	DS4G Chosen Value	DS3G Chosen Value
Screen Grid Voltage	9,000V	10,000V
Extraction Grid Voltage	8,000V	9,000V
Acceleration Grid Voltage	-200V	-100V
Aperture Diameter	1mm/0.7mm	1mm/0.7mm
Grid Spacings	0.5mm/2mm/1mm	0.5mm/2.5mm
Grid Thickness	0.5mm/2mm	0.5mm/2mm
Parameter	**DS4G Simulation Result**	**DS3G Simulation Result**
Specific Impulse (s)	15,252	15,103
Thrust (mN)	4.5	4.4
Power Efficiency	0.544	0.557
Change in Ion Momentum (kg m/s)	6.01e-18	1.49e-17

Table 7.6: Table showing a comparison between applied voltages, grid configuration and simulation results for the 3 and 4 grid versions of PICSIE aiming to produce a specific impulse of 15,000s

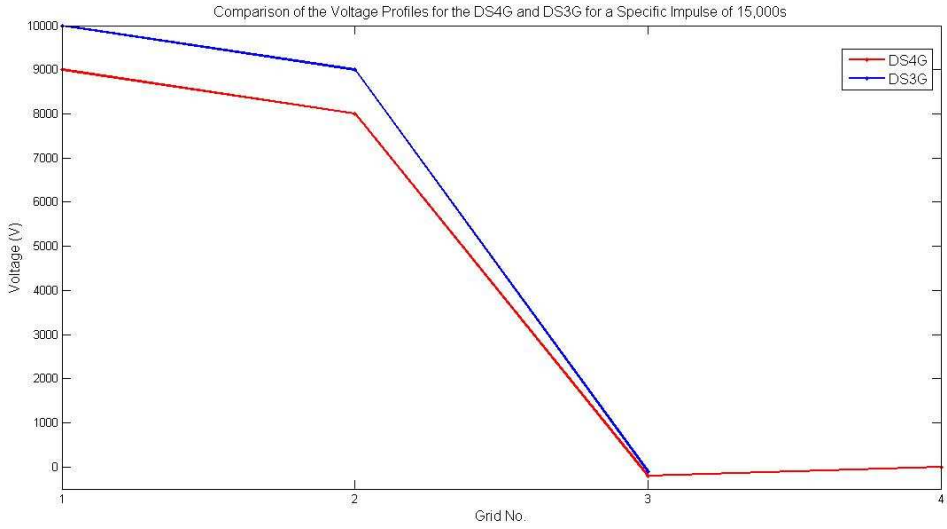

Figure 7.2: Figure showing the voltage profiles for the DS4G and DS3G to produce a specific impulse of 15,000s

For a desired specific impulse of 15,000s, the most efficient grid configuration and voltage profile and key simulation results are shown in Table 7.6. It can be seen that the three grid case employs a total applied voltage that is 1000V greater than that employed in the four grid case, as can be seen in Fig. 7.2, while both configurations have a drop of 1000V in the extraction stage and have a voltage difference of only 100V at the acceleration grid. The aperture diameters and accelerating grid thicknesses are the same in both cases. For the four grid layout the grid spacings are the same as for the 10,000s case shown in Table 7.5, however for the three grid case an acceleration stage gap of 2.5mm is employed for a specific impulse of 15,000s, compared with a gap of 2mm for a specific impulse of 10,000s.

From Table 7.6 it can be seen that

- The specific impulses produced by the three and four grid layouts are close to the

required specific impulse of 15,000s; the four grid layout produced a specific impulse of 15,252s and the three grid layout produced a specific impulse of 15,103s

- The thrust produced by the four grid case is slightly higher than that produced by the three grid case, 4.5mN compared to 4.4mN
- The power efficiency is slightly higher for the three grid layout, 0.557 compared to 0.544 for the four grid layout

As for the case of a target specific impulse of 10,000s, the major difference between the three and four grid layouts is the change in ion momentum produced. The four grid layout produces a change in momentum of $6.01e^{-18}$ kg m/s, while the three grid layout produces a much higher value of $1.49e^{-17}$ kg m/s. It can be assumed that the lower change in momentum in the four grid case is due to the deceleration grid; while aiming to reduce erosion of the thruster the fourth grid also results in a decreased ion momentum when compared to that achieved without the deceleration grid.

Comparing the three and four grid results for the specific impulses of 10,000s and 15,000s, it can be seen that for both cases the three grid layout requires a slightly higher applied voltage to produce the required specific impulse. The two grid layouts are identical for both cases, with the exception being a larger acceleration stage gap of 2.5mm is employed for the three grid thruster in the 15,000s case. Increasing the acceleration stage gap by 0.5mm may have an impact on the erosion patterns within the thruster, possibly altering the potential lifetime of the thruster. In future research the changes in erosion patterns should be studied to ensure that the larger acceleration gap would not have a negative impact on thruster lifetime.

It can be seen from Tables 6.5.and 6.6 that in order to produce the lower specific impulse of 10,000s the four grid design needs a stronger potential gradient in the extraction stange, while this is not needed in the 15,000s case. The potential gradient would have an effect on the erosion patterns in the area and downstream of the extraction stage, and this should be studied further before a conclusion can be reached on which scenario produces better results in terms of both efficiency and erosion. This would only be an issue for missions requiring a specific impulse lower than 15,000s, as it can be seen that this difference between the thruster designs is not apparent for the higher specific impulse.

In both specific impulse cases the three grid layout produces a slightly better power efficiency; however the differences between the power efficiency values are small and may not impact on a choice between the two thrusters. The major difference between the three and four grid layouts in both specific impulse cases is the change in ion momentum produced by PICSIE. The change in momentum produced by the three grid layout is significantly higher than that produced by the four grid layout, which would be a significant factor when it came to deciding between the two layouts for a mission. It is clear that removing the fourth grid has a major impact on the change in momentum of the ions within the

simulation; however the reasons for this making such a large difference to the result are not clear and should be studied further.

This chapter has provided a discussion of the results presented in the previous chapter. The conclusions reached during this work will be presented in the following chapter.

7.4 Optimization of the DS3G Configuration

The results from the simulation runs aiming to find an optimized configuration for the three grid thruster while using a set voltage profile can be seen in Section 6.3.

Fig.6.14 shows a drop of around 8% in the number of ions impacting on the extraction grid as the extraction stage gap is increased and displays a negative correlation between the specific impulse and the number of ions impacting on the grid. It can be seen that a larger spacing between the screen grid and extraction grid provides better results in terms of a high specific impulse, high change in ion momentum and low ion impaction on the extraction grid, as did a spacing of 2.5mm between the extraction grid and acceleration grid.

It can be seen in Fig.6.17 and Fig.6.18 that grid diameters of 2mm for the extraction grid and acceleration grid provides a compromise between obtaining a high specific impulse and change in ion momentum while restricting the amount of simulation ions impacting on the extraction grid. Figs 6.14 and 6.15 show clear benefits in terms of increased specific impulse, change in ion momentum and reduced ion impaction on the extraction grid as the extraction stage and acceleration stage gaps are increased. A maximum extraction stage gap of 1mm and a maximum acceleration stage gap of 2.7mm were simulated. It has been stated that the distance between the first two grids should be less than the diameter of the screen grid apertures to maximise perveance, which is the amount of current that the accelerator grids can extract and focus into the ion beam for a given applied voltage (Goebel and Katz, 2008). Therefore an extraction stage gap of 0.7mm was chosen, to allow for widening of the screen grid apertures through erosion.

A peak in the graph showing the simulation ions impacting on the extraction grid at a diameter of 1.25mm can be seen in Fig.6.17. This is an unexpected value although it may be due to natural variation and the change is made more obvious due to the scale used on the plot.

The results originally presented in the previous chapter have been discussed above; the chosen configuration parameters for the two thruster designs have been presented, chosen in order to produce two specific impulses. The two designs have been compared, and a conclusion has been reached on whether the fourth grid provides benefits in terms of thruster performance compared to the three grid design. An optimized configuration for the three grid design has been presented for a given applied voltage. The conclusions

reached during this work will be summarized in the following chapter.

8 Conclusions

The conclusions reached during this work are presented in this chapter. The first conclusion reached in this work is that the code developed produced consistent results when compared with test data and results (see Section 5.8) and could be utilized as a design tool for the study of ion engine performance.

The three and four grid thrusters were simulated with the aim of producing specific impulses of 10,000s and 15,000s, chosen as values likely to be design requirements of space missions in the future for different purposes. The requirement for the design of the thrusters for the BepiColombo mission was to achieve a specific impulse of 4300s (Benkhoff *et.al.*, 2010) and it is expected that higher specific impulses will be required for future missions. The accelerating grids layout and applied voltage profiles were varied in PICSIE and the parameters chosen from the results of these simulations are presented in Table 6.5, Table 6.7, Table 6.10 and Table 6.12. The simulation results indicate that a large screen grid aperture results in such poor beam collimation that even a larger extraction grid aperture could not reduce the number of ions impacting on the grid, and that for the three grid case a saturation level seems to be reached on the amount of particles impacting on the extraction grid at a total applied voltage of 7000V, suggesting that increasing voltage above this point does not reduce beam collimation at the first grid.

It has been suggested (see Section 4) that the use of the fourth grid in the dual stage thruster is not necessary. Its main function is to shield the thruster from backstreaming CEX ions, and while this can increase the lifetime of the thruster it also greatly increases its complexity in terms of construction and hence its reliability as it provides one more part that has the potential to fail. Once the most efficient parameters for the two desired specific impulses had been found, the three and four grid cases for each specific impulse were compared; the results of this comparison can be found in Tables 7.5 and 7.6. The results indicate that an acceleration grid voltage of -100V produces the best performance for both the three grid and four grid thrusters, in terms of maximum thrust, high power efficiency and a good degree of beam focusing.

The input and output parameters were similar for the three and four grid layouts for both specific impulse cases, with the major exception being the change in ion momentum produced by the simulations. In both the 10,000s and 15,000s case the change in momentum produced was significantly higher (over 100% higher) for the three grid layout than for the four grid layout, as shown in Tables 7.5 and 7.6; a reduction in ion momentum was an unexpected result of including the fourth grid in the thruster.

The inclusion of the fourth grid in the thruster produces no apparent advantages to the thruster when the backstreaming of CEX ions was disregarded and actually results in a significantly lower change in ion momentum being produced by the thruster, as shown in Tables 7.5 and 7.6. Hence the conclusion of this work is that the fourth grid should

not be included in the dual stage thruster system, unless a very long lifetime is required and it is expected that a three grid thruster could not fulfil this requirement. In order to discover the expected lifetime extension as a result of including the fourth grid, CEX ions would need to be included in PICSIE; this is discussed in Section 9 as possible further work.

A set voltage profile was then applied to the three grid layout, and the grid configuration was manipulated to find the most efficient layout in terms of producing a high specific impulse, thrust and change in ion momentum while maximising ion beamlet focusing (and therefore minimizing erosion of the grids as a result of ions impact), as described in Section 6.3. Results of this optimization can be found in Table 6.10; the results indicate that the maximum specific impulse that can be achieved with this chosen voltage profile without increasing erosion rates is 17,280s. The results also show that increasing the extraction stage gap results in a drop in the number of ions impacting on the extraction grid, and a negative correlation can be seen between the specific impulse and the number of ions impacting on the grid.

It was thought that propagating a wave through the plasma within the ion thruster could result in improved performance; firstly the potentials applied to the accelerating grids were oscillated. No improvement was observed in performance of the thruster, as can be seen in Section 6.4.1; no significant changes in performance parameters were apparent, with specific impulse, thrust, change in ion momentum and beamlet focusing remaining very close to those produced by the optimised grid configuration presented earlier.

Secondly an ion acoustic wave was simulated in the centre of the accelerator grid apertures, as described in Section 6.4.2. As for the oscillating grid potentials no improvement in performance parameters was observed; specific impulse, thrust, change in ion momentum and beamlet focusing remained very close to those produced by the optimised grid configuration presented earlier.

The lack of change in the performance parameters observed after introducing waves into the discharge chamber plasma was unexpected. This may be due to the effects being very subtle, or hidden by assumptions made in the simulation. It is possible that other types of waves may have a more noticeable effect.

This chapter has discussed the conclusions reached during this work. The following chapter will discuss some potential areas for future work, leading from the conclusions reached during this research and from some interesting results obtained from the simulation code that couldn't be investigated further due to time constraints.

9 Further Work

This chapter will discuss some possible areas for future work, including extending the simulation code PICSIE and examining in more detail some interesting results that were produced by the simulation code.

A major cause of reduced lifetime in ion thrusters is widening of the grid apertures due to CEX ions. A potential next stage in this research would be to extend PICSIE to include these CEX ions, in order to attempt to predict the total expected lifetime of the ion thruster. As the expected lifetime of the thruster would play a key role when choosing a thruster for a potential space mission it would be important to know that the thruster design could fulfil potential lifetime requirements. Extending the simulation domain to include the entire discharge chamber of the thruster when studying erosion would provide more insight into erosion and its consequences. Sputtering taking place within the discharge chamber can affect other areas of the thruster, allowing sputtered material to build up in areas where it may have negative consequences. Producing a simulation of the entire discharge chamber area would allow the flow of sputtered material to be examined, analysing the benefits of the materials recommended to reduce sputtering and finding methods to reduce the erosion process.

Alternatively the code could be extended to simulate two or more apertures in two dimensions, allowing the interaction of the individual ion beamlets to be studied. The interaction between ion beamlets could alter performance of the thruster, and engineering the thruster design in order to minimize the negative impacts of ion beam interaction would play an important role in designing an efficient engine.

PICSIE is currently being used by two undergraduate students in the Engineering department at Sussex University as a research tool. The students will be adapting the code to fit their own research aims of studying material performance at boundaries and plume collimation to improve specific impulse.

Some of the results presented in this work may have consequences that were not apparent when using the simulation code PICSIE. When manipulating the two thruster designs with the aim of producing a specific impulse of 10,000s it was found that the three grid design required a more gentle potential gradient in the acceleration stage compared to the four grid design in order to produce the same specific impulse. The differences in potential gradient in the area may have an impact on erosion, both from ions leaving the ion beam to impact on the grids and from backstreaming ions. The apparent efficiency of the three grid design in this case may actually result in increased erosion within the thruster, or alternatively may result in reduced erosion within the thruster. All aspects of a design choice should be studied before a firm conclusion is reached, so this would be an interesting area for further study.

A similar issue arises in the 15,000s specific impulse case; it can be seen in Table 7.6 that a slightly larger acceleration stage gap of 2.5mm is used in the three grid case, compared to a gap of 2mm in the four grid case. A 25% increase in the acceleration stage gap compared to the four grid case could have significant impact on erosion patterns, particularly in terms of ions escaping the ion beam and impacting on the grids, resulting in potential barrel erosion. It is clear that investigation of erosion patterns would be a key area for future work, as it is possible that decisions made during this research could have an impact on erosion rates and therefore potential lifetime of the thruster.

One of the main differences between the two thruster designs was the change in ion momentum produced by the thrusters, with the change in ion momentum being significantly higher in the three grid case compared to the four grid case. The reasons for this difference in performance are not clear and this would be an interesting area for further study.

The concept of introducing waves into the plasma within the discharge chamber was studied briefly. No apparent benefits were found, although it is possible that there were subtle effects that went unnoticed or that assumptions made within the simulation code hid any potential effects. The lack of impact of propagating waves through the discharge chamber was unexpected, so it is possible that investigating this concept in more detail would make it possible to utilize this concept in order to improve the performance of all gridded ion thrusters. There are many types of waves that could be investigated, and it is possible that although the two wave types investigated in this work did not show any effect another type of wave may have a more dramatic impact on thruster performance. This would be a major area of work, with the physical interaction between the motion of the waves and the particles within the thruster having potentially unexpected consequences in other areas, for example impacts on erosion rates and thruster lifetime or altering the interaction between the ion beamlets and within the thruster plume. The simulation code would need to be greatly extended in order to study this in detail.

In Figure 6.2 a sharp increase in the number of ions impacting on the extraction grid can be seen at a voltage of 6300V. The reasons for this striking increase are not clear, therefore running a number of simulations with voltages around 6300V to get a clearer understanding of what is occurring at this point would be beneficial. This increase in the number of ions impacting on the grid could result in increased erosion, leading to a potentially reduced lifetime. Therefore it would be useful to study this in more detail and reach a conclusion on whether this particular grid configuration and voltage profile should be avoided due to the reduced collimation of the ion beamlet leading to increased ion impaction on the extraction grid.

This chapter has suggested several potential research areas for future work. It is clear that there are many areas of research into which this work could be extended, all complimenting this work in different ways.

References

Ad Astra Rocket Company (2009). http://www.adastrarocket.com. [Accessed May 2010]

Ahedo, E (2011). Plasmas for Space Propulsion. Plasma Physics and Controlled Fusion. 53(12).

ANU (2010). Dual Stage 4 Grid Thruster [online]. Available from: physics.anu.edu.au [Accessed October 2010]

Benkhoff, J., van Casteren, J., Hayakawa, H., Fujimoto, M., Laakso, H., Novara, M., Ferri, P. Middleton, H., and Ziethe, R. (2010). BepiColombo - Comprehensive exploration of Mercury: Mission overview and science goals. Planetary and Space Science. 58, pp 2-20.

Bering, E., Longmier, B., Squire, J., Glover, T., Cassady, L., Ilin, A., Carter, M., Olsen, C., McCaskill, G. and Chang Diaz, F. (2010). Performance Measurements and Technology Demonstration of the VASIMR VX-200. In: AIAA (American Institute of Aeronautics and Astronautics), AIAA Space 2010 Conference and Exposition, California, August 30 – September 2 2010.

Birdsall, C. and Langdon, A. (1985). Plasma Physics Via Computer Simulation. Bristol: IOP Publishing Ltd

Boyd, I. (2011). Simulation of Electric Propulsion Thrusters. Available from: http://ftp.rta.nato.int. [June 2010]

Bramanti, C. and Walker, R. (2006), Single Aperture Four Electrode (SAFE/DS4G) Thruster Executive Summary. Available from http://esamultimedia.esa.int [Accessed March 2011]

Bramanti, C., Walker, R., Sutherland, O., Boswell, R., Charles, C., Fearn, D., Gonzalez Del Amo, J., and Orlandi, M. (2006). The Innovative Dual-Stage 4-Grid Ion Thruster Concept – Theory and Experimental Results. Available from: http://www.esa.int. [Accessed May 2011]

Bramanti, C., Izzo, D., Samaracc, T., Walker, R., and Fearn, D. (2009). Very High delta-V Missions to the Edge of the Solar System and Beyond Enabled by the Dual-Stage 4-Grid Ion Thruster Concept. Available from: http://www.esa.int. [Accessed May 2011]

Breizman, B. and Arefiev, A. (2004). Theoretical Components of the VASIMR Plasma Propulsion Concept. Physics of Plasmas, 5(11). pp 2942-2949.

Brieda, L. (2010). Simple Particle in Cell Code in Matlab. Available from:

http://www.particleincell.com. [Accessed June 2011]

Brophy, J. (2002). NASA's Deep Space 1 ion engine. Review of Scientific Instruments. 73. 1071-1078

Callen, J. (2006). Fundamentals of Plasma Physics. 3rd edition. Springer-Verlag New York.

Cassady, L., Longmier, B., Olsen, C., Ballenger, M., McCaskill, G., Ilin, A., Carter, M., Glover, T., Squire, J. and Chang Diaz, F. (2010). VASIMR Performance Results. In: AIAA (American Institute of Aeronautics and Astronautics), 46th AIAA/ASME/SAE/ASEE Joint Propulsion Conference & Exhibit, Tennessee, 25-28 July 2010

Chang, L., Haibin, T., Zhenpeng, Z., Zuo, G., and Yu, L. (2008). Estimate of Lifetime of Ion Thruster Optics Based on Particle Simulation. Plasma Science and Technology 10. Available from: iopscience.iop.org [Accessed June 2010]

Charles, C (2009). Plasmas for Spacecraft Propulsions. Journal of Physics D: Applied Physics. 42(16)

Charles, C., West, D., and Boswell, R. (2008). Testing a Helicon Double Layer Thruster Immersed in a Space-Simulation Chamber. Available from: arc.aiaa.org [Accessed March 2012]

Coletti, M., Gessini, M. and Gabriel, S. (2010). A 4-Gridded Ion Engine for High Impulse Mission. Space Propulsion 2010, San Sebastian, Spain, 2010

Coletti, M. and Gabriel, S. (2010). Design of a Dual Stage Ion Engine for the Hiper Project. AIAA 46th Joint Propulsion Conference, Nashville, July 2010

Coletti, M. and Gabriel, S. (2012). The Applicability of Dual Stage Ion Optics to Ion Engines for High Power Missions. IEEE Transactions on Plasma Scence, 40,4 (April 2012)

Edwards, C., Wallace, N., Tato, C. and van Put, P. (2004). The T5 Ion Propulsion Assembly for Drag Compensation on GOCE. Proc. Second International GOCE User Workshop 'GOCE, the Geoid and Oceanography. March 2004.

ESA (2004). Electric Spacecraft Propulsion - Hall Effect Thrusters [online]. Available from: www.esa.int [Accessed March 2012]

ESA (2006). Dual-Stage Gridded Ion Thruster (DS4G) [online]. Available from: www.esa.int [Accessed May 2010]

ESA (2009). ESA Designs its Smallest Ever Space Engine to Push Back Against Sunshine [online]. Available from: www.esa.int [Accessed May 2011]

ESA (2009a). SMART-1 [online]. Available from: www.esa.int [Accessed May 2010]

ESA (2012). GOCE [online]. Available from: www.esa.int [Accessed September 2012]

ESA (2012a). BepiColombo [online]. Available from: www.esa.int [Accessed June 2013]

ESA (2012b). LISA Pathfinder Overview [online]. Available from: www.esa.int [Accessed June 2013]

Estublier, D., Saccoccia, G. and Gonzales del Amo, J. (2007). Electric Propulsion on SMART-1. ESA Bulletin 129.

Estublier, D (2008). The SMART-1 Spacecraft Potential Investigations. IEEE Transactions on Plasma Science. 36 (5). 2262-2270.

FAR-TECH Inc (2012). http://www.far-tech.com. [Accessed May 30th 2011]

Farnell, C., Williams, J. and Wilbur, P. (2003). Numerical Simulation of Ion Thruster Optics. 29th International Electric Propulsion Conference, Toulouse, France, 2003.

García-Rosales, C., Eckstein, W. and Roth, J. (1994). Revised Formulae for Sputtering Data. Journal of Nuclear Materials. 218, pp8-17.

Glover, T., Chang Diaz, F., Squire, J., Jacobson, V., Chavers, D. and Carter, M. (2005). Principal VASIMR Results and Present Objectives. In: American Institute of Physics, Space Technology and Applications International Forum – STAIF 2005.

Goebel, D (2005). High Voltage Breakdown Limits of Molybdenum and Carbon-based Grids for Ion Thrusters. Available from http://trs-new.jpl.nasa.gov [Accessed May 16th 2011]

Goebel, D and Katz, I (2008). Fundamentals of Electric Propulsion: Ion and Hall Thrusters. NASA JPL Space and Technology Series, 2008.

Hamilton, C (2009). Galileo Project [online]. Available from: www.fukuoka-edu.ac.jp [Accessed March 2010]

Hayakawa, Y (2007). Current Distribution on a Two Grid Ion Extraction System Gridlet.

Journal of Propulsion and Power. 23. pp 1279-1284

JAXA (2010). Asteroid Explorer 'Hayabusa' (MUSES-C) [online]. Available from: www.jaxa.jp [Accessed September 2010]

Kivelson, M. and Russel, C. eds. (1995). Introduction to Space Physics. Cambridge: Cambridge University Press

Kubota, K (2009). Comparison of Simulated Plasma Flow Field in a Two Dimensional Magnetoplasmadynamic Thruster with Experimental Data. IEEE Transactions on Plasma Science. 12(37).

Kuninaka, H (2008). Microwave Discharge Ion Engines aboard Hayabusa Asteroid Explorer. Beamed Energy Propulsion, Fifth International Symposium. 572-581

LeVeque, R. (2007). Finite Difference Methods for Ordinary and Partial Differential Equations. USA: Society for Industrial and Applied Mathematics.

Longmier, B., Bering, E., Ballenger, M., Olsen, C., Squire, J. and Chang Diaz, F. (2011). Performance Studies of the VASIMR VX-200. In: AIAA (American Institute of Aeronautics and Astronautics), 49th AIAA Aerospace Sciences Meeting and Exhibit, Florida, 4-7 January 2011.

Marcuccio, S., Genovese, A., Andrenucci, M., Saccoccia, G. and Gonzales del Amo, J. (1997). FEEP Thrusters Applications to Constellations and Small Satellites. Spacecraft Guidance, Navigation and Control Systems, Proceedings of the 3rd ESA International Conference held 26-29 November, 1996 at ESTEC, Noordwijk, the Netherlands. p.689

Martinex-Sanchez and Pollard (1998). Spacecraft Electric Propulsion – an Overview. Journal of Propulsion and Power. 14(5).

McNamara, P. (2009). Overview of LISA Pathfinder. Available from: lisa.nasa.org [Accessed June 2010]

Miyasaka, T., Kobayashi, T. and Asato, K. (2010). Characteristics of Ions Impacting Grid Surfaces in an Ion Engine. Vacuum. 85: 585-590. Available from: elsevier.com [Accessed May 31st 2011].

Nakano, M (2007). Three-Dimensional Simulations of Ion Engine Grid Erosion. Adv Appl Plasma Sci. 2007. 6:93-6.

NASA (2003). Propulsion Systems of the Future [online]. Available from: http://www.nasa.gov

[Accessed May 2010]

NASA (2004). Variable Specific Impulse Magnetoplasma Rocket [online]. Available from: spaceflight.nasa.gov [Accessed May 2010]

NASA (2008). Ion Propulsion [online]. Available from: http://www.nasa.gov [Accessed April 2010].

NASA (2010). Magnetoplasmadynamic Thrusters [online]. Available from: http://www.nasa.gov [Accessed May 2010]

NASA (2011). Dawn at a Glance [online]. Available from: Available from: http://www.nasa.gov [Accessed June 2011]

Ohara, Y (1978). Numerical Simulation for Design of a Twostage Acceleration System in a Megawatt Power Source. J. Appl. Phys. 49, 4711 (1978);

Oran, E., and Boris, J. (1987). Numerical Simulation of Reactive Flow. Cambridge: Cambridge University Press.

Patterson, M and Verhey, T (1990). 5kW Xenon Ion Thruster Lifetest. AIAA Paper No. 90-2543. Available from: http://arc.aiaa.org [Accessed May 2011]

Peng, X., Zhang, Q. and Keefer, D. (1993). Particle Simulation of Ion Optics and Grid Erosion for Two-Grid and Three-Grid Systems. Review of Scientific Instruments. 65(5). Available from: American Institute of Physics [Accessed May 31st 2011]

The Planetary Society (2010) http://www.planetary.org [Accessed April 2010]

Prado, M (2002). Transportation - of Earth, Lunar and Asteroidal Materials [online]. Available from: www.permanent.com [Accessed April 2010]

Pullins, S., Chiu, Y., Levandier, D., and Dressler, R. (2000). Ion Dynamics in Hall Effect and Ion Thrusters: Xe^+ + Xe Symmetric Charge Transfer. AIAA 2000-0603. Available from: arc.aiaa.org [Accessed May 2011]

Rawlin, V (1988). Internal Erosion Rates of a 10-kW Xenon Ion Thruster. Available from: www.archive.org [Accessed May 2011]

Rayman, M., Fraschetti, T., Raymond, C. and Russell, C. (2006). Dawn: A Mission in Development for Exploration of Main Belt Asteroids Vesta and Ceres. Acta Astronautica 58, pp605-616.

Rosenberg, D and Wehner, G (1962). Sputtering Yields for Low Energy He+, Kr+, and Xe+Ion Bombardment. Journal of Applied Physics. 33, 1842 (1962).

Scharlemann, C., Buldrini, N., Killinger, R., Jentsch, M., Polli, A., Ceruti, L., Serafini, L., DiCara, D. and Nicolini, D. (2011). Qualification Test Series of the Indium Needle FEEP Micropropulsion system for LISA Pathfinder. Acta Astronautica. 69(9). pp 822-832.

Shewchuk, J. (2002). What is a Good Linear Element? Interpolation, Conditioning and Quality Measures. Available from: http://www.cs.berkeley.edu [Accessed January 2014]

Smith, H (2006). Computational Studies of an Asymmetric RF Plasma using Particle-in-cell Techniques. Available from http://plasma.kulgun.net/HBS/ [Accessed January 2011]

Snyder, J., Goebel, D., Hofer, R. and Polk, J. (2010). Performance Evaluation of the T6 Ion Engine. 46th AIAA/ASME/SAE/ASEE Joint Propulsion Conference and Exhibit. July 2010.

Squire, J., Chang Diaz, F., Carter, M., Cassady, L., Chancery, W., Glover, T., Jacobson, V., McCaskill, G., Bengtson, R., Bering, E. and Deline, C. (2007). High Power Experiments using Deutrium, Neon and Argon. The 30th International Electric Propulsion Conference, Florence, Italy, 17-20 September 2007

Sun, A., Mao, G., Yang, J., Xia, G., Chen, M. and Huo, C. (2010). Particle Simulation of Three-Grid ECR Ion Thruster Optics and Erosion Prediction. Plasma Science and Technology. 12(2). Available from: IOPscience [Accessed May 31st 2011]

Szabo, B. and Babuska, I. (1991). Finite Element Analysis. USA: John Wiley and Sons.

Tartz, M., Hartmann, E. and Neumann, H. (2008) Validated Simulation of the Ion Extraction Grid Lifetime. Review of Scientific Instruments. 79. Available from: American Institute of Physics [Accessed 31st May 2011]

Tech-X Corporation (2012). http://www.txcorp.com. [Accessed May 30th 2011]

Walker, R., Izzo, D. and Fearn, D. (2006). Missions to the Edge of the Solar System Using a New Advanced Dual-Stage Gridded Ion Thruster with Very High Specific Impulse. Available from: http://www.esa.int. [Accessed May 2011]

Wang, J., Anderson, J. and Polk, J. (1998). Three-Dimensional Particle Simulations of Ion Optics Plasma Flow. Available from: The American Institute of Aeronautics and Astronautics [Accessed May 31st 2011]

Wang, J., Polk, J. and Brinza, D. (2003). Ion Thruster Modelling: Particle Simulations and Experimental Validations. Available from: American Institute of Physics [Accessed May 31st 2011]

Wang, J., Polk, J., Brophy, J. and Katz, I. (2003a). Three Dimensional Particle Simulations of NSTAR Ion Optics. Available from: erps.spacegrant.org [Accessed May 2011]

Wilbur, P., Rawlin, V. and Beattie, J. (1998). Ion Thruster Development Trends and Status in the United States. Journal of Propulsion and Power. 14(5).

Williams, J., Goebel, D., and Wilbur, P. (2003). Analytical Model of Electron Backstreaming for Ion Thrusters. AIAA 2003-4560. Available from: arc.aiaa.org [Accessed May 2011]

Yamamura, Y., Itikawa, Y., and Itoh, N. (1983). Angular Dependence of Sputtering Yields of Monatomic Solids. Available from: dpc.nifs.ac.jp [Accessed May 2011]

Zhong, L., Liu, Y., Wen, Z. and Ren, J. (2010a). Numerical Simulation of Ion Extraction Through Ion Thruster Optics. Plasma Science and Technology. 12(1). Available from: IOPscience [Accessed May 31st 2011]

Zhong, L., Liu, Y., Li, J., Gu, Z., Jiang, H., Wang, H. and Haibin, T. (2010b). Numerical Simulation of Characteristics of CEX Ions in Ion Thruster Optical System. Chinese Journal of Aeronautics. 23: 15-21. Available from: ScienceDirect [Accessed May 31st 2011]

Appendices

Appendix A - Conversion Factors

The conversion factors shown here were used in PICSIE to peform conversions between real units and computer units.

Time conversion factor:

$$T_{\mathbf{F}} = \frac{\omega_{p\mathbf{COMP}}}{\omega_p}$$

Thermal velocity conversion factor:

$$V_{th\mathbf{F}} = \frac{V_{th}}{V_{th\mathbf{COMP}}}$$

Drift velocity conversion factor:

$$V_{drift\mathbf{F}} = \frac{V_{drift}}{V_{drift\mathbf{COMP}}}$$

Length conversion factor:

$$L_{\mathbf{F}} = V_{th\mathbf{F}} * T_{\mathbf{F}}$$

Number density conversion factor:

$$N_{d\mathbf{F}} = \frac{N_d}{N_{d\mathbf{COMP}}}$$

Charge conversion factor:

$$Q_{\mathbf{F}} = \frac{q}{\frac{q_{macro}}{N_{d\mathbf{F}}}}$$

Mass conversion factor:

$$M_{\mathbf{F}} = \frac{M_i}{M_{\mathbf{COMP}}}$$

Energy conversion factor:

$$W_{\mathbf{F}} = M_{\mathbf{F}} * V_{th\mathbf{F}}^2$$

Potential conversion factor

$$\phi_{\mathbf{F}} = \frac{W_{\mathbf{F}}}{Q_{\mathbf{F}}}$$

Electric field intensity conversion factor

$$E_{\mathbf{F}} = \frac{\phi_{\mathbf{F}}}{L_{\mathbf{F}}}$$

Magnetic induction conversion factor

$$B_{\mathbf{F}} = \frac{M_{\mathbf{F}}}{T_{\mathbf{F}} * Q_{\mathbf{F}}}$$

Charge density conversion factor

$$\rho_{\mathbf{F}} = \frac{Q_{\mathbf{F}}}{L_{\mathbf{F}}}$$

Appendix B - Matlab Code

This section contains sample code for the PICSIE simulation, including the main code and the functions called within in.

Main code

```
%%%%%%%%%%%%%%%%%%%%%%%%%
%%ION THRUSTER PIC CODE%%%
%%Ellie Bramer%%
%%%%PICSIE%%%
%%%%%%%%%%%%%%%%%%%%%%%%%%%%%%%%%%


%Clear variables, close all figures
clear variables
close all

%Identify global variables needed for functions
global C Lx Ly M K vth v_drift Te N nx ny p np nnp insertp Vp Xp MomentumX MomentumY
Cden Rho phi EF it Optics1 Optics2 Optics3 Optics4 i j a b c d e f g h h1 h2 h3 h4
mp_q PhiO1 PhiO2 PhiO3 PhiO4 SW PCOUNT;



%%Simultion domain%%
nx = 26;                            %No. of nodes in x direction
ny = 10;                            %No. of nodes in y direction
N = nx*ny;                          %No. of nodes

%%Constants%%
RE0 = 8.854e-12;                    %Permittivity of a vacuum REAL
E0 = 1;                             %E0 COMPUTER
EPSI = 1;                           %EPSI = 1/E0
QE = 1.602e-19;                     %Elementary charge
Kb = 1.381e-23;                      %Boltzmann constant
AMU = 1.661e-27;                    %Atomic mass unit
Mi = 2.18024e-25;                   %Xenon ion mass (kg) REAL
Rqm = 7.14e5;                       %Charge to mass ratio of Xenon (q/m) REAL
QM = 1;                             %Charge to mass ratio COMPUTER
q = 5;                              %Charge of Xenon ion REAL

%Plasma parameters
n0 = 1.5e17;                        %Density in #/m^3 REAL
Te = 5;                             %Electron temperature in eV
T = 500;                            %Plasma temperature in K
Wc = 0;                             %As plasma is unmagnetised
```

```
%ST = 5.31*DL;                          %Sheath thickness
phiref = 10;                            %Reference potential REAL
Max = 200000;                           %Max no. of particles

%SCALING AND CONVERSION FACTORS%
%Wp and Time%
Wp = 1;                                 %Wp COMPUTER
RWp = sqrt(n0*q^2/RE0*Mi);              %Wp REAL
Tf = Wp/RWp;                            %Time CONVERSION FACTOR
%Velocity%
vthR = sqrt(Kb*Te/Mi);                  %Thermal velocity REAL
vth = 0.1;                              %Thermal velocity COMPUTER
Vthf = vthR/vth;                        %Thermal velocity CONVERSION FACTOR
v_drift = 4*vth;                       %V_drift COMPUTER
v_driftR = 7000;                        %V_drift REAL
v_driftF = v_driftR/v_drift;            %V_drift CONVERSION FACTOR
%Length%
lambdaD = 69*sqrt(T/n0);                %Debye length REAL
DL = vth/Wp;                            %Debye length COMPUTER
Lf = Vthf*Tf;                           %Length conversion factor
Fpe = Wp/(2*pi);
Tp = 1/Fpe;
%%%%%%%%%%%Simulation Domain, length, cell size, time%%%%%%%%%%%
C = 4*DL;                               %Cell size
dx = 4*DL;
Lx = (nx-1)*C;                          %Domain length in x direction
Ly = (ny-1)*C;                          %Domain length in y direction
dt =  0.5;                              %Time step
ts = 500;                               %No. of time steps
%%%%%%%%%%%%%%%%%%%%%%%%%%%%%%%%%%%%%%%%%%%%%%%%%%%%%%%%%%%%%%%%%%%%%%%
%Number density%
RNd = (n0^0.333)*lambdaD;               %Number density REAL - no of real particles per
lambdaD
Nd = Max*(DL/Lx);                       %Number density COMPUTER - no of macroparticles
per LD
Nf = RNd/Nd;                            %Number density CONVERSION FACTOR
Tp = 1/(9*sqrt(Nd));                    %Plasma period
RN0 = 2.5e11;                           %Plasma density REAL
N0 = RN0/Nf;                            %Plasma density COMPUTER
%Charge and mass%
mp_q = Wp^2/(QM*Max/Lx);                %Macroparticle charge COMPUTER
Qf = q/(mp_q/Nf);                       %Charge CONVERSION FACTOR
```

```
M = mp_q/QM;                          %Mass COMPUTER
M = 1;
Mf = Mi/M;                            %Mass CONVERSION FACTOR
%Other%
Wf = Mf*Vthf^2;                       %Energy CONVERSION FACTOR
phiF = Wf/Qf;                         %Potential (Phi) CONVERSION FACTOR
Ef = phiF/Lf;                         %E-field intensity CONVERSION FACTOR
Bf = Mf/(Tf*Qf);                      %Magnetic induction CONVERSION FACTOR
RhoF = Qf/Lf;                         %Charge density CONVERSION FACTOR
K = (vth^2*M)/Te;                     %Boltzmann constant COMPUTER
%Potentials%+
phiREF = 30;                           %Reference potetial REAL
phi0 = phiREF/phiF;                    %Reference potential COMPUTER
RPhiO1 = 30000;                        %Optics 1 potential REAL - 30kV
PhiO1 = RPhiO1/phiF;                   %Optics 1 potential COMPUTER
RPhiO2 = 27000;                        %Optics 2 potential REAL - 27kV
PhiO2 = RPhiO2/phiF;                   %Optics 2 potential COMPUTER
RPhiO3 = -400;                         %Optics 3 potential REAL - -0.4kV
PhiO3 = RPhiO3/phiF;                   %Optics 3 potential COMPUTER
RPhiO4 = 0;                            %Optics 4 potential REAL - 0V
PhiO4 = RPhiO4/phiF;                   %Optics 4 potential COMPUTER

%%Initialize particles%%
Xp = zeros(Max,2);                    %Particle positions
Vp = zeros(Max,2);                    %Particle velocities
insertp = (ny-1)*20;                  %Insert 20 particles per cell
flux = Nd*v_drift*Ly;                 %flux of entering particles
npt = flux*dt;                        %number of real particles created per timestep
SW = npt/insertp;                     %specific weight, real particles per macroparti
%insertp = 50;
phi = ones(nx,ny)*phi0;               %Initial potential set to phi0
np = 0;                               %Clear particles
nnp = 0;                              %Clear extracted particles
O1 = 0;
O2 = 0;
O3 = 0;
O4 = 0;
E = [0 0];
```

%%%

```
%x range for each optics
a=6;
b=9;
c=11;
d=14;
e=16;
f=19;
g=21;
h=24;

%y max for each optics
h1=floor(ny/2);
h2=floor(ny/2);
h3=floor(ny/2);
h4=floor(ny/2);
%initialize optics and boundary conditions
init1;

%%%%%%%%%%%%%%%%%%%%%%%%%%%%%%%%%%%%%%%%%%%%%%%%%%%%%%%%%%%%%%%%%%%%%%%%%%%%

%Display to show program is running
disp(['Solving....'])




%%%%%%%%%%%%%%%%%%%%%%%%%%%%%%%%%%%%%%%%%%%%%%%%%%%%%%%%%%%%%%%%%%%%%%%%%%%%
%MAIN LOOP
%%%%%%%%%%%%%%%%%%%%%%%%%%%%%%%%%%%%%%%%%%%%%%%%%%%%%%%%%%%%%%%%%%%%%%%%%%%%

for p=1:np
       Xp(p,:) = Xp(p,:)/dx;            %Normalize Xp and Vp
       Vp(p,:) = (Vp(p,:)*dt)/dx;
end


for it=1:dt:ts                          %Repeat for set no of time steps

    %Reset field quantities
Rho = zeros(nx,ny);                 %Rho
    Cden = zeros(nx,ny);                %Charge distribution
```

```
    Pd = zeros(nx,ny);                  %Plasma density - for diagnosis only



%%%%%%%%%%%%%Insert particles%%%%%%%%%%%%%%%%%%%%%%%%%
%Check no of particles is within set limit
if (np+insertp>Max)
      disp(['Max no. of particles reached'])
    break
end

%Insert particles at each time step%

%Insert particles randomly across Y and in first cell of X - Poisson
%distribution
    Xp(np+1:np+insertp,1)=poissrnd(2,insertp,1)*C;                    %X position
    Xp(np+1:np+insertp,2)=poissrnd(2,insertp,1)*(Ly/2);               %Y position
 %Maxwellian velocity distribution, include thermal and drift velocity
   a = M/(2*K*Te);                                                    %Maxwellian
   M = 4*a^(3/2)*exp(-a*vth^2)*vth^2/(sqrt(pi));

   Vp(np+1:np+insertp,1)=v_drift+rand(insertp,1)*vth*M;
   Vp(np+1:np+insertp,2)=0.5*rand(insertp,1)*vth*M;

   if Xp(p,2)>ny
       Xp(p,2) = ny - (Xp(p,2)-ny);
       Vp(p,2) = -Vp(p,2);
   end

   pcountf;
   np=np+insertp;




%%%%%%%%%%%%%%%%%%%%%%%%%%%%%%%%%%%%%%%%%%%%%%%%%%%%%%%%%%%%%%%%%%%%
%%Weight particles to grids%%
weightPtoG;
Rho0 = mp_q*N0/Nd;                     %Charge density of each macroparticle


%%%%%%%%%%%%%%%%%%%%%%%%%%%%%%Poisson%%%%%%%%%%%%%%%%%%%%%%%%%%%%%%%%%%%
```

```
poissoncalc;


%%%%%%%%%%%%%%%%%%%%%%%%%%%%%%%%%%%%%%%%%%%%%%%%%%%%%%%%%%%%%%%%%%%%%%%%%%%%%%%%
%%Electric field%%
    EF = -gradient(phi);


%%%%%%%%%%%%%%%%%%%%%%%%%%Insert new particles%%%%%%%%%%%%%%%%%%%%%%%%%%%%%%%%
  MomentumX = zeros(np,1);
  MomentumY = zeros(np,1);
   for p=1:np
       MomentumX(p) = M*Vp(p,1);
       MomentumY(p)= M*Vp(p,2);
   end


%%%%%%%%%%%%%%%%%%%%%%%%%%Move particles%%%%%%%%%%%%%%%%%%%%%%%%%%%%%%%%%%%%%%
p=1;
    while(p<=np)                          %loop over particles
      if Xp(p,1)<Lx

        x = Xp(p,1);                     %X grid point
        y = Xp(p,2);                     %Y grid point
        xgp = int8(x);
        ygp = int8(y);

        if xgp<1
            xgp = floor(xgp+1);
        else
            xgp = round(xgp);
        end                             %Round to integer
        if ygp<1
            ygp = 1;
        elseif ygp>ny-1
                ygp = ny-1;
            else
            ygp = round(ygp);              %Round to integer
        end

        %%%%%%%%%%
        %Electric field
```

```
        E1 = int8(EF(xgp,ygp));
        E2 = int8(EF(xgp+1,ygp));
        E3 = int8(EF(xgp,ygp+1));
        E4 = int8(EF(xgp+1,ygp+1));

        E = [E1 E1]*((C-xgp)*(C-ygp)/(C*C));    %contribution from (i,j)
E = E+ [E2 E2]*(xgp*(C-ygp)/(C*C));     %(i+1,j)
        E = E + [E3 E3]*((C-xgp)*ygp/(C*C));    %(i,j+1)
        E = E + [E4 E4]*(xgp*ygp/(C*C));        %(i+1,j+1)

        E = double(E);
       end

       F = QM*E;
   A = QM*((E*dt^2)/dx);                    %Normalize
       %Update position and velocity
       Vp(p,:) = Vp(p,:)+A;
       Xp(p,:) = Xp(p,:)+Vp(p,:);


%%%%%%%%%%%%%%%%%%%%%%%%%%%%%%%%%%%%%%%%%%%%%%%%%%%%%%%%%%%%%%%%%%%%%%%%%%%%%%%
   %%%%%Effect of boundaries on particles%%%%%

     for p=1:np
     %%Reflective boundary at y=0, x=0, y=Ly
 %Boundary at y=Ly
        if (Xp(p,2)>ny)
            if (Xp(p,2)>(ny+ny))
                Xp(p,2) = ny-0.5;
                Vp(p,2) = -Vp(p,2);
            else
                Xp(p,2) = ny-(Xp(p,2)-ny);
                Vp(p,2) = -Vp(p,2);
            end
        end
%Boundary at y=0
        if (Xp(p,2)<0)
            if  (Xp(p,2)<(-ny))
                Xp(p,2) = 0.1;
                Vp(p,2) = -Vp(p,2);
            else
                Xp(p,2) = -Xp(p,2);              %Move particle back to domain
```

```
                Vp(p,2) = -Vp(p,2);
            end
        end
%Boundary at x=0
        if (Xp(p,1)<0)
            if (Xp(p,1)<(-nx))
                Xp(p,1) = 0.1;
                Vp(p,1) = -Vp(p,1);
            else
                Xp(p,1) = -Xp(p,1);
                Vp(p,1) = -Vp(p,1);
            end
        end

 %At x = Lx allow particle to continue past boundary out of
        %simulation domain and count no. of particles

        if (Xp(p,1)>nx)
            nnp = nnp+1;
            np = np - nnp;
        end


%%%%%%%%%%%%%%%%%%%%%%%%%%%%%%%%%%%%%%%%%%%%%%%%%%%%%%%%%%%%%%%%%%%%%%%%%%%%%%%
    %Is particle within Optics1
    if ((Xp(p,1)>=a && Xp(p,1)<b) && ...
       (Xp(p,2)>1 && Xp(p,2)<h1))
        in_opt1=true;
    else
        in_opt1=false;
    end
    %Optics 2
    if ((Xp(p,1)>=c && Xp(p,1)<d) && ...
       (Xp(p,2)>1 && Xp(p,2)<h2))
        in_opt2=true;
    else
        in_opt2=false;
    end
    %Optics 3
    if((Xp(p,1)>=e && Xp(p,1)<f) && ...
       (Xp(p,2)>1 && Xp(p,2)<h3))
        in_opt3=true;
```

```
    else
        in_opt3=false;
    end
    %Optics 4
    if ((Xp(p,1)>=g && Xp(p,1)<h) && ...
       (Xp(p,2)>1 && Xp(p,2)<h4))
        in_opt4=true;
    else
        in_opt4=false;
    end


%%%%%%%%%%%%%%%%%%%%%%%%%%%%%%%%%%%%%%%%%%%%%%%%%%%%%%%%%%%%%%%%%%%%%%%%%%%%

    %Absorbing boundary on optics
     if (in_opt1)
        Xp(p,:) = Xp(np,:);         %Kill particle by replacing it with last particl
        Vp(p,:) = Vp(np,:);
        np = np - 1;                %Reduce particle count
        p = p-1;                    %Reduce particle
        O1 = O1+1;
     end

     if (in_opt2)
        Xp(p,:) = Xp(np,:);         %Kill particle by replacing it with last particl
        Vp(p,:) = Vp(np,:);
        np = np - 1;                %Reduce particle count
        p = p-1;                    %Reduce particle index
        O2 = O2+1;
     end

     if (in_opt3)
        Xp(p,:) = Xp(np,:);         %Kill particle by replacing it with last particl
        Vp(p,:) = Vp(np,:);
        np = np - 1;                %Reduce particle count
        p = p-1;                    %Reduce particle index
        O3 = O3+1;
     end

     if (in_opt4)
        Xp(p,:) = Xp(np,:);         %Kill particle by replacing it with last particl
        Vp(p,:) = Vp(np,:);
```

```
        np = np - 1;                %Reduce particle count
        p = p-1;                    %Reduce particle index
        O4 = O4+1;
     end
  end

%%%
```

Function: init1

```
function init1
global nx ny j Optics1 Optics2 Optics3 Optics4 a b c d e f g h h1 h2 h3 h4;


%Optics 1 dimensions - Plasma grid
box(1,:) = [a b]; %X range
box(2,:) = [1 h1];              %Y range

%Define optics
Optics1 = zeros(nx,ny);
for j=box(2,1):box(2,2)
    Optics1(box(1,1):box(1,2),j)=ones(box(1,2)-box(1,1)+1,1);
end

%Optics dimensions - Extraction grid
box(3,:) = [c d]; %X range
box(4,:) = [1 h2];              %Y range

%Define optics
Optics2 = zeros(nx,ny);
for j=box(4,1):box(4,2)
    Optics2(box(3,1):box(3,2),j)=ones(box(3,2)-box(3,1)+1,1);
end

%Optics dimensions - Accel grid
box(5,:) = [e f]; %X range
box(6,:) = [1 h3];              %Y range

%Define optics
Optics3 = zeros(nx,ny);
for j=box(6,1):box(6,2)
    Optics3(box(5,1):box(5,2),j)=ones(box(5,2)-box(5,1)+1,1);
end

%Optics dimensions - Ground grid
box(7,:) = [g h]; %X range
box(8,:) = [1 h4];              %Y range

%Define optics
Optics4 = zeros(nx,ny);
for j=box(8,1):box(8,2)
```

```
    Optics4(box(7,1):box(7,2),j)=ones(box(7,2)-box(7,1)+1,1);
end

end
```

Function: weightPtoG

```
function weightPtoG
global np p Xp Cden C nx ny q


for p=1:np                              %loop over particles

      if Xp(p,1)<nx
        x = Xp(p,1);                     %X grid point
        y = Xp(p,2);                     %Y grid point
        xgp = int8(x);
        ygp = int8(y);

        if xgp<1
            xgp = 1;
        end
        if xgp>(nx-1)
            xgp = nx-1;
        else
            xgp = round(xgp);
        end

        if ygp<1
            ygp = 1;
        end
        if ygp>(ny-1)
                ygp = ny-1;
            else
            ygp = round(ygp);              %Round to integer
        end

        Cden(xgp,ygp) = Cden(xgp,ygp)+((C-xgp)*(C-ygp)/(C*C));
Cden(xgp+1,ygp) = Cden(xgp+1,ygp)+(xgp*(C-ygp)/(C*C));
        Cden(xgp,ygp+1) = Cden(xgp,ygp+1)+((C-xgp)*ygp/(C*C));
        Cden(xgp+1,ygp+1) = Cden(xgp+1,ygp+1)+(xgp*ygp/(C*C));


      end
end

end
```

Function: poissoncalc

```
function poissoncalc
global phi Rho mp_q Optics1 Optics2 Optics3 Optics4 PhiO1 PhiO2 PhiO3 PhiO4 nx ny C

    %Rho = SW*mp_q*(Cden*npt)/(C*C);        %Specific weight x

    Rho = Cden*mp_q*SW;

%Reshape arrays into column vectors
    PHI = reshape(phi, numel(phi),1);
    rho = reshape(Rho, numel(Rho),1);

    rho1 = reshape(rho,nx,ny);

    %%%%%%%%%%%%%%%%%%%%
    %Set boundary conditions - divide by RhoF to normalize
    rho1(:,1) = 0;                                  %Electric field on y=0;
    rho1(:,ny) = 0;                                 %Electric field on y=L;
    rho1(nx,:) = 0;                                      %Electric field on x=L;
    rho1(1,:) = 0 ;                                 %Electric field on x=0;

    rho2 = rho1+(Optics1*PhiO1)+(Optics2*PhiO2)+(Optics3*PhiO3)+(Optics4*PhiO4);
    PHI = reshape(PHI,nx,ny);
    rho2 = rho2+PHI;
    rho2 = reshape(rho2,numel(rho1),1);

    %Solve Poisson equation
    S = numel(rho2);
    phi = poicalc(rho2,C,C,S,1);
    %Reshape to nx by ny array
    phi = reshape(phi,nx,ny);

end
```

Appendix C - Presentation at 33rd International Conference on Plasma Physics [ICPP-2012], Venice, Italy, 2012

A poster was presented on this research at the 33rd International Conference on Plasma Physics (Venice, November 14-16 2012) and is shown below along with the poster abstract.

Poster Abstract

Simulation of Dual Stage Ion Thruster Using a Particle in Cell Code

Background:
Traditional ion thrusters make use of two or three accelerator grids to accelerate ions and thereby produce thrust. A recent concept is the dual stage ion thruster, in which the extraction and acceleration of ions is split into two stages, allowing a higher accelerating potential to be applied without adverse affects. Simulations are often used to model ion thrusters, in order to attempt to improve performance and lifetime.

Method:
A two dimensional particle in cell code has been written in order to simulate the flow of ions through a single aperture on dual stage ion thrusters. This code has been used to simulate an aperture in the Dual-Stage 4-Grid (DS4G) ion thruster and the Dual-Stage 3-grid (DS3G) ion thruster. Original results were compared with results obtained through testing of a DS4G prototype in a vacuum chamber and other simulations of the DS3G. The parameters of the grids, including voltage applied to the grids, grid thickness, grid separation and aperture size were then varied in order to arrive at the optimum configuration.

Results:
Results will be presented showing the most efficient grid configuration and voltage profile to produce certain specific impulses for the DS4G and DS3G ion thrusters in terms of thrust, momentum, beam divergence and ion impaction on the grids, a key factor in determining the lifetime of the thruster. The 3 grid and 4 grid configurations were compared in order to decide whether the added complexity of the fourth grid makes a significant difference to the performance of the thruster. The 3 grid simulation was then run with a set voltage profile applied to the grids while the configuration was varied to find the most efficient grid configuration in order to maximise the performance parameters stated above.

Simulation of dual-stage ion thrusters using a particle-in-cell code

Ellie Bramer

Introduction

Gridded ion engines use electrostatic forces to accelerate ions and produce thrust. Dual stage ion thrusters separate ion extraction and acceleration into 2 stages, allowing higher acceleration potentials to be applied. This produces higher specific impulse (SI), exit velocity and thrust density.

The Dual-Stage 4-Grid (DS4G) ion thruster uses four grids, screen, extraction, acceleration and deceleration. It has been suggested [1] that the benefits provided by the fourth grid are outweighed by the added complexity of the thruster.

Simulations are often used to model the performance of ion thrusters

The Particle in Cell Code

In a particle in cell (PIC) code, a mathematical grid is imposed on the simulation domain. Particle positions are interpolated to the grid, the field equations are performed on the grid and the fields are then interpolated back to the particle positions. The new particle positions can then be calculated.

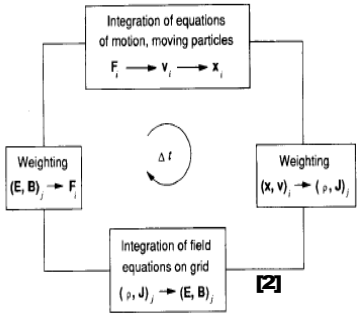

[2]

A single simulation particle represents a large number of real particles and is known as a 'super particle'.

Weighting Schemes

A first order, or bilinear, weighting scheme was chosen for this simulation. In a first order weighting scheme the particle charge is linearly weighted to the four nearest grid points (in 2D). The weighting scheme is given by

$$\rho_{j,k} = \rho_c \frac{(\Delta x - x)(\Delta y - y)}{\Delta x \Delta y}$$

$$\rho_{j+1,k} = \rho_c \frac{x(\Delta y - y)}{\Delta x \Delta y}$$

$$\rho_{j+1,k+1} = \rho_c \frac{xy}{\Delta x \Delta y}$$

$$\rho_{j,k+1} = \rho_c \frac{(\Delta x - x)y}{\Delta x \Delta y}$$

Where ρ_c is the charge of the super particle, Δx and Δy are the grid spacings in the x and y directions.
The same weighting scheme is used to interpolate the particle positions to the grid and then the forces back to the particles.

Field Equations

The charge densities calculated at the grid points become the right hand side of Poisson's equation

$$\nabla^2 \phi(x, y) = \frac{-\rho(x, y)}{\epsilon_0} \quad (1)$$

And the electric field can be calculated from

$$\mathrm{E(x)} = -\nabla \phi(\mathrm{x}) \quad (2)$$

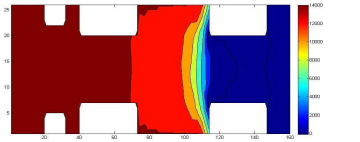
Fig 1. Potential within the simulation domain. White areas are the accelerator grids. Potential in real units, x and y axis arbitrary computer units

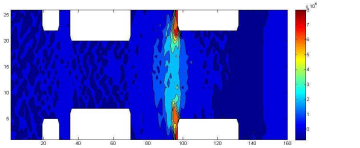
Fig 2. X component of the electric field within the simulation domain, in real units

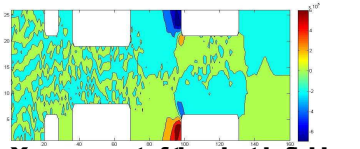
Fig 3. Y component of the electric field within the simulation domain.

Particle Mover

The fields can then be weighted back to the particles, and the new particle positions can be calculated using the leapfrog particle mover, using

$$v_{new} = v_{old} + \frac{q}{m} E \triangle t \quad (3)$$

$$x_{new} = x_{old} + v_{new} \triangle t \quad (4)$$

Results

Dual-Stage 4-Grid Thruster (DS4G)
The most efficient voltage profile and grid configuration to produce an Isp of 15,000s was found to be:
- Total applied voltage of 9,500V
- Screen grid diameter: 0.5mm
- Other grid diameters: 2mm
- Extraction stage gap: 0.5mm
- Acceleration stage gap:2mm
- Deceleration stage gap: 1mm
- Aperture diameter: 0.7 – 1mm

-- Power efficiency: 0.54

Dual-Stage 3-Grid Thruster (DS3G)
For an Isp of 15,000s:
- Total applied voltage of 10,000V
- Screen grid diameter: 0.5mm
- Other grid diameters: 2mm
- Extraction stage gap: 0.5mm
- Acceleration stage gap:2.5mm
- Aperture diameter: 0.7 – 1mm

-- Power efficiency: 0.56

Conclusions

The DS4G case required a lower applied voltage in order to produce an Isp of 15,000s, and produced a higher thrust and better beam focusing. However the DS3G produced a slightly higher power efficiency.
Although the main reason for the deceleration grid is to protect the thruster from backstreaming ions it does seem to provide some benefit in terms of thrust and beam focusing.

References

[1] Coletti et.al. (2010). A 4-Gridded Ion Engine for High Impulse Mission. Space Propulsion 2010. Spain 2010.
[2] Birdsall, C (1991). Particle in Cell Charged-Particle Simulations Plus Monte Carlo Collisions with Neutral Atoms, PIC-MCC. IEEE Transactions on Plasma Science. 19(2).